The Study of Chemically Cross-Linked Ion Gels for Electronic Devices

Jeong, Jaehoon

(2020)

The Study of Chemically Cross-Linked Ion Gels for Electronic Devices

1. Ink-Jet Printable, Self-Assembled, and Chemically Cross-Linked Ion Gel as an Electrolyte for Thin Film, Printable Field Transistors

2. Adhesive Ion Gel as Gate Insulator of Electrolyte-Gated Transistors

TECHNISCHE UNIVERSITÄT DARMSTADT

Vom Fachbereich Material- und Geowissenschaften

der Technischen Universität Darmstadt

zur Erlangung des akademischen Titels Doktor-Ingenieur (Dr.-Ing.)

genehmigte Dissertation von

M.Sc. Jaehoon Jeong geboren in Seoul, Republic of Korea.

1. Gutachten: Prof. Dr. -Ing. Horst Hahn

2. Gutachten: Prof. Dr. rer. nat. Uli Lemmer

Tag der Einreichung: 28.08.2020

Tag der Prüfung: 05.11.2020

Darmstadt 2020-D 17

Erklärung zur Dissertation

Hiermit versichere ich, dass ich meine Dissertation selbstständig und nur mit den angegebenen Quellen und Hilfsmitteln angefertigt habe. Diese Arbeit hat in gleicher oder ähnlicher Form noch keiner Prüfungsbehörde vorgelegen.

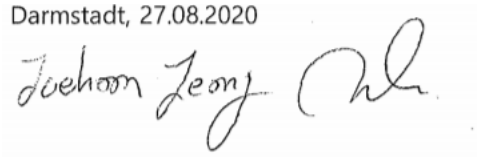

Jeong, Jaehoon: The Study of Chemically Cross-Linked Ion Gels for Electronic Devices

Darmstadt, Technische Universität Darmstadt
Jahr der Veröffentlichung der Dissertation auf TUprints: 2020
Tag der mündlichen Prüfung: 05.11.2020

Abstract

This thesis presents the development of new chemically cross-linked (CC) ion gels and their application in electronic devices. The CC ion gels are synthesized by a hitherto unreported and novel method using self-assembled gelation; this method allows for a straightforward synthesis without complicated procedures. The CC ion gels have excellent ionic conductivities and can exhibit high capacitances through the formation of electric double layers.

These CC ion gels are applied to electrolyte-gated transistors (EGTs) in the field of printed electronics. In particular, they are applied as gate insulators, which separate the semiconducting channel from the gate electrode. They simultaneously act as mediating materials for electric double layer formation, to switch the channel on and off upon an applied bias potential between source and gate electrode. Two different ion gels are utilized for the fabrication of gate insulators, making use of a self-assembled gelation of a CC ion gel, combined with ink-jet printing, which is an effective technique to fabricate gate insulators of EGTs. The ink-jet printing process involves the development of an ink-jet printable ink to prevent nozzle clogging. The optimized amount of solvent in that ink plays an essential role in inhibiting the gelation before printing. The self-assembled gelation starts upon solvent evaporation after printing, and the CC ion gel is spontaneously synthesized on the semiconductor. In a subsequent approach, adhesive properties are added to the CC ion gel to enable hand laminating of electrodes or semiconductors. The CC ion gels fabricated by both methods exhibit remarkable gating performances in EGTs. In particular, they mitigate the drawback of the major humidity sensitivity of the common composite solid polymer electrolytes (CSPE), and show stable transfer curves in the range of 20 % to 90 % relative humidity.

The presented results enable for the first time ink-jet printing of CC ion gels. Moreover, the presented CC ion gels demonstrate great potential as gate insulators for EGTs. New findings about synthesis, analysis, and utilization of the CC ion gel suggest new directions for the development and application of advanced CC ion gels in the future.

Zusammenfassung / Abstract

In dieser Arbeit wird die Entwicklung neuer chemisch vernetzter (CC) Ionengele und ihre Anwendung in elektronischen Bauteilen vorgestellt. Die CC-Ionengele werden nach einem, in dieser Arbeit entwickelten, neuartigem Verfahren synthetisiert, welche sich eine selbstorganisierte Gelierung zu Nutze macht. Diese Methode ermöglicht eine einfache Synthese ohne komplizierte Verfahrensschritte. Die CC-Ionengele weisen ausgezeichnete Ionenleitfähigkeiten auf und können durch die Bildung elektrischer Doppelschichten hohe Kapazitäten in den entsprechenden elektronischen Bauteilen aufweisen.

Die CC-Ionengele werden in dieser Arbeit für Transistoren mit Elektrolytgating (EGTs) im Bereich der gedruckten Elektronik genutzt. Hierbei dienen sie als Gate-Isolatoren, die den Halbleiterkanal von der Gate-Elektrode trennen. Gleichzeitig unterstützen sie die Bildung einer elektrischen Doppelschicht, um den Halbleiterkanal bei einem angelegten Potential zwischen Source- und Gate-Elektrode leitfähig bzw. isolierend werden zu lassen. In dieser Arbeit wurden zwei verschiedene Ionengele zur Herstellung von Gate-Isolatoren verwendet, wobei die selbstorganisierte Gelierung der Ionengele die Anwendung der Materialien für Tintenstrahldruckprozesse ermöglicht. Hierfür mussten die Eigenschaften der CC-Ionengel-Tinten maßgeschneidert werden, damit ein Verstopfen der Düse verhindert werde konnte. Die optimierte Menge an Lösungsmittel in dieser Tinte spielt eine wesentliche Rolle bei der Hemmung des Gelierprozesses, so dass eine Tinte mit niedriger Viskosität für den Druckprozess erzeugt werden kann. Die selbstorganisierte Gelierung beginnt mit dem Verdampfen des Lösungsmittels nach dem Drucken und das CC-Ionengel wird erst auf dem Substrat gebildet. In einem nachfolgenden Ansatz werden dem CC-Ionengel adhäsive Eigenschaften hinzugefügt, um das Handlaminieren von Elektroden oder Halbleitern zu ermöglichen. Beide hergestellten CC-Ionengele zeigen bemerkenswerte elektrische Leistungskennzahlen. Ein weiterer bemerkenswerter Vorteil des CC-Ionengel-Gatings ist die Unempfindlichkeit gegenüber Luftfeuchtigkeit. Durch dieses Konzept konnte das Problem der stark schwankenden Leistung von standard-Polymerelektrolyt gegateten Transistoren bei unterschiedlichen Luftfeuchtigkeiten gelöst und eine Anwendung gedruckter Transistoren bei Umgebungsbedingungen ermöglicht werden.

Zusammengefasst ermöglichen die vorgestellten Ergebnisse erstmals den Tintenstrahldruck von CC-Ionengelen. Darüber hinaus zeigen die vorgestellten CC-Ionengele ein großes Potenzial als Gate-Isolatoren für Elektrolyt gegatete Transistoren. Diese neuen Erkenntnisse zur Synthese, Analyse und Verwendung des CC-Ionengels, eröffnen neue Anwendungsmöglichkeiten und Entwicklungen für fortschrittliche CC-Ionengele.

Table of Contents

Chapter 1

1. Introduction

An electrolyte is a substance that can be dissociated in a polar solvent and makes a solution electrically conducting when an electric potential is applied. In 1884, the terminology of "electrolyte" was first defined by Svante Arrhenius [1]. In his doctoral thesis, he first proposed the theory regarding the dissociation of rock salt into positive and negative ions in water [1]. In 1903, he was awarded the Nobel Prize in chemistry for his findings. Since then, the definition of ions was established based on his discovery. Electrolytes have been utilized for many applications, especially in the field of electrochemistry. For instance, carbonate-based electrolytes such as $LiPF_6$ solved in propylene carbonate, ethylene carbonate, and dimethyl carbonate are used in lithium-ion batteries. These electrolytes prevent internal electronic conduction between the cathode and the anode, and transfer lithium ions for redox reactions during charging/discharging processes. Electrolytes are also utilized in many electrochemical applications such as supercapacitors [2], sensors [3,4], and water electrolysis [5,6].

An electrolyte can exist in the liquid phase, but also in the solid phase. The discovery of polymer electrolytes (PE) had a significant impact on electrolyte research. The solid polymer electrolyte (SPE), the primary type of PEs, was first reported in 1975 by Wright et al., who studied an ionic polymer complex using poly(ethylene oxide)(PEO) [7]. The SPE dissociates salts through a lone pair of electrons, located at certain donor atoms. Unlike liquid-phase electrolytes, the dissociated ions in SPEs are transferred by an ion-hopping mechanism. Therefore, the ionic conductivity of an SPE is much lower than that of liquid-phase electrolytes because the ion-hopping mechanism is governed by a slow segmental movement of polymers. Hence, apart from SPEs, advanced types of PEs such as polyelectrolytes, gel polymer electrolytes, and composite polymer electrolytes have been developed to enhance the ionic conductivity. The primary advantage of PEs

is that they are easy to handle. It is convenient to fabricate the films and apply them to devices contrary to liquid-phase electrolytes. Moreover, it can reduce safety issues of liquid-phase electrolytes, e.g. leakage or gas evolution, which can lead to severe accidents. However, the low ionic conductivity offsets these advantages, and thus PEs are rarely used in commercial devices. This technical obstacle constitutes a major drawback of PEs and requires further studies to solve low ionic conductivity.

A novel approach, the use of ionic liquids (ILs), opens up new pathways for the development of PEs. An IL is a molten salt, which appears as a liquid at room temperature. In general, ILs have excellent ionic conductivities and other intrinsic properties such as high capacitance, non-volatility, and electrochemical stability. Therefore, the synthesis of solid-phase electrolytes, using ILs, constitutes a straightforward approach for new types of unique materials called ion gels, which show better key parameters for electrolyte utilization than PEs. An ion gel consists of cross-linked polymers and incorporated ILs. The cross-linked polymers make polymeric gel structures by absorbing the ILs. The structures and components of ion gels are described in detail in Chapter 2. Therefore, ion gels have been utilized in many electrochemical devices, especially in the area of printed electronics.

The field of printed electronics is quite promising and consists of electronic devices, which are fabricated using printing techniques. The fabrication process is a simple and inexpensive method, and electrical circuits can be easily fabricated on various substrates such as metals, plastics, and fabrics. Therefore, printed electronics are considered the future of electronics; suitable for flexible, wearable, and Internet of Things (IoT) devices. Within printed electronics, ion gels and polymer electrolytes are most commonly used in electrolyte-gated transistors (EGTs) as a gate insulator. The EGT operates by the applied gate voltages controlling the formation/dissolution of electrical double layers (EDLs) at the interface of the semiconductor and the electrolyte. Due to the high capacitance from EDLs, the EGT can be operated at a low gate voltage (< 2V). However, the slow switching speed as a result of the slow formation/dissolution of the EDLs is considered a fatal drawback of the EGTs, and therefore, it is necessary to develop highly ionic conductive solid-phase electrolytes to improve the switching speed of EGTs.

This thesis deals with the synthesis and the application of new ion gels for gate insulators in EGTs. The new ion gels are synthesized by a self-assembled gelation using a simple method. They have remarkable ionic conductivities and can drive high capacitance by EDLs. In addition, the ion gels are designed so that it is possible to fabricate the gate insulator of EGTs by ink-jet printing or film lamination method using adhesive property. As a gate insulator, the newly-synthesized ion gels demonstrate remarkable gating performances in EGTs.

Chapter 2

2. Fundamentals

This chapter aims to introduce the fundamentals of ionic liquids, solid-phase electrolytes (polymer electrolytes and ion gels), and electrolyte-gated transistors (EGTs). Section 2.1 covers the basics of ionic liquids such as development history, material properties, and applications. Section 2.2 introduces solid-phase electrolytes that have been classified into four different polymer electrolytes and ion gels. Section 2.3 introduces metal-oxide-semiconductor field-effect transistors (MOSFETs) and EGTs with in-detail information on their structure, operational mechanism, and characterizations.

2.1. Room-Temperature Molten Salts, Ionic Liquids (IL)

An ionic liquid (IL) is composed of organic cations and inorganic or polyatomic anions. The combination of different cations and anions results in several thousand ILs. By replacing cations or anions, their material properties such as ionic conductivity, electrochemical stability, and viscosity can be modified easily. These tailorable properties deem it more suitable for a wide variety of applications. For this reason, ILs have been utilized as an electrolyte or as a solvent in many fields. In this thesis, the IL is used as a critical material to synthesize ion gel. Therefore, it is necessary to introduce the basics of ILs in detail. This section describes the fundamentals of the development (2.1.1.), material properties (2.1.2.), and applications (2.1.3.) of ILs**.**

2.1.1. Development History of Ionic Liquids

An ionic liquid (IL) has a relatively long history; it has been around 100 years since they were first discovered in the early 1900s. Although, ILs have recently been attracting massive attention from industry and academia and the number of related studies done has exponentially increased, they

were not highlighted until the mid-1900s. ILs were first discovered by Paul Walden, who was nominated as a candidate for the Nobel Prize in Chemistry in 1913 and 1914 for the study of Walden inversion. In 1914, he discovered ethylammonium nitrate ($[EtNH_3][NO_3]$), which has a melting point of 12 °C and is known as the first-ever reported room-temperature molten salt [8]. Although in 1888 Gabriel and Weiner discovered ethanolammonium nitrate, which has a melting point of 55 °C [9], it does not sufficiently accord with the current definition of ILs because of a slightly higher melting point than room temperature. Despite notable inventions, researchers did not recognize the importance of ILs at that time, and there were no prominent studies until the mid-1900s.

In the mid-1900s, there was a significant development of ILs by the U.S. Air Force Academy. At that time, research groups in the U.S. Air Force Academy sought new electrolytes to substitute the LiCl/KCl molten salt present in thermal batteries because high operating temperatures (375-550 °C) can damage battery materials [10]. For this reason, Lowell A. King, one of the pioneers of chloroaluminate molten salts, first organized research projects to develop chloroaluminate molten salts consisting of alkali chloride and aluminum chloride ($AlCl_3$) [10,11]. He networked with other research groups for collaborations in efforts to substitute the existing LiCl/KCl molten salts with chloroaluminate molten salt. In one of the remarkable studies carried out with this ambition, Charles Hussey, who served his military duty in the U.S. Air Force Academy, discovered chloroaluminate molten salt of $NaCl/AlCl_3$, which has a melting point of 107 °C [10,11]. However, the lower melting point of $NaCl/AlCl_3$ as compared to LiCl/KCl (molten salt (melting point (m.p.): 352-736 °C) [12], still does not allow it to be in the liquid phase at room temperature. In another fascinating study, Frank Hurley discovered room-temperature chloroaluminate molten salts of ethylpyridinium bromide ([EtPyBr]) and $AlCl_3$ in 1951 [13]. This molten salt has the lowest melting point of –40 °C at a molar ratio of 2:1 ($[EtPyBr]:[AlCl_3]$), which varies depending on the molar ratios of [EtPyBr] and $[AlCl_3]$ [13]. This study has become a cornerstone of the development of chloroaluminate molten salts and has thereby influenced subsequent research. For instance, Chum et al. utilized the chloroaluminate molten salts of $[EtPyBr][AlCl_3]$ as a solvent for the electrochemical analysis of hexamethylbenzene and organometallic ion complexes [14].

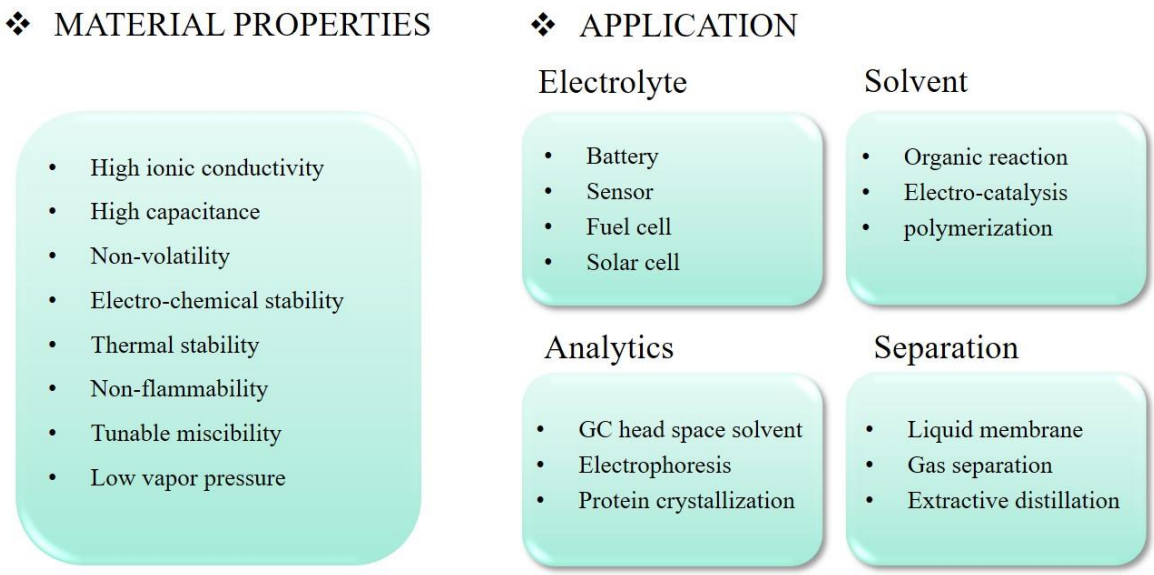

Figure 2-1. Material properties and application list of ionic liquids

Furthermore, many research groups have investigated tetraalkylammonium-based ILs. In 1964, Wen and Saito reported a study about the influence of symmetric alkyl groups of CH_3, C_2H_5, n-C_3H_7, and n-C_5H_{11} on the volume of tetraalkylammonium bromides in aqueous solution [15]. Subsequently, Conway et al. studied the volume change of tetraalkylammonium halide depending on halide ions (Cl^-, Br^-, I^-) [16]. Kay et al. also studied the viscosity coefficient of tetraalkylammonium halides, which varied with alkyl chains [17]. In addition, tetraalkylammonium-based ILs were used as a solvent in diverse applications. For example, Parshall *et al.* used tetraalkylammonium-based molten salts of $[(C_2H_5)_4N][SnCl_3]$ and $[(C_2H_5)_4N][GeCl_3]$ (m.p.: 78 and 68 °C) as a solvent for the electrocatalytic reaction of olefin [18]. Until now, many types of tetraalkylammonium-based ILs have been developed and widely used due to their outstanding electrochemical stability.

In the late-1900s, significant advances were made in the development of ILs. In particular, various ILs were developed to solve the humidity instability of chloroaluminate molten salts. In 1982, John S Wilkes first identified that the binary system of 1,3-dialkyl imidazolium chloride and $AlCl_3$ has more enhanced electrochemical stability than 1-alkyl pyridinium chloroaluminate [19]. Subsequently, in 1992, he discovered air- and water-stable ILs using 1-ethyl-3-methylimidazolium ($[EMIM]^+$) cations [20]. This discovery of $[EMIM]^+$ triggered the development of water-stable ILs. Since then, diverse imidazolium-based ILs have been developed, mainly by combining it with fluorinated anions such as bis(trifluoromethanesulfonate) ($[TFSI]^-$), trifluoromethanesulfonate ($[OTf]^-$), bis(fluorosulfonyl)imide ($[FSI]^-$), hexafluorophosphate (PF_6^-), and tetrafluoroborate (BF_4^-).

Since the early 2000s, research into ILs has increased in a widespread fashion. However, the material development of ILs is in gridlock, and most of the state-of-the-art studies focus on utilizing ILs in applications. The cations or anions for ILs discovered a few decades ago are considered top-notch and are still in use today.

2.1.2. Properties of Ionic Liquids

ILs have advantages with respect to their decisive properties compared to conventional solvents because tailoring allows for the selection and combination of suitable cations or anions depending on the required properties of the application (Figure 2-1). The ionic conductivity, electrochemical stability or other properties of ILs can be easily manipulated by combining cations and anions, rendering ILs as "designer solvents".

ILs should preferably have weak Coulomb interactions between their cation and anion to reduce their melting points. The melting points of ILs are influenced by ion sizes, charge distributions, or symmetries of the alkyl chains [11]. Ion sizes of anions and cations are an important factor in determining Coulomb interactions and melting points, the impact of the sizes can partially be described by the hard or soft acids and bases (HSAB) concept. Here, the size ratios and the charges on each ion lead to a classification in HSAB. Small ions with high valences, which are hard to polarize are called "hard", while large ions, with low valences, which are easily polarizable are referred to as soft ions. The HSAB concept predicts that hard bases form strong bonds with hard acids and soft bases with soft acids, because of an improved orbital overlapping compared to a hard/soft species. This usually leads to higher melting points for hard/hard or soft/soft species than for hard/soft materials. For example, the ion sizes of some anions are listed in Table 2-1: Cl^- < $[BF_4]^-$ < $[PF_6]^-$ < $[AlCl_4]^-$. The melting point of NaCl is 801 °C and much higher than that of $Na[AlCl_4]$ (melting point: 184 °C), since Na^+ and Cl^- are both hard ions, but $AlCl_4^-$ can be described as soft.

Another effect, which influences the melting point of a salt, is the shielding of charges in the individual ions. When the ions are shielded due to steric forces, the charges cannot come close to each another and the bond is weak. As an example, [EMIM]Cl has a higher melting point than $[EMIM][BF_4]$ and $[EMIM][AlCl_4]$. Moreover, Gordon and Rao reported that the melting point of tetraalkylammonium varies with the symmetricity and length of voluminous alkyl groups [21]. Moreover, the melting point of imidazolium is also affected by the length of the alkyl chains, disturbing ion packing and crystallinity [11]. Depending on the used species, additional effects can appear as well, e.g. aromatic π-π stacking, complicating the prediction of the melting points even further.

Table 2-1. Melting points of NaX and [EMIM]X with different anions (ionic radii of Na^+ and $[EMIM]^+$: 1.2 Å and 2×2.7 Å, respectively) [11,22]. Thermochemical radii of anions are calculated by Kapustinskii Equation.[22]

X^-	Thermochemical Radius (Å)	Melting point (°C)	
		NaX	[EMIM]X
Cl^-	1.68 ± 0.19	801	87
$[BF_4]^-$	2.05 ± 0.19	384	6
$[PF_6]^-$	2.42 ± 0.19	200	60
$[AlCl_4]^-$	3.17 ± 0.19	185	7

One important property of ILs, which is related to this work, is that ILs can be tailored to have a wide electrochemical potential window, which corresponds to the electrochemically stable potential range where no oxidation or reduction reaction occurs. Therefore, ILs are often used for electrochemical applications, since the main reactions are induced without side reactions. The electrochemical window of ILs is influenced by the reduction of cations and the oxidation of anions [11]. The electrochemical stabilities of individual cations and anions are as below [11,23]:

Cations: pyridinium ≤ pyrazolium ≤ imidazolium ≤ sulfonium ≤ ammonium
Anions: halide ions (Cl^-, I^-, Br^-) except for fluoride (F^-) ≤ chloroaluminates ($AlCl_4^-$, $Al_2Cl_7^-$) ≤ triflyl group($[CF_3SO_2]^-$)-based anions (triflate ($[CF_3SO_3]^-$), TFSI ($[[CF_3SO_3]_2N]^-$) ≤ fluorinated ions (PF_6^-, BF_4^-).

Each cation and anion has different electrochemical stability, and the combinations of them vary electrochemical windows. For example, the electrochemical windows of [BMIM][BF_4], [BMIM][CF_3SO_3], and [BMIM]I are 4.6 V, 4.2 V, and 2 V, respectively [23]. Halide ions of I^- are easily oxidized in comparison with the fluorine-containing anions like $[CF_3SO_3]^-$ and $[BF_4]^-$. However, among halide ions, fluoride (F^-) is very stable against oxidation. Fluorinated ions of $[PF_6]^-$ and $[BF_4]^-$ have similar or slightly higher oxidation stability than triflate or triflyl ions. However, $[PF_6]^-$ reacts with water to produce hydrogen fluoride (HF) [24]. Moreover, it has been noted that the electrochemical window of [BMIM][BF_4] is drastically reduced from 4.1 V to 1.95 V due to the reaction between $[BF_4]^-$ and 3 wt% of water impurity [25]. The reduction stabilities of cations also affect the electrochemical window. For example, the electrochemical windows of [EMIM][TFSI] and [$N_{1,8,8,8}$][TFSI] are 4.1 V and 5.7 V, respectively, and it results from the different reduction stabilities of $[EMIM]^+$ and $[N_{1,8,8,8}]^+$. Therefore, the electrochemical stability of ILs is related to the individual stabilities of cations and anions and can be customized depending on the applied voltage and working conditions of the applications.

Ionic conductivity is one of the most important properties of ILs, especially for electrochemical devices. In general, the ILs have high ionic conductivity in the range from 10^{-4} to 10^{-2} S cm^{-1}, varied by the composition of cations and anions. This ionic conductivity is determined

by cation size, viscosity, and the ion structure of the cations and anions. The viscosity is related to the Coulomb interaction of cations and anions, and the ionic conductivity increases as the viscosity decreases [26]**.** The order of ionic conductivity of cations is as follows: pyridinium ≤ ammonium < sulfonium ≤ imidazolium [11]. In general, imidazolium-based ILs have a relatively higher ionic conductivity than other ILs.

2.1.3. Applications of Ionic Liquids

The interest in ILs, which has exponentially grown since the early 2000s, has led to an explosion of research in various fields. In particular, due to their unique and tailorable properties, ILs have been used in many applications such as batteries, sensors, and analytic solvents. This subsection provides a brief description of those applications and related literature reviews.

Batteries have significantly influenced the development of ILs. Nowadays, chloroaluminate molten salts mainly used for thermal batteries have been replaced by new ILs in a lithium-ion battery (LIB). The role of the anion is important for LIBs because the interaction between lithium-ions (Li^+) and anions governs the transport and electrochemical reaction of Li^+ at the surface of the electrode [27,28]. Among anions, $[TFSI]^-$ and $[BF_4]^-$ have been mainly studied for LIBs. Notably, $[TFSI]^-$ is mainly used rather than BF_4^- because the water-immiscibility of $[TFSI]^-$ makes impurity extractions much more convenient with water washing [28]. $[TFSI]^-$ has several advantages suitable for LIB, but also has a disadvantage: the layers of ionic species such as Li^+, $[TFSI]^-$, and $[Li(TFSI)_2]^-$, accumulated at the interface of the electrode, can prevent the electrochemical reduction of cations by acting like the solid electrolyte interface (SEI) layer [29]. For this reason, advanced anions such as $[(FSO_2)(C_2F_5SO_2)N]^-$, $[FSI]^-$, and $[TFAC]^-$, have been developed to substitute $[TFSI]^-$ [30,31]. Among them, $[FSI]^-$ is considered the most promising anion for LIBs. [FSI]-based ILs have low interfacial charge transfer resistance with a Li anode and $LiCoO_2$ cathode [32]. Furthermore, $[FSI]^-$ prevents irreversible reactions and facilitates reversible Li intercalation to graphene electrodes [33]. On the other hand, among cations of ILs, ammonium, pyrrolidinium, and piperidinium-based ILs have been mainly investigated to be used for LIBs. For instance, Egashira et al. reported the influence of cyano groups on battery cycles by comparing them with [CTMA][TFSI]/LiTFSI and $[N_{1,1,1,4}]$[TFSI]/LiTFSI [34]. Reale *et al.* studied solid electrolyte layer (SEI) formation and cycle performance of LIB using $[Pyr_{24}]$[TFSI] and electrodes of lithium titanium oxide (LTO) and lithium iron phosphate (LFP) [35]. In addition, ILs have been applied to various types of batteries, such as lithium-sulfur batteries [36,37] and lithium-air batteries [38,39].

In another application, ILs are used as a solvent for materials synthesis. ILs can be used in diverse synthetic reactions of organics, inorganics, or polymers because material properties can be tailored easily depending on the synthetic conditions. Furthermore, it is easy to separate the solvent from the product by vacuum steam distillation or supercritical fluid extraction (CO_2) [11]. For the

synthesis of organics, ILs can be used for electrophilic substitutions and additions, Friedel-crafts alkylation reaction, cracking and isomerization reaction, hydrogenation, and hydroformylation [11,40]. For example, Wilkes et al. reported studies of the electrophilic substitution of benzene in [EMIM]Cl/$AlCl_3$ [41]. In this study, benzene is selectively transformed into chlorobenzene and dichlorobenzene in the acid state or chlorobenzene and an isomer of tetrachlorocyclohexene and hexachlorocyclohexane in base state [41]. In the synthesis of polymers, ILs can be used in almost synthetic reactions such as acid-catalyzed cationic polymerization, free radical polymerization, Ziegler-Natta polymerization, and Living radical polymerization. For instance, May et al. identified that [EMIM][PF_6] enhances the conversion rate from 3 % to 25 % and molar mass (M_n) from 58,300 g mol^{-1} to 669,000 g mol^{-1}, compared to toluene in the synthesis of PMMA [11].

ILs can also be used as lubricants due to the advantages of low-volatility and non-flammability [42]. Moreover, ILs play a role in forming a thin, protective layer on the surface of metals and reducing wear and friction [42–45]. However, although ILs are considered as eco-friendly and green solvents [46], they are not as cost-effective as other lubricants. For this reason, the ILs are normally used as an additive, and a small amount of IL is blended with conventional lubricants. Among the anions, PF_6^-, BF_4^-, $[OTF]^-$ or $[TFSI]^-$ are used as fluorinated anions [43–45,47]. Dibutylphosphate (DBP) or dis(oxalate)borate (BOB) are also used as non-fluorinated anions [42]. Moreover, quaternary phosphonium or imidazolium are used as cations [42]. In addition, the ILs can also be used in dye-sensitized solar cells, extraction, and spectroscopy. It is expected that the application fields of ILs will increase further as the development of ILs proceeds.

Table 2-2. Lists of ionic liquids used for electrochemical devices.[11,23]

Ionic Liquid (IL)	Abbreviation	Density [g cm^{-3}]	Ionic conductivity [mS cm^{-1}]	Electrochemical window [V]	Viscosity [cP]	Melting point [°C]
imidazolium-based ILs						
1-Ethyl-3-methylimidazolium trifluoromethylsulfonate	[EMIM][OTf]	1.39	9.84	4.3	39.8	–9
1-Butyl-3-methylimidazolium bis (trifluoromethylsulfonyl) imide	[BMIM][TFSI] [BMIM][NTf_2]	1.44	3.41	4.3	48.8	–4
1-Ethyl-3-methylimidazolium bis (trifluoromethylsulfonyl) imide	[EMIM][TFSI] [EMIM][NTf_2]	1.52	6.63	4.1	39.4	–3
1-Methyl-3-propylimidazolium bis (trifluoromethylsulfonyl) imide	[PMIM][TFSI] [PMIM][NTf_2]	1.48	4.4	4.9	43.8	–20
1-Ethyl-3-methylimidazolium tetrafluoroborate	[EMIM][BF_4]	1.28	14.1	4.5	33.8	15
Pyrrolidinium-based ILs						
1-Butyl-1-methylpyrrolidinium bis (trifluoromethylsulfonyl) imide	[BMPyr][TFSI] [Pyr_{14}][TFSI]	1.4	2.12	5.5	94.4	–18
1-Butyl-1-methylpyrrolidinium dicyanamide	[BMPyr][DCA] [Pyr_{14}][DCA]	1.02	10.8	3.5	35.2	–50
1-Butyl-1-methylpyrrolidinium trifluoromethylsulfonate	[BMPyr][OTf] [Pyr_{14}][OTf]	1.26	1.85	4.2	148	3
1-Methyl-1-propylpyrrolidinium bis (trifluoromethylsulfonyl) imide	[PMPyr][TFSI] [Pyr_{13}][TFSI]	1.43	4.92	5.9	58.7	< RT
1-Methyl-1-octylpyrrolidinium bis (trifluoromethylsulfonyl) imide	[OMPyr][TFSI] [Pyr_{18}][TFSI]	1.45	1.27	-	168	< RT
Pyridinium-based ILs						
1-Butyl-2-methylpyridinium bis (trifluoromethylsulfonyl) imide	[Py_{14}][TFSI]	1.43	1.03	4.2	91.5	< RT
1-Butylpyridinium bis (trifluoromethylsulfonyl) imide	[BuPy][TFSI] [BuPy] [NTf_2]	1.45	1.54	4.2	59	< RT
1-Butylpyridinium tetrafluoroborate	[BuPy][BF_4]	1.23	1.94	-	203	< RT
Piperidinium-based ILs						
1-Butyl-1-methylpiperidinium bis (trifluoromethylsulfonyl) imide	[BMPip][TFSI] [Pip_{14}][TFSI]	1.38	0.84	3.7	173	< RT
1-Methyl-1-propylpiperidinium bis (trifluoromethylsulfonyl) imide	[PMPip][TFSI] [Pip_{13}][TFSI]	1.41	2.12	5.9	176	12
Ammonium-based ILs						
N-Methyl-N-trioctylammonium bis(trifluoromethylsulfonyl)imide	[$N_{1,8,8,8}$][TFSI]	1.095	2.2	5.7	-	–50

2.2. Solid-Phase Electrolyte: Polymer Electrolyte and Ion Gels

This section outlines the fundamentals of polymer electrolytes, ion gels, and analysis techniques. Polymer electrolytes and ion gels have similar components and mechanisms of ion conduction, but they are different in polymer structures. In this section, their definition, preparation methods, and literature reviews are detailed. Furthermore, the analysis techniques for frequency-dependent behaviors and polymer structures are introduced. This section discusses polymer electrolyte (2.2.1), ion gel (2.2.2), EIS analysis (2.2.3), and FT-IR Spectroscopy (2.2.4).

2.2.1. Polymer Electrolyte

Polymer electrolytes are solid-phase electrolytes, in which polymers play the role of dissociating salts into ions and facilitating ion conduction. For decades, there have been many studies to develop polymer electrolytes, and many types of polymer electrolytes have been discovered. This subsection introduces four different types of polymer electrolytes differentiated by the composition and ion migration mechanism. Their definitions, properties, and research trends are also discussed in detail.

Solid Polymer Electrolyte

Solid polymer electrolytes (SPE) are solvent-free, solid-phase polymer electrolytes, which are a classic, initial type of SPEs first developed in the 1970s [7]. SPEs consist of backbone polymers (polymer host) and salts. Donor atoms with lone pair electrons on backbone polymers, e.g., oxygen (O), nitrogen (N), and sulfur (S), can dissociate salts into cations and anions. Due to the solvent-free solid phase, the SPEs have excellent intrinsic properties such as mechanical and thermal stabilities, wide electrochemical windows, flexibilities, and are leak-proofs [48]. For the synthesis of the SPEs, alkali metal ions such as lithium ions (Li^+), sodium ions (Na^+), and potassium ions (K^+) are utilized

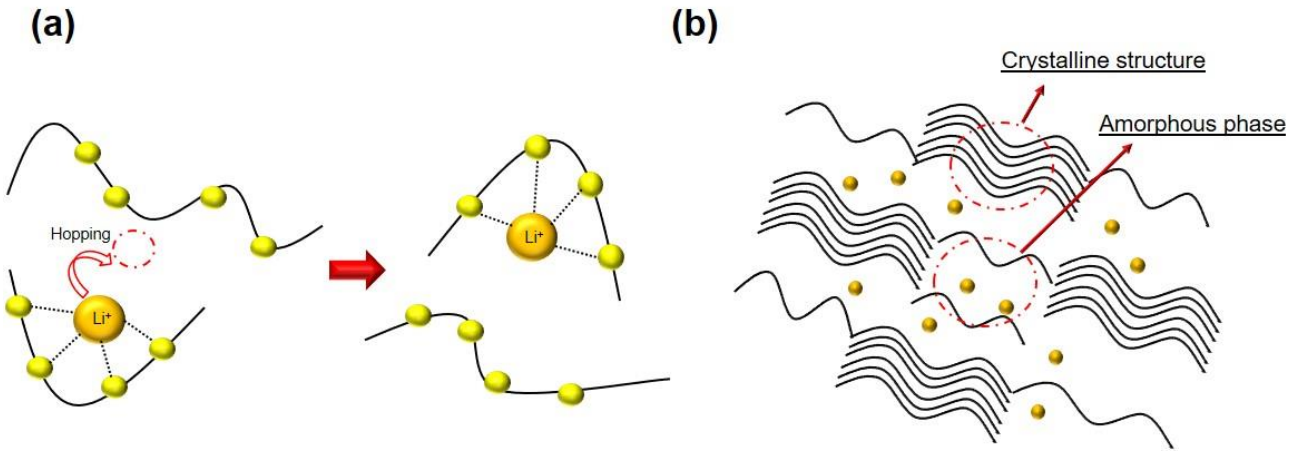

Figure 2-2. Illustration of (a) ion-hopping transfer and (b) crystalline and amorphous structures of SPE

as conducting ions. Moreover, poly(ethylene oxide) (PEO) is used as a backbone polymer because of its low glass transition temperature (T_g) of –67 °C and large solvation power of salts [49,50].

The mechanism of ion conduction is based on ion-hopping transfer by the segmental movement of the backbone polymer, e.g., reptation, which is thermal motion of long linear polymers in concentrated solutions, or rotational motions of small units of polymers. In ionic complexes of SPEs, alkali metal cations co-coordinate with lone pair electrons of donor atoms on backbone polymers by Lewis acid-base interaction [49]. By coordination interaction, the alkali metal ion is centered and surrounded by backbone polymers (Figure 2-2(a)) [7]. This coordinated position of alkali metal cations and segmental movement of the backbone polymer influence the mechanism of ion conduction in SPEs. The coordinated cations can hop to vacant neighboring sites available to form another coordination with donor atoms of backbone polymer. During ion conduction, the segmental movement facilitates cations to hop to neighboring sites, and ion-hopping transfer occurs sequentially. For this reason, it is important to optimize the ratio of donor atoms and ions, affecting coordination and ionic conductivity in the development of SPEs. For example, Shukla et al. reported that the concentration of lithium-ions affects the dielectric relaxation movement of PMMA-based SPE [51]. This study identified that the ion-hopping rate and ionic conductivity reaches the maximum at the ratio of 1:4 (lithium-ion: donor oxygen) [51]. Moreover, the crystallinity of the backbone polymer affects ionic conductivity because crystalline structures hinder segmental movement and narrow the ion-conducting path. Therefore, it is important to make amorphous structures to increase ionic conductivity. This can be done by choosing non-crystalline and low T_g polymers.

Among backbone polymers, PEO has been primarily utilized as a backbone polymer of SPE due to low T_g and ion-dissociating properties. The PEO has advantageous properties such as dimensional stability, chemical stability, corrosion resistance, and mechanical flexibility [48]. PEO-based SPE was first introduced by Wright et al. in 1973 [7,48]. He investigated the melting point of SPEs in dependence on cation sizes, and their corresponding activation energies [7]. Moreover, it was identified that larger cations produce more stable macrocyclic complexes with ethylene oxide units of PEO. Since then, many research groups have carried out studies on PEO-based SPEs. Among PEO-based SPEs, the composition of PEO and lithium perchlorate ($LiClO_4$) has been intensively studied for electronic devices like lithium-ion batteries.

On the other hand, SPE has a critical drawback: the ionic conductivity of the SPE is much lower than other types of PEs. This low ionic conductivity results from crystallinity, slow hopping-ion transfer, and insufficient solubility of salt [52]. Generally, the ionic conductivity of SPE is in the range of 10^{-7} to 10^{-4} S cm^{-1} [53]. For this reason, research into SPE has declined in recent years.

Gel (Plasticized) Polymer Electrolyte

Gel polymer electrolytes (GPE) are advanced polymer electrolytes that are modified from SPEs. GPEs were developed in an effort to enhance the ionic conductivity of SPEs. GPEs have a ternary system consisting of a backbone polymer, salt, and a plasticizer (Figure 2-3). The plasticizer functions like a lubricant and facilitates ion migration in the ionic complex. The use of a plasticizer drastically improves ionic conductivity. In general, cyclic carbonates such as propylene carbonate and ethylene carbonate (Figure 2-4) are used as a plasticizer for the GPE due to their properties such as high dielectric constant, good miscibility, low volatility, and good electrochemical stability. The roles of plasticizers in the GPE are as follows: (1) dissociation of salts and ion aggregates, (2) facilitation of the segmental movement of macromolecular chains, and (3) reduction of crystalline structures.

The dissociation of salts and ion aggregates is important for enhancing ionic conductivity because neutral ion pairs and ion aggregates do not contribute to ionic conductivity. Since dissociation of salts only by donor atoms of the backbone polymer is insufficient, the use of a plasticizer helps to make more free conducting ions by dissociation. The plasticizer also reduces the degree of crystallinity. The plasticizer can permeate through crystalline structures and weaken interactions of macromolecules. Therefore, ion conduction is more facilitated because ions can conduct more easily in amorphous structures than in crystalline structures due to the unimpeded segmental movement of the backbone polymer [52,54].

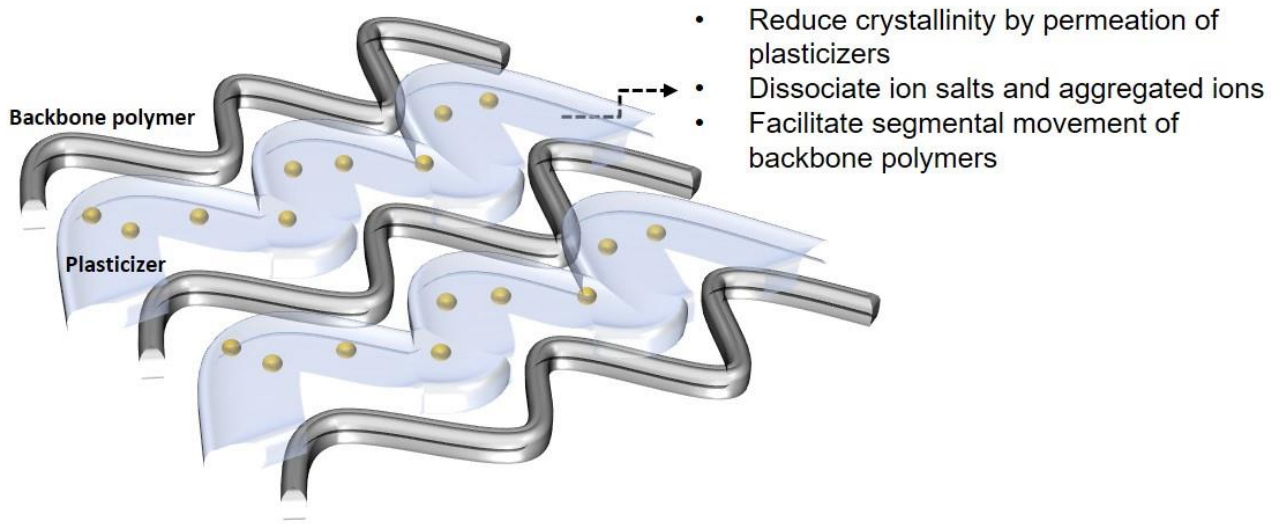

Figure 2-3. Illustration of backbone polymers, plasticizers and salts in gel polymer electrolyte

The most important aspect of the development of GPEs has been to optimize the proportion of components to maximize ionic conductivity. Since an excessive or deficient amount of plasticizer decreases the ionic conductivity, it is crucial to find the optimized ratio of plasticizer. For example, Das et al. investigated the influence of the concentration of plasticizers on the ionic conductivity of

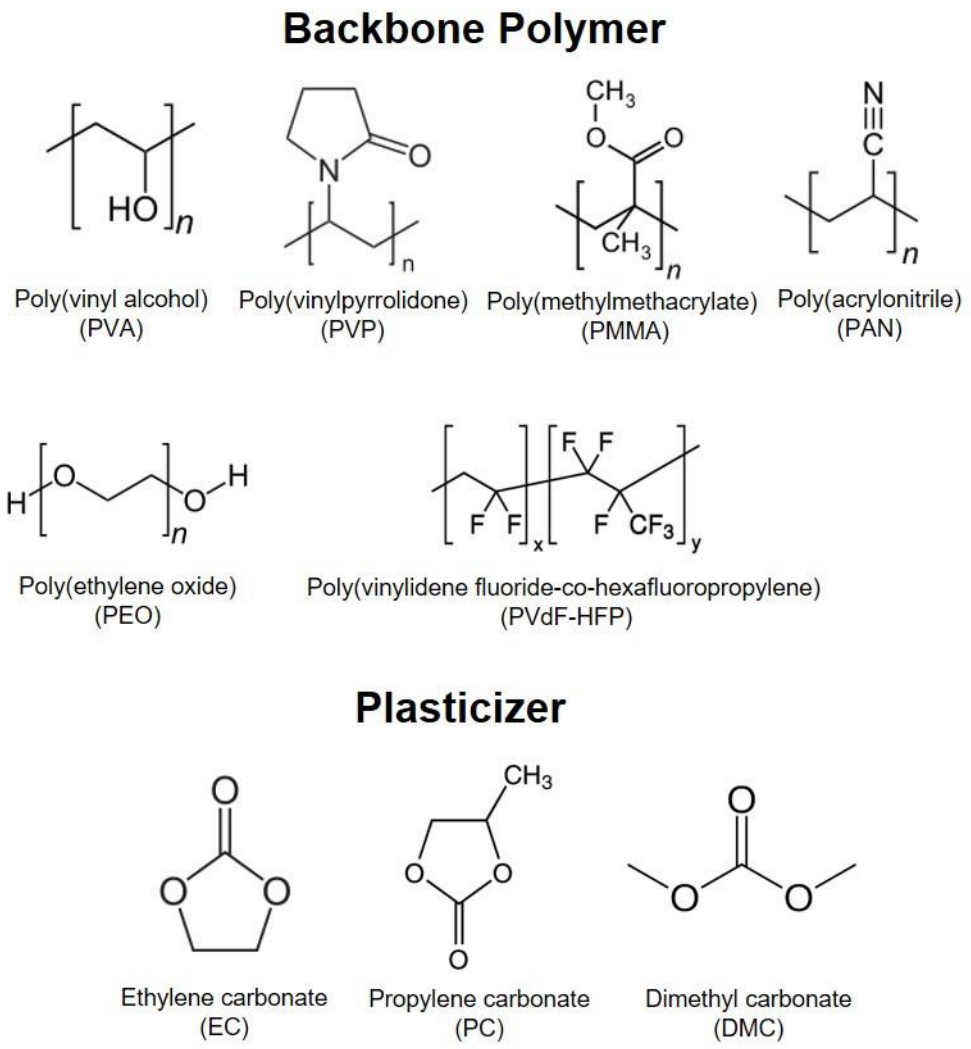

Figure 2-4. Molecular structures of backbone polymers and plasticizers

GPEs.[55] In this study, it is observed that the use of propylene carbonate as a plasticizer increases the ionic conductivity by dissociating salts and ion aggregates to make free conducting ions [55]. Moreover, the ionic conductivity reaches a peak at the concentration of the plasticizer of 40 %. In the excessive concentration of the plasticizer over 40 %, ionic conductivity decreases substantially due to the increase of neutral ion-pairs and aggregated ions [55–57]. In general, the ionic conductivity of GPEs is in the range of 10^{-4} to 10^{-3} S cm^{-1}, which is much higher than that of SPEs.

On the other hand, there are some drawbacks to the use of plasticizers. Due to the swollen polymer matrix, the physical strength of GPEs is much weaker than that of SPEs. Moreover, flash point and electrochemical stability are low as well [48]. However, despite those drawbacks, GPEs have been intensively studied and utilized in various applications due to high ionic conductivity.

Polyelectrolytes

Polyelectrolytes are binary systems of backbone polymer and salts but differentiated with SPEs. The backbone polymer of polyelectrolyte consists of polycations or polyanions, which can dissociate salts. The dissociated ions interact with the charged species on branched groups of polyions. Polyelectrolytes are therefore different from SPEs, in which ions coordinate with donor atoms on backbone polymers. The counterions interact with polyions and facilitate a transfer to neighboring charged species by the segmental movement of backbone polymers. The ion-hopping mechanisms of SPEs and polyelectrolytes are similar, but the states of ions coordinating with donor atoms in SPEs or interacting with polyions in polyelectrolytes are different.

Among polyelectrolytes, Nafion® membrane (DuPont and Sigma-Aldrich Corp.) is the most representative polyelectrolyte. Nafion was invented in the late 1960s and has been produced by DuPont [58]. Nafion has perfluorinated backbone polymers with sulfonic acid groups branching from them as shown in Figure 2-5. Due to its excellent electrochemical stability, mechanical properties, and high ionic conductivity, Nafion has been mainly applied to a proton exchange membrane of fuel cells [59]. A proton exchange membrane fuel cell (PEMFC) is an energy conversion system to produce electricity by means of electrochemical reactions of hydrogen oxidation and oxygen reduction. In the PEMFC, Nafion plays an important role in transporting proton ions (H^+) from the anode to the cathode and insulating electricity. Moreover, it has outstanding thermal and mechanical strength, which are essential for the fabrication of membrane electrode assembly (MEA). For this reason, Nafion has been mainly used to the membrane of PEMFCs. There has been no better polyelectrolyte than Nafion for PEMFCs, as of yet, even though many research groups have tried to develop a more advanced polyelectrolyte.

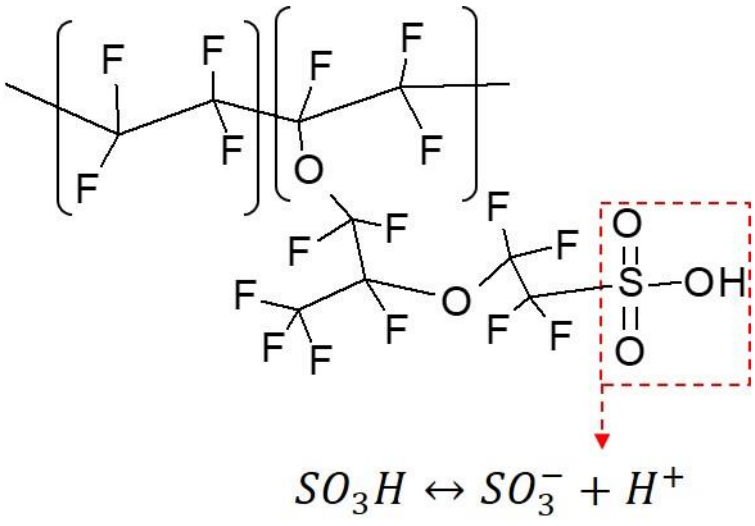

Figure 2-5. Chemical structure of Nafion

Composite Polymer Electrolytes

Composite polymer electrolytes (CPE) are advanced polymer electrolytes consisting of polymer, salts, and inorganic materials. The inorganic materials are electrochemically inert nanoparticles called fillers, e.g., $LiAlO_2$, MgO, SiO_2, and Al_2O_3 [60]. The nanoparticle fillers highly influence the material properties of the CPE. Capuano et al. reported that nanoparticle fillers of γ-$LiAlO_2$ drastically improve morphological and electrochemical properties in the composition of PEO/$LiClO_4$ [61]. Moreover, the nanoparticle fillers reduce the degree of crystallinity by dispersing into polymer structures and preventing the agglomeration of polymer chains [61]. However, although the addition of nanoparticle fillers in PEs can improve ionic conductivity, an excessive concentration of them rather reduces the ionic conductivity [61]. Therefore, the optimization of the ratio of these components is important. Moreover, high dielectric constants of nanoparticle fillers facilitate the dissociation of salts to make free lithium ions [62]. In addition, thermal stabilities, interfacial contacts, and mechanical properties are also improved by the addition of nanoparticle fillers [48]. As above, nanoparticle fillers have a great influence on the properties of CPEs. For this reason, many research groups have investigated the CPEs for many electrochemical devices like batteries, fuel cells, and supercapacitors [62–64].

Table 2-3. Materials properties of backbone polymers, plasticizers, and salts

Backbone Polymer	**Abbreviation**	**Chemical formula**	**Melting point [°C]**	**Glass transition temperature (T_g) [°C]**	**Density [g cm^{-3}]**	**Solubility in water**
Poly(vinly alcohol)	PVA	$(C_2H_4O)_n$	200	85	1.19	Soluble
Poly(methylmethacrylate)	PMMA	$(C_5O_2H_8)_n$	160	105	1.18	Insoluble
Poly(vinylpyrrolidone)	PVP	$(C_6H_9NO)_n$	150	130 - 175	1.2	Soluble
Poly(acrylonitrile)	PAN	$(C_3H_3N)_n$	300	95	1.184	Insoluble
Poly(ethylene oxide)	PEO	$(C_2H_4O)_n$	65	–67	1.12	Soluble
Poly(vinylidene fluoride)	PVDF	$(C_2H_2F_2)_n$	175	–35	1.76	Insoluble
Plasticizer	**Abbreviation**	**Molar mass [g mol^{-1}]**	**Melting point [°C]**	**Flash point [°C]**	**Density [g cm^{-3}]**	**Dielectric constant**
Ethylene carbonate	EC	88.062	34 - 37	150	1.321	90 at 40°C
Propylene carbonate	PC	102.08	–48.8	132	1.205	64.92
Dimethyl carbonate	DMC	90.078	2 - 4	21.7	1.069	3.087
Diethyle carbonate	DEC	118.13	–74.3	33	0.975	2.82
Dimethyl formamide	DMF	73.095	–60	58	0.948	36.7
Salt	**Abbreviation**	**Molar mass [g mol^{-1}]**	**Melting point [°C]**	**Density [g cm^{-3}]**	**Solubility in water**	
Lithium bis(trifluoromethane-sulfonyl)imide	LiTFSI	287.075	236	1.33	Soluble	
Lithium perchlorate	$LiClO_4$	106.39	236	2.42	Soluble	
Sodium perchlorate	$NaClO_4$	122.44	468	2.49	Soluble	
Lithium sulfate	Li_2SO_4	109.94	859	2.22	Insoluble	
Lithium trifluoro-methanesulfonate (or lithium triflate)	LiOTf or LiTf	156	> 300	1.9	Soluble	
Lithium hexafluorophosphate	$LiPF_6$	151.905	200	1.5	Soluble	
Lithium tetrafluoroborate	$LiBF_4$	93.75	293 – 300	0.852	Soluble	

2.2.2. Ion Gels

For decades, many types of polymer electrolytes (PE) have been studied and applied to electrochemical devices. However, the low ionic conductivity of PEs remains a shortcoming. Until now, most studies of PEs have only focused on the modification of polymers or optimization of component ratios without any remarkable contribution, and the development of new PEs seems to have reached a plateau. However, the advent of ion gels hints at a new possibility for the development of solid-phase electrolytes.

Ion gels can be classified as a new category of solid-phase electrolytes that consist of backbone polymers and ionic liquids (ILs) (Figure 2-6). Ion gels have been developed to overcome the drawbacks of PEs with the intrinsic properties of ILs. Ion gels have distinct characteristics that are different from the PEs. First, the ILs used in ion gels play the role of both the electrolyte and the conducting ions. Therefore, it is not necessary to use any additional salts. However, depending on the applications, salts can be added into the ion gels with the ILs. Secondly, the polymer structures of the PEs and the ion gels are different. The polymer structures of ion gels have cross-linked junctions forming a 3-dimensional polymeric matrix, whereas polymer structures of PEs are agglomerated due to Van der Waals interactions and the weak physical entanglement of polymers. The cross-linked polymeric structures capture the ILs and swell to form the ion gels.

Figure 2-6. Image of chemically cross-linked ion gel

Ion gels have very unique advantages, because their properties can be easily tailored by ILs. As described in the previous section, the properties of ILs can be modified by simply replacing cations or anions depending on the application. This tailorable property also applies to ion gels. For this reason, the properties of ion gels, such as ionic conductivity and electrochemical stability, can be easily modified by substituting the appropriate ILs. In addition, those properties are affected

by other factors like polymer structures and composition ratio. Due to these tailorable properties, ion gels have been used in many applications such as batteries, printed electronics, and supercapacitors [52,65,66].

Classification of Ion Gels by Cross-Linked Structures

Ion gels are classified into two types as physically cross-linked (PC) or chemically cross-linked (CC) ion gels. Depending on the cross-linked structures, ion gels have different properties and synthesis procedures. The ion gels should have cross-linked junctions to form 3-dimensional polymer structures through absorbing ILs and swelling. These cross-linked junctions structured by physical entanglement or covalent bonds of polymers classify the types of ion gels (Figure 2-7).

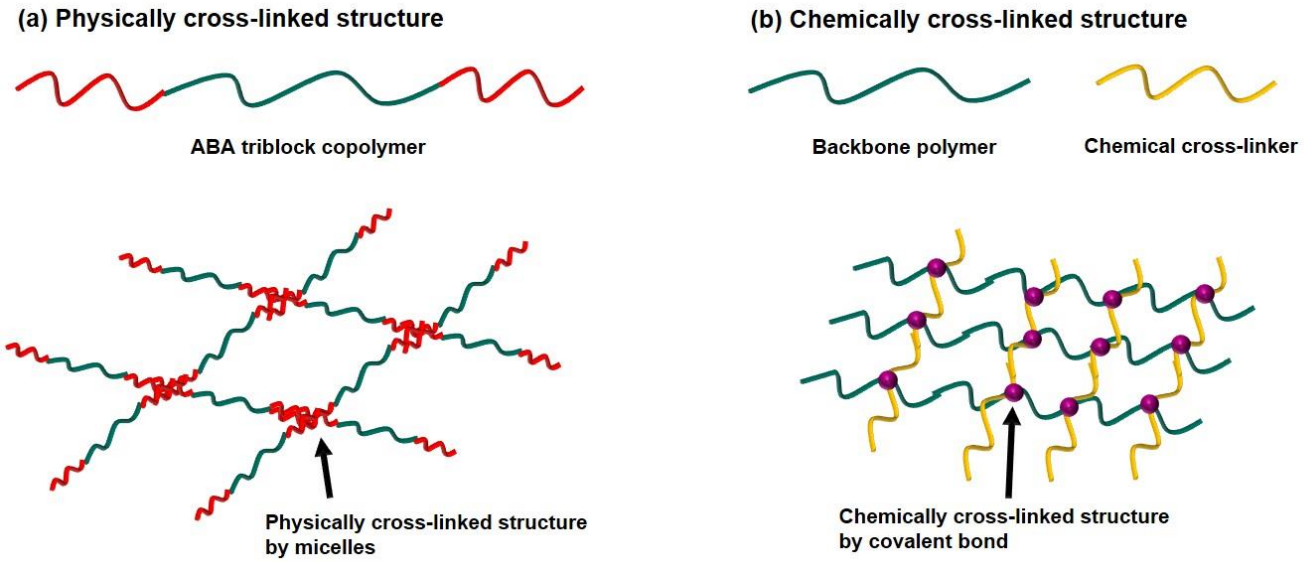

Figure 2-7. Illustration of (a) physically cross-linked structure and (b) chemically cross-linked structure

Most of the PC ion gels are based on the micellization of ABA triblock copolymers, in which blocks consisting of repeating units of A or B monomers are linked as a pattern of A-B-A. The PC ion gels have physically cross-linked junctions with micelles of ABA triblock copolymers and form 3-dimensional polymeric networks. These PC junctions are different from the structures of PEs, which have a solid phase by Van der Waals interactions and weak polymeric entanglement of backbone polymers. ABA triblock ion gels have been considered cutting-edge PC ion gels. The key mechanism to prepare ABA triblock ion gels is to use the selective solubility of ABA triblock copolymers. The PC junctions with ABA triblock copolymers are structured by micellizations and selective dissolution of A and B blocks [67–69]. The A block polymers are insoluble, whereas the B block polymers are soluble in solvents [67,68]. These insoluble A block polymers form the micellar cores with other A block polymers and make physical cross-linking junctions [67]. The B block polymers also act as a bridge junction [67]. The PC ion gels utilize this partial micellization by the

A block of the triblock copolymer system. Consequently, the PC structures absorb ILs in the matrix and therefore become PC ion gels.

The innovative work from the groups of Frisbie and Lodge has paved the way for the new field of ABA triblock ion gels. They first utilized the selective solubility and micellization of ABA triblock copolymers to synthesize PC ion gels. Lodge's group developed the PC ion gels, and Frisbie's group applied the PC ion gels to electrolyte-gated transistors as a gate insulator. Their collaborations have marked significant achievements in the development of the PC ion gels. In 1990, Balsara et al. in Lodge's group studied the micellization of poly(vinyl pyridine)-polystyrene-poly(vinyl pyridine) (PVP-PS-PVP) triblock copolymers, in which an insoluble mid-block polymer of PS against the solvent forms the core of the micelle surrounded by the solvated polymer of PVP [70]. Based on this study, in 2007, they developed ABA triblock ion gels combining poly(styrene-block-ethylene oxide-block-styrene) (PS-PEO-PS) triblock copolymer with 1-butyl-3-methylimidazolium hexafluorophosphate ([BMIM][PF_6]) [71]. Lee et al. in Frisbie's group developed polymer thin-film transistors using a triblock copolymer of PS-PEO-PS and an ionic liquid of 1-butyl-3-methylimidazolium hexafluorophosphate ([BMIM][PF_6]) [72]. In this study, the PC ion gel of the PS-PEO-PS triblock copolymer shows a high gate capacitance of 40 μF cm^{-2} at 10 Hz and a much faster polarization response time compared to solid polymer electrolytes (SPE) [72]. In addition, Cho et al. reported low-voltage polymer thin-film transistors using PC ion gels consisting of PS-PEO-PS and 1-ethyl-3-methyl imidazolium bis(trifluoromethane sulfonyl)imide ([EMIM][TFSI]) as a gate insulator [73]. Since then, there have been numerous studies to develop triblock ion gels by many groups.

On the other hand, CC ion gels contain CC junctions made by covalent bonding in polymer structures. Without physical entanglement, micellization, or aggregation, 3-dimensional polymeric matrices are structured by covalent bonds. In general, the CC junctions are induced by annealing [74], UV-curing [75,76], or radical polymerization [77]. For instance, Susan et al. reported the synthesis method of CC ion gels using the vinyl monomer of methyl methacrylate (MMA) and [EMIM][TFSI] through in-situ radical polymerization, exhibiting high ionic conductivities around 10^{-3} S cm^{-1} [77]. Moreover, in a few studies, PC ion gels are modified to form CC junctions through the processes of annealing or UV-curing. Gu et al. reported that PC ion gels are annealed to make CC junctions and to enhance their toughness, and these show the improved physical strength and high ionic conductivity of 10^{-3} S cm^{-1} at room temperature [74]. Furthermore, Choi et al. synthesized CC ion gels by curing PC triblock ion gels with UV irradiation [75]. Aside from those, there have been many studies into developing CC ion gels. However, CC ion gels have a major drawback; polymer structures are not reversible and are difficult to use for the fabrication of electronic devices. Therefore, most of the studies are focused on material synthesis.

As stated, ion gels can be classified into either PC or CC ion gels. In comparison with PC ion gels, CC ion gels have better mechanical properties and thermal stability because the micelles of

ABA triblock copolymer are thermoreversible. However, CC ion gels are relatively more challenging to be applied to devices due to irreversible polymer structures created through covalent bonding.

2.3. Printed Electronics

For decades, the field of printed electronics has received attention since progress in manufacturing and printing techniques was achieved. Printing is one of the most promising approaches to fabricate electronic circuits. It is fast, easy, and cost-effective, and suitable to manufacture large-scale and flexible electronics on various substrates such as a wide variety of papers, plastics, and fabrics. These advantages further enable the development of flexible substrates for wearable applications or for internet of things (IoT) devices that are also low-power. Therefore, the field of printed electronics has been the focus of interest as one of the possible future of electronics. Related studies have been extensively reported.

Various manufacturing techniques for printed electronics have been developed to achieve high resolution, fast, and large-area printing. Typically, screen printing, ink-jet printing, aerosol-jet printing, and roll-to-roll (R2R) printing are utilized to fabricate printed electronic devices. Screen printing uses the push-through process, in which the printed inks are spread and filled in patterns on the screen plate by blading [80]. Screen printing is cheap, versatile, and convenient to fabricate patterns. The printing resolution of screen printing is generally in the range of 30-100 μm and can be further improved up to a value of 10 μm using a metal screen [80,81]. Ink-jet printing is one of the most preferred techniques for the fabrication of printed electronics. Ink-jet printing, called drop-on-demand (DOD) printing, is classified into thermal and piezoelectric DOD printing. Thermal DOD printing is used to generate bubbles in the ink by heating and then press it out of the nozzle [80]. On the other hand, in piezoelectric DOD printing, the ink is ejected by applying the voltage to piezoelectric materials, generating a pressure pulse in the ink [80]. Ink-jet printing has the benefit of economically producing printed electronics without the loss of materials, unlike screen printing. Moreover, the manufacturing process is simple, precise, and suitable for large-area, mass production. Aerosol-jet printing is a relatively new technique compared to screen or ink-jet printing. The aerosol is ejected by pressurized inert gas (e.g., N_2) and printed with high printing resolution (<5 μm). However, the availability of solvent which has a low boiling point, inert gas pressure, and related parameters should be carefully controlled for printing [80]. Therefore, aerosol-jet printing has a drawback in terms of the complicated processes involved despite high printing resolution. Roll-to-roll (R2R) printing is a classic printing technology, most suitable for high-volume, large-scale, and continuous manufacture of printed electronics. The rotating roll stamps the ink and fabricates electric circuits on the substrate. There are several types of R2R printing techniques such as gravure printing, flexographic printing, rotary screen printing, and offset printing. The printing resolution of the rotary screen printing is relatively lower than the others, while the gravure printing displays the

highest printing resolution comprising of a range of 1 to 8 μm [80]. As discussed above, many types of printing techniques have been developed and applied to the fabrication of printed electronics. In this thesis, the piezoelectric DOD printing is used for the fabrication of electrolyte-gated transistors as an application of the new ion gel described in Chapters 4 and 5.

Many types of applications, such as sensors, solar cells, and flexible displays, adopt printing techniques for their fabrication. Notably, the printing technique is mainly utilized to fabricate transistors, which are the key active components of electronic devices. The transistor plays the role of controlling current flows and represents the basic unit in the logic gate. Transistors consist of gate dielectrics, semiconducting channels, and electrodes of drain, source, and gate. The conventional transistors adapted for computers or smartphones use inorganic semiconductors and gate dielectrics, most preferably silicon (Si) and silicon dioxide (SiO_2). Si-based transistors are manufactured by patterning electric circuits on Si wafers through intricate etching and photolithographic processes. In general, silicon oxide (SiO_2) or high-k materials (e.g., HfO_2, $ZrSiO_4$, or ZrO_2) are adapted as gate dielectrics. Although the inorganic-based gate dielectrics have outstanding gating performance of low leakage current and fast switching speed, they have a drawback: the manufacturing process is rather complicated. Moreover, the inorganic-based semiconducting channel and gate dielectrics are brittle and not flexible, thereby not suitable for wearable, low-operating potential, or flexible devices. For this reason, as an alternative to inorganic-based transistors, electrolyte-gated transistors (EGT) are highlighted because they use flexible polymer electrolyte as a gate insulator, instead of high-k or silicon oxide.

In these subsections, the fundamentals of MOSFETs and EGTs are discussed. First, the operational mechanism of the MOS capacitor and the MOSFET is discussed, and the related equations for the electrical parameters are explained. Then, the structure and features of the EGT are introduced in detail.

2.3.1. Metal Oxide Semiconductor Field-Effect Transistor (MOSFET)

The metal oxide semiconductor field-effect transistor (MOSFET) is the primary system of modern electronics. The MOSFET was first discovered in the 1930s by Lilienfeld [82]. He developed the fundamental structure of the MOSFET consisting of copper sulfide (semiconductor), aluminum foil (source, drain, and gate electrodes), and glass substrates. This structure is very simple because there was no lithography technology at that time. However, since then, the structures of MOSFETs have been developed and have thereby resulted in modern, standard transistors adapted in all electronic devices today. This subsection introduces the MOSFET.

Before describing the MOSFET, the MOS capacitor should be first explained to understand the operational mechanism of the MOSFET. The MOS capacitor has a metal oxide semiconductor structure consisting of three layers stacked on top of each other as depicted in Figure 2-8. The metal is a gate electrode, and the oxide consists of gate dielectrics (SiO_2 or high-k materials). The MOS capacitor operates by applying gate voltage (V_g) to change the state of the semiconductor, which results in the formation of three different states: surface accumulation, depletion, and inversion. Surface accumulation means that there is a charge accumulation of majority carriers at the interface of the semiconductor. It occurs when the opposite charge carriers are accumulated at the interface of the gate electrode. In the case of P-type substrate (Figure 2-8), the holes, which are majority carriers in P-type substrates, accumulate when the V_g lower than the flat band voltage (V_{fb}) is applied. The V_{fb} is the voltage at which the accumulated charges in the semiconductor and gate electrode offset each other and generate no electric field on the gate dielectrics. When the V_g is higher than V_{fb}, the holes are pushed away from the accumulation surface and depleted. This depletion layer increases by the repulsive force when the V_g increases. When the V_g is higher than the threshold voltage (V_{th}), minority carriers, which are the electrons, are accumulated at the interface, and make an inversion layer. This inversion layer is utilized as a N-type current channel of the MOSFET. These transitional states of semiconductors controlled by the V_g are the mechanism of the MOS capacitor. In the case of the N-type substrate of the MOS capacitor, the majority and minority charges are electrons and holes, respectively. Surface accumulation also occurs when V_g is higher than V_{fb}, and inversion occurs when V_g is lower than V_{th}.

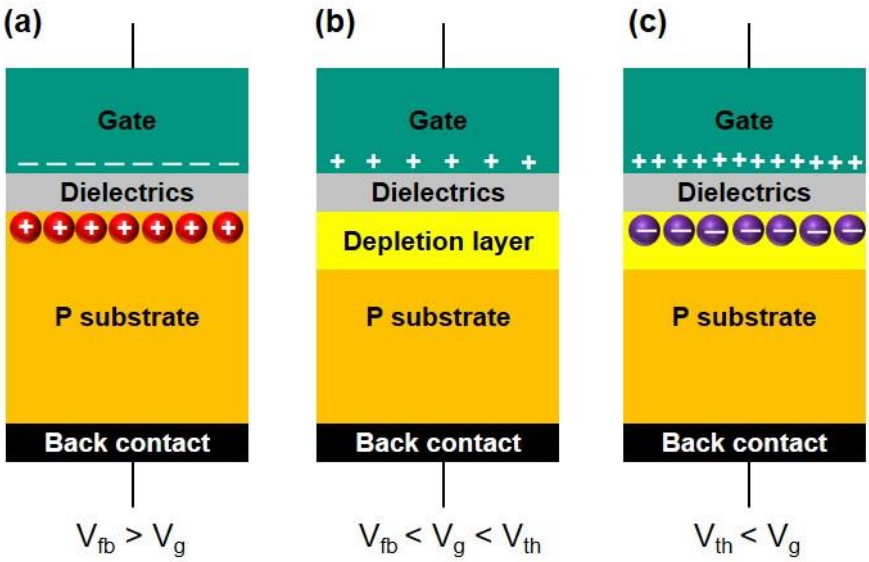

Figure 2-8. Illustration of n-type metal-oxide-semiconductor (MOS) capacitor (P-type substrate); (a) accumulation, (b) depletion, and (c) inversion

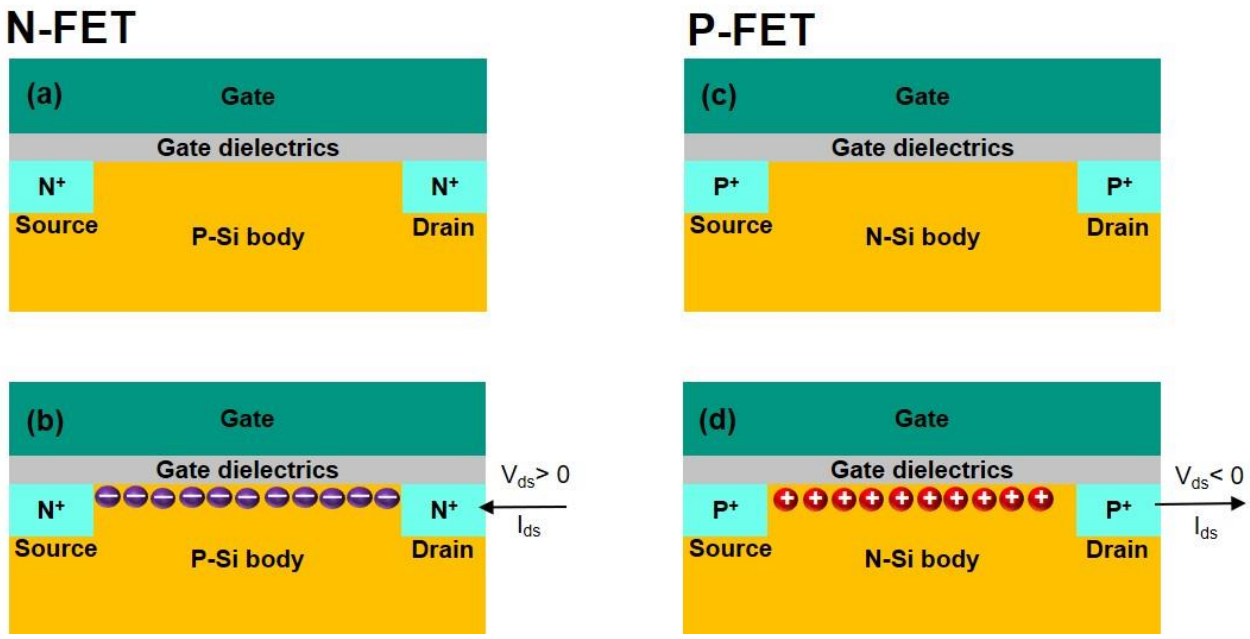

Figure 2-9. Illustration of (a) off- and (b) on-states N-channel MOSFET and (c) off- and (d) on-states P-channel MOSFET.

The MOSFET is a current control structure developed from the MOS capacitor. It has additional components of source and drain electrodes in the semiconductor. The source and drain electrodes play the role of connecting the external circuits and induce the current flow through the channel of the semiconductor. Figure 2-9 shows the N-type channel or the P-type channel MOSFETs (N-FET and P-FET). In this thesis, ion gels and polymer electrolytes are applied to N-type EGTs. Therefore, the N-FET mechanism is primarily described here. In the N-FET, the current is controlled not only by V_g but also by drain-source voltage (V_{ds}). The applied V_g switches the current channel in the semiconductor on/off. The current flowing through the channel is controlled by the V_{ds}. The higher the V_g or V_{ds}, the more current flows. When the V_g or V_{ds} are higher than specific voltages, the current becomes saturated (Figure 2-9).

The accumulated charge and drain-source current (I_{ds}) can be calculated with the following equations. First and foremost, the charges accumulated in the inversion layer can be calculated using Equation 2.1 [82].

$$Q_{inv}(x) = -C_{oxe}\left(V_{gs} - mV_{cs} - V_{th}\right) \tag{2.1}$$

$$\mathrm{m} = 1 + \frac{C_{dep}}{C_{oxe}} = 1 + \frac{3T_{oxe}}{W_{dmax}} \tag{2.2}$$

Q_{inv} is the accumulated charge in the inversion layer. C_{dep} and C_{oxe} are capacitances at the depletion layer and the oxide, respectively. T_{oxe} is the oxide thickness, and W_{dmax} is the maximum thickness of the inversion layer. V_{gs}, V_{cs}, V_{th} are the gate-source, channel-source, and threshold voltages,

respectively. To obtain a rough estimate, m can be assumed to have a value of Equation 2.1 can be used for the calculation of the I_{ds} (Equation 2.3) [82].

$$I_{ds} = \mathrm{W} \cdot Q_{inv}(x) \cdot v = W \cdot Q_{inv} \cdot \mu_{ns} \cdot E \quad (2.3)$$

$$= \mathrm{W} C_{oxe}\left(V_{gs} - mV_{cs} - V_t\right)\mu_{ns}\frac{dV_{cs}}{dx} \quad (2.4)$$

μ_{ns} is electron surface mobility, and E is the electric field in the channel. X is the channel length. If the above equation is integrated along the channel length from 0 to L, it can be expressed as below [82].

$$\int_0^L I_{ds}\,\mathrm{dx} = \mathrm{W} C_{oxe}\mu_{ns}\int_0^{V_{ds}}\left(V_{gs} - mV_{cs} - V_t\right)dV_{cs} \quad (2.5)$$

$$I_{ds}\mathrm{L} = \mathrm{W} C_{oxe}\mu_{ns}\left(V_{gs} - V_t - \frac{m}{2}V_{ds}\right)V_{ds} \quad (2.6)$$

Equation 2.6 can be simplified depending on the linear region or saturation region as below [82].

$I_{ds} = \frac{W}{L}C_{oxe}\mu_{ns}\left(V_{gs} - V_t - \frac{m}{2}V_{ds}\right)V_{ds}$, if $V_{ds} \leq V_{gs} - V_{th}$ (Linear region) (2.7)

Equation 2.7 is the equation for I_{ds} in the linear region when the value of $V_{gs}–V_{th}$ is much higher than V_{ds}. If I_{ds} is saturated and dI_{ds}/dV_{ds} is zero, the saturated V_{ds} (V_{dsat}) can be expressed as below [82].

$$V_{dsat} = \frac{V_{gs} - V_t}{m} \quad (2.8)$$

In the saturation region, when V_{ds} is much higher than $V_{gs}–V_{th}$, the saturated I_d (I_{dsat}) can be expressed as below.

$I_{dsat} = \frac{W}{2mL}C_{oxe}\mu_{ns}\left(V_{gs} - V_t\right)^2$, if $V_{ds} > V_{gs} - V_{th}$ (Saturation region) (2.9)

Equation 2.7 and 2.9 are mainly used to calculate the I_{ds} of N-FET.

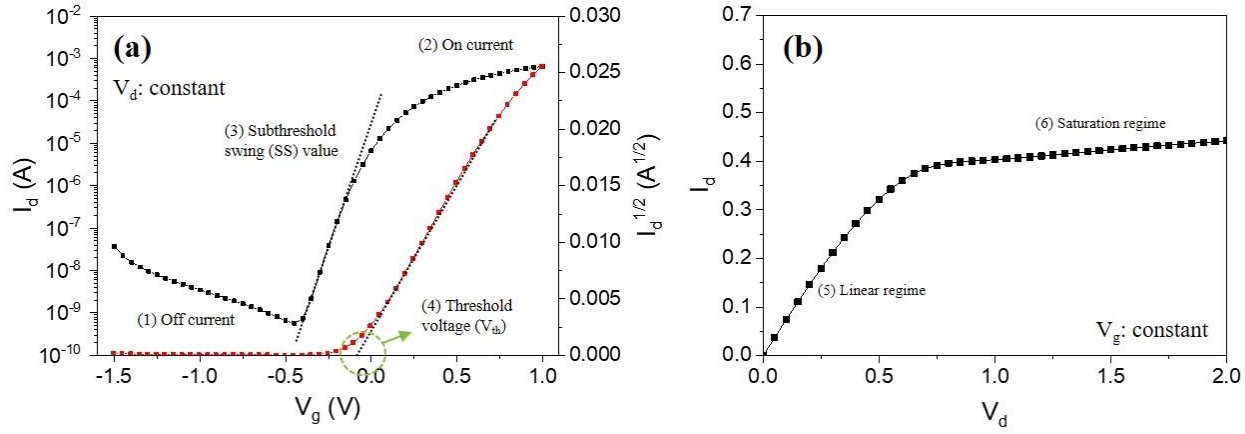

Figure 2-10. Transfer curves of NFETs; (a) drain-source current (I_d) versus gate voltage (V_g) and (b) I_d versus drain voltage (V_d).

Figure 2-10 shows the transfer curves of the N-FET. The electrical parameters of off-current (I_{off}), on-current (I_{on}), subthreshold swing (SS), and threshold voltage (V_{th}) are shown in the transfer curves. The primary function of the MOSFET is to turn the current flow open or close the current flow. Therefore, it is essential to measure the values of I_{on} or I_{off}. The I_{off} and I_{on} can be observed in the transfer curve (Figure 2-10(a)). In the ideal case, when the channel is closed, there should be no leakage current to prevent power consumption in the off-state. However, in real cases, there is a leakage current, and its value appears as the I_{off}. In the on-state when the channel is opened, the current flows according to the V_d or V_g. The I_{on} increases rapidly when the channel is opened. Upon increasing V_g over V_{th}, the I_{on} rises and approaches saturation as shown in Figure 2-10. The on/off current ratio is a crucial parameter to compare the electric performance of FETs. It can be calculated by the ratio of I_{on} with I_{off} (I_{on}/I_{off}) to create a dimensionless number.

The subthreshold swing (SS) is the value indicating the speed at which the N-FET is switched on/off. This SS value can be calculated by Equation 2.10 or 2.11 [83].

$$SS = \ln 10 \frac{dV_{gs}}{d(\ln I_d)} \tag{2.10}$$

$$SS = \ln 10 \left(\frac{k_b T}{q}\right)\left(\frac{C_{oxe}+C_{dep}}{C_{oxe}}\right) \tag{2.11}$$

The mathematical meaning of the SS value is the slope of $\ln(I_d)$ and V_g with a higher value indicating a faster switching speed between I_{on} and I_{off} by V_g.

The threshold voltage (V_{th}) of the N-FET is the minimum voltage required to start opening the current channel in the semiconductor. It can be calculated by the extrapolation of $I_d^{1/2,}$ as shown in Figure 2-10(a). The field-effect mobility (μ) is the value indicating how quickly charges of electrons or holes move through a current channel in an electric field. It can be calculated by Equation 2.6 or 2.7 using the values of channel width (W), length (L), and capacitance (C_{oxe}).

2.3.2. Electrolyte-Gated Transistor (EGT)

The electrolyte-gated transistor (EGT) was first developed in the 1950s but has not been used in mainstream applications for a long time [53]. On the other hand, the MOSFET has been used as a standard transistor in modern electronic devices. Recently, however, the MOSFET is considered not to be suitable for flexible printed electronics, and now the EGT has attracted much more attention and has been studied by many researchers. This thesis deals with the EGT as the main application of polymer electrolyte and ion gel. In this subsection, the fundamentals and structures of the EGT are introduced in comparison with the MOSFET.

Figure 2-11 shows the structure of the EGTs. The structural difference between the EGT and the MOSFET is the gate insulator. In the MOSFET, inorganic materials like SiO_2 or high-K materials are used as gate dielectrics, which generates the capacitance by dielectric polarization. On the other hand, EGTs use electrolytes to drive the capacitance through the mechanism of electric double layers (EDLs). The EDLs are created by the accumulation of ions at the interface of the electrolyte and the electrodes. When the electric field is applied, the ions migrate and accumulate on the interface. The polarization by accumulated ions form the EDL.

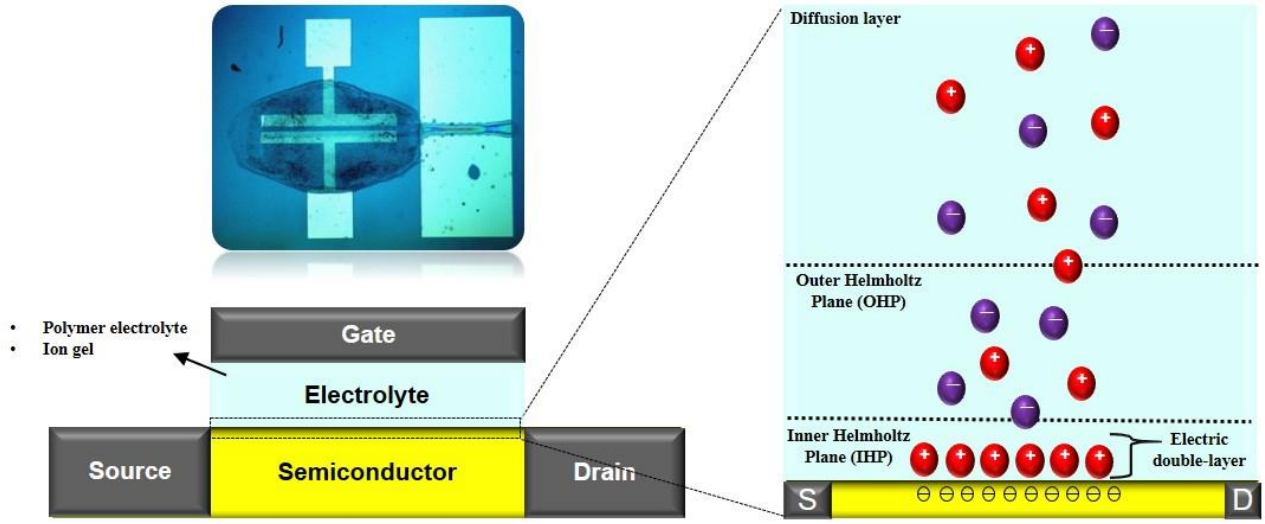

Figure 2-11. Illustration and image of electrolyte-gated transistor

In 1853, Hermann von Helmholtz et al. first established the fundamental model of electrode polarization and the formation of EDLs [84]. However, this model could not explain the influence of ion diffusion. Since then, diverse models have been developed by many groups, and through these efforts, the Stern, and Grahame models were established. The Stern model is the advanced version of the Helmholtz model. Stern et al. added the factor of ion diffusion in his model [85]. Furthermore, the Grahame model suggests the concept of inner and outer Helmholtz planes (IHP and OHP) [86]. These concepts of IHP and OHP are required to understand the formation of EDLs, and Grahame and Stern's models have been widely used in the modeling studies of EDLs.

Table 2-4. Lists of capacitance and phenomena

Capacitance [F]	**Phenomena**
10^{-12}	Bulk
10^{-11} to 10^{-8}	Grain boundary
10^{-10} to 10^{-9}	Bulk ferroelectrics
10^{-7} to 10^{-5}	Electric double-layer (EDL)
$>10^{-4}$	Electrochemical reaction

Although the transitional mechanisms of the semiconductor in the EGT and the MOSFET are the same, their properties are different because of the capacitances from the electrolyte and inorganic dielectrics. In the MOSFET, gate dielectrics drive the capacitance by bulk ferroelectric or grain boundary capacitances, which use the polarization of atoms in the electric field. However, the EDLs are generated through the accumulation of ions and possess a capacitance in the range of ~10 μF cm^{-2}, which is much higher than that of inorganic dielectrics (Table 2-4) [53]. For this reason, the EGT can operate in low V_g (< 2V) and is suitable for low-power devices. Moreover, another difference is flexibility. Inorganic gate dielectrics are brittle and have a risk of cracking when the substrate is bent. However, in the EGT, the polymer electrolyte or ion gel is elastic and physically stable in the flexible substrate. This flexibility of the EGT broadens the applicability to various wearable, flexible devices. The printing process can also produce the EGT, whereas the manufacture of the MOSFET requires a high temperature and complex etching processes. As above, the EGT has many advantages using gate insulators of polymer electrolyte or ion gel in comparison with the MOSFET.

On the other hand, the slow switching speed is considered to be a critical drawback of EGTs. It results from the slow speed of the formation of the EDL. In general, the ionic conductivity of polymer electrolyte is in the range of 10^{-5} to 10^{-2} S cm^{-1}. However, that is still not enough to achieve a switching speed comparable to that of the MOSFET. For this reason, diverse types of gate insulators have been developed to enhance the ionic conductivity and the speed of EDL formation.

Chapter 3

3. Experimental

This chapter describes the experimental techniques, methodologies, and sample preparations involved. Each section gives a brief description of how the experimental techniques were utilized and how the samples were prepared for the characterization. The electrochemical impedance spectroscopy (EIS), scanning electron microscopy (SEM), and Fourier-transform infrared (FTIR) spectroscopy are described. Especially, fundamental knowledge of EIS and FTIR spectroscopy are described in detail because they are essential for the characterization of polymer electrolytes and ion gels. Moreover, the ink preparation and fabrication process of electrolyte-gated transistors (EGTs) are introduced.

3.1. Fundamentals and Measurement of Electrochemical Impedance Spectroscopy (EIS)

Electrochemical impedance spectroscopy (EIS) is an essential technique for the investigation of polymer electrolytes (PE) and ion gels. Notably, the EIS technique is useful in analyzing the properties of materials and electrode-electrolyte interfacial phenomena such as capacitance, ionic conductivity, permittivity, and frequency-dependent behavior. In the analysis of the EIS, alternating current (AC) potential is applied to the sample, and the response of phase-shifted currents is measured. Applied AC potentials and phase-shifted currents are measured as sinusoidal functions (Equation 3.1 and 3.2, and Figure 3-1), and from Ohm's law (V=IR), those can be written as Equation 2.3.

$$E_t = E_0 \sin(wt) \quad (3.1)$$

$$I_t = I_0 \sin(wt + \phi) \quad (3.2)$$

$$Z = \frac{E_t}{I_t} = \frac{E_0 \sin(wt)}{I_0 \sin(wt+\phi)} = Z_0 \frac{\sin(wt)}{\sin(wt+\phi)} \quad (3.3)$$

ϕ is phase angle, I_0 and E_0 are amplitudes, and w is radial frequency. By Euler's relationship($e^{j\phi} = \cos\phi + j \cdot \sin\phi$), Equation (3.3) can be also expressed as

$$Z(w) = \frac{E_t}{I_t} = \frac{E_0 exp(jwt)}{I_0 exp(jwt-\phi)} = Z_0(\cos\phi + j\sin\phi) = Z' + jZ'' \quad (3.4)$$

$$|Z| = \sqrt{Z'^2 + Z''^2} \quad (3.5)$$

The resistance Z(w) is a function of frequency and contains real and imaginary parts of the impedance (Z' and Z''). The Z' and Z'' measured from the EIS analysis can be interpreted by the equivalent circuit.

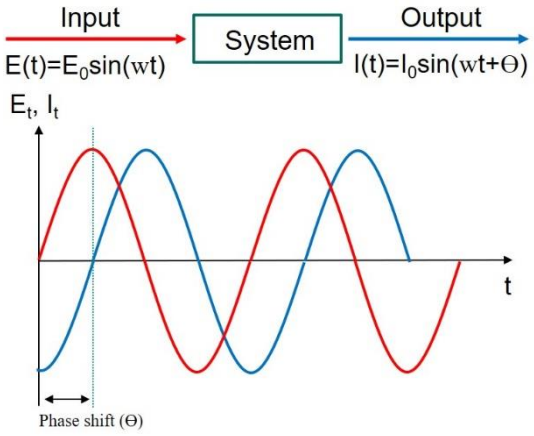

Figure 3-1. Input of applied potential (E_t) and output of phase-shifted current response (I_t) in EIS analysis

Equivalent Circuit

An equivalent circuit is a theoretical, electrical circuit that helps interpret the result of EIS more accurately and precisely. The measured data from EIS can be converted to the processed results allocated to each electrical element using the equivalent circuit. Therefore, designing a correct equivalent circuit fitting to the materials and systems is a crucial part of the EIS analysis because circuit design can dramatically affect the interpretation of the results. This subsection introduces equivalent circuits.

Table 3-1. The elements of equivalent circuits

Equivalent element	Resistor (R)	Capacitor (C)	Inductor (L)	Warburg element (W)	Constant phase element (CPE)
Impedance	R	$\frac{1}{jwC}$	jwL	$\frac{1}{Y_0\sqrt{(jw)}}$	$\frac{1}{Y_0(jw)^a}$
Admittance	$\frac{1}{R}$	jwC	$\frac{1}{jwL}$	$Y_0\sqrt{(jw)}$	$Y_0(jw)^a$

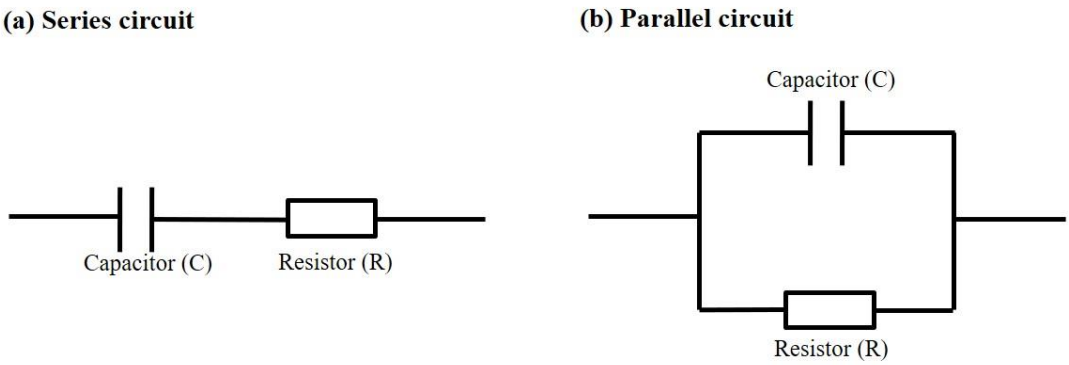

Figure 3-2. Examples of equivalent circuits; (a) series circuit and (b) parallel circuit

The electrical elements of an equivalent circuit are listed in Table 3-1. Electrical elements are therefore combined, based on the principle of equivalent circuits. In equivalent circuits, electrical elements are allocated into series or parallel circuits, as shown in Figure 3-2. The resistor (Z_R) and capacitor (Z_C) can be written as Equation 3.6 and 3.7 following Ohm's law.

$$Z_R(w) = \frac{V(t)}{I(t)} = R \tag{3.6}$$

$$Z_C(w) = \frac{V(t)}{I(t)} = \frac{1}{jwC} = \frac{-j}{wC} \tag{3.7}$$

j is an imaginary number, C is the capacitance, and ω is the applied frequency. In series equivalent circuits containing the resistor and the capacitor, the real and imaginary parts (Z' and Z'') are given by Equation 3.9 [87].

$$Z = Z_R + Z_C \tag{3.8}$$

$$Z = R_{si} - \frac{j}{wC} = Z' + jZ'' \tag{3.9}$$

Equation 3.9 contains Z' and Z'' converted to electric elements of the resistor and the capacitor in series. Z' and Z'' correspond to the ohmic resistance in series (R_{si}) and $-j/wC$, respectively. On the other hand, Z' and Z'' in the parallel equivalent circuit containing the resistor and the capacitor can be expressed by Equation 3.14 [87].

$$\frac{1}{Z} = \frac{1}{Z_R} + \frac{1}{Z_C} \tag{3.10}$$

$$\frac{1}{Z} = \frac{1}{R_p} + jwC = \frac{1+jwCR_p}{R_p} \tag{3.11}$$

$$\frac{1}{Z} = \frac{(jwR_PC+1)(jwR_pC-1)}{R_p(jwR_pC-1)} = \frac{-(w^2R_p^2C^2+1)}{R_p(jwR_pC-1)} \tag{3.12}$$

$$\mathrm{Z} = \frac{-(jwR_p^2C-R_p)}{w^2R_p^2C^2+1} \tag{3.13}$$

$$\mathrm{Z} = \frac{R_p}{w^2R_p^2C^2+1} + \frac{-R_p^2jwC}{w^2R_p^2C^2+1} = Z' + jZ'' \tag{3.14}$$

R_p is the polarization resistance in a parallel circuit. As above, Z' and Z'' can be expressed differently depending on electrical elements and circuit design. For this reason, the precise modeling of an equivalent circuit suitable for the desired materials and systems is important to extract the required parameters of electrical elements.

Nyquist Plot

The Nyquist plot, which was first suggested by Nyquist in 1932, is a polar coordinate system plotting impedance responses of real and imaginary parts (Z' and Z'') [88]. The Z' is plotted as the X-axis against the –Z'' on the Y-axis. The Nyquist plot is useful to investigate electrochemical phenomena at a glance because it displays responses from the whole frequency ranges on a single plot. In this section, the Nyquist plot of the parallel equivalent circuit of the capacitor and the resistor is explained. Moreover, the Randles circuit, used as a standard circuit for the analysis of interfaces, is discussed.

The equivalent circuit in Figure 3-3(a) is the parallel circuit containing a resistor and a capacitor. The electrical elements and related equations of parallel equivalent circuits have already been

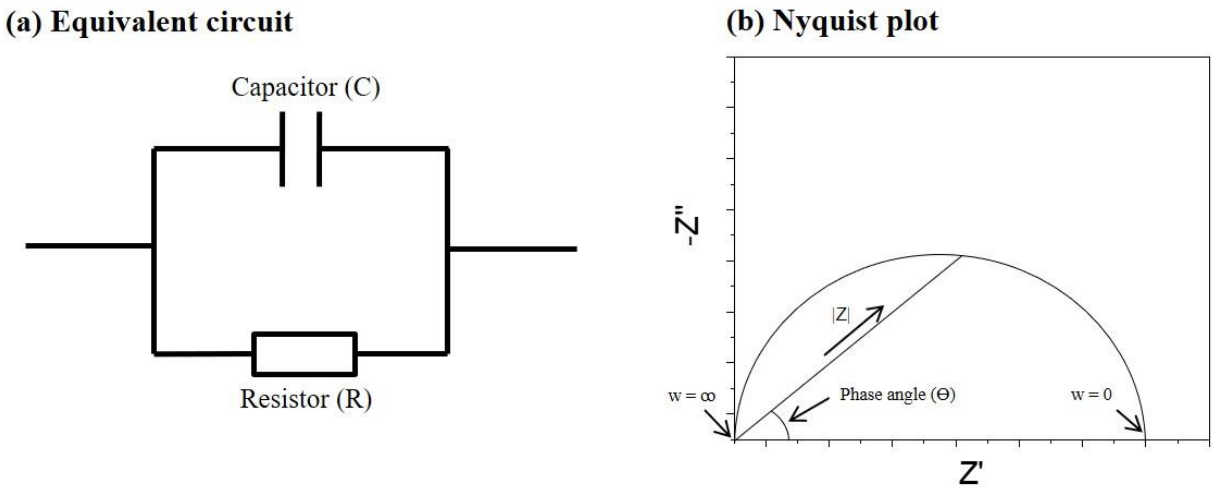

Figure 3-3. (a) Equivalent circuit of resistor and capacitor in parallel and (b) Nyquist plot

discussed in the previous subsection. Figure 3-3(b) shows the Nyquist plot of the parallel equivalent circuit. In infinite frequency (w = ∞), the values of Z' and –Z'' converge to 0. The influence of the capacitor is negligible, and the response of the resistor is dominant in the high-frequency range. However, the value of –Z'' increases by the influence of capacitance as frequency decreases. This value of –Z'' also converges to 0 when the frequency approaches 0. This variation of Z' and –Z'' by frequency draws the semicircle plot as shown in Figure 3-3(b). This semicircle plot has an important meaning in the analysis of the EIS.

The Randles circuit, designed by Randle in 1947, is the primary equivalent circuit used to analyze the interface between the electrolyte and the electrode [89]. The Randles circuit is useful to analyze interfacial phenomena between the electrode and electrolyte. The Randles circuit contains electric elements of electric-double layer capacitance (C_{dl}), solution resistance (R_s), charge transfer resistance (R_{ct}) (or polarization resistance), and the Warburg element (Z_w). Figure 3-4 shows the Randles circuit and Nyquist plot. R_{ct} and Z_w are placed in series, and C_{dl} is connected with them in parallel. An R_s element is also placed in series with their parallel circuits.

- Solution resistance (R_s): ohmic resistance of the solution
- Charge transfer resistance (R_{ct}): resistance from charge transfer
- Electric double-layer capacitance (C_{dl}): capacitance by charge accumulation at the interface
- Warburg element (Z_w): diffusional impedance of charge carriers

In Figure 3-4, the R_s is the ohmic resistance of the solution. The R_{ct} is the resistance of the charge transfer during the faradaic redox reaction ($M \leftrightarrow M^{n+} + ne^-$) at the interface. The R_{ct} can be calculated using the diameter of the semicircle plot in the Nyquist plot. The C_{dl} can be replaced with the composite phase element (CPE) (Table 3-1). There may be a discrepancy between the theoretical and the experimental values, even if the equivalent circuit is appropriately designed for the system and materials. The CPE can adjust this deviation. The Warburg element (Z_W) is related to the diffusion

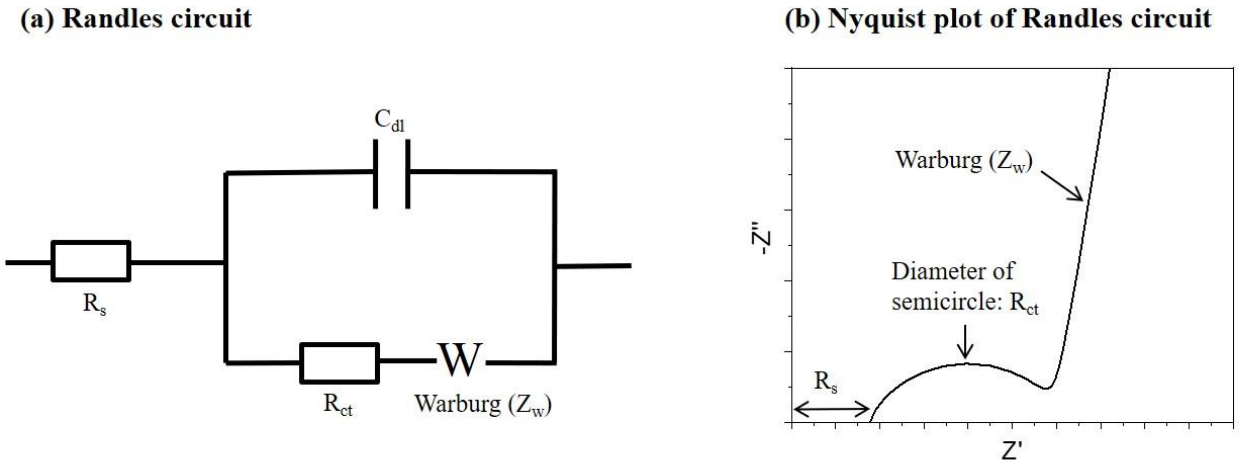

Figure 3-4. Randles circuits. (a) equivalent circuit and (b) Nyquist plot

of charge carriers from the bulk electrolyte to the electrode [90]. Warburg impedance is negligible in the high-frequency range. However, it should be considered in the low-frequency range because the mass transport of charge carriers can limit the electron transfer [91]. Straight diagonal lines following semicircle is a result of the Warburg element (ideal = 45º). If the Warburg element is ignored, the equivalent circuit in Figure 3-4(a) can be expressed by the equations below [91].

$$Z(w) = R_s + \frac{R_p}{1+jwR_pC} \tag{3.15}$$

$$= R_s + \frac{R_p}{1+w^2R_p^2C^2} - \frac{jwR_p^2C}{1+w^2R_p^2C^2} = Z' + jZ'' \tag{3.16}$$

If the Warburg element is considered, the Randles circuit can be written by Equation 3.17.[91]

$$\mathrm{Z(w)} = R_s + R_p\left(1 + \frac{\lambda}{\sqrt{2w}}\right) - CR_p^2\lambda^2 - \frac{j\lambda R_p}{\sqrt{2w}} \tag{3.17}$$

$$\lambda = \frac{\kappa_f}{\sqrt{D_O}} + \frac{\kappa_b}{\sqrt{D_R}} \tag{3.18}$$

κ_f and κ_b are forward and backward electron transfer constants, and D_O and D_R are oxidant and reductant diffusion coefficients [91]. The Randles circuit is useful to analyze interfacial phenomena in electrochemical applications as a basic model.

The Randles circuit is, therefore, a useful tool to investigate a faradaic system like lithium-ion batteries. However, it is not suitable for non-faradaic systems like electric double-layer capacitors (EDLCs). For example, EDLCs do not have redox reactions occurring at the interface, and primarily the accumulation of charges occurs. The charge transfer resistance observed in the EDLC is interpreted as an interfacial leakage current [92]. Therefore, the equivalent circuit should be modified to fit the non-faradaic system, and thereby the interpretation of results should be different. For this reason, there have been many model studies of equivalent circuits and interpretations for EDLCs [92,93].

This thesis deals with polymer electrolytes and ion gels, which form electric double layers (EDLs) and proposes how to further apply them to electrolyte-gated transistors, which are non-faradaic systems. Therefore, it is not appropriate to use the Randles circuit. Moreover, the Nyquist plot is not the best method for the analysis of frequency-dependent behavior because the frequency is not indicated in the plot. Rather than the Nyquist plot, the Bode plot is more suitable to investigate the frequency-dependent behavior of polymer electrolyte and ion gels.

Bode Plot for the Analysis of Polymer Electrolytes or Ion Gels

The Bode plot is a useful graph to investigate frequency-dependent behaviors. Herein, the explanation of the Bode plot focuses on the analysis of polymer electrolytes (PE) and ion gels. In the Bode plot, the x-axis is the frequency, and two y-axes are log(|Z|) and phase angle (º). The advantage of the Bode plot is that it displays all the responses by the applied frequency in a graph, making the interpretation of frequency-dependent behaviors much easier. For this reason, the Bode plot is more preferred for the analysis of PE or ion gel than the Nyquist plot.

In the Bode plot (Figure 3-5), PE or ion gels show three different behaviors depending on the frequency: (1) formation of electric double-layers (EDL), (2) ion migration, and (3) dipole relaxation of polymers. In the Bode plot (Figure 3-5), the phenomena of dipole relaxation are observed in the high-frequency range (region (3)). In this range, permanent or induced dipoles on polymers are aligned in applied electric fields by segmental movement. In the lower frequency range (region (2)), dipole relaxation phenomena do not occur, and bulk resistance (R_{bulk}) from ion migration is measured. In this range, due to the insufficient time, the conducting ions cannot migrate to the interface of the electrode to form EDLs [92]. The R_{bulk} is independent according to the frequency and shows a plateau in the log (|Z|) versus frequency plot. As the frequency decreases and approaches values lower than that of R_{bulk}, the ions can accumulate and form the EDLs at the interface between the electrode and the electrolyte. For the EDLs, the value of (|Z|) linearly increases as the frequency decreases because the ions have more time to be accumulated to form the EDLs.

The variation of frequency-dependent behaviors can be also determined with the phase angle (º). In a phase angle versus a frequency plot (Figure 3-5(b)), the phase angle of –45º is a datum line to determine capacitive or resistive behaviors [65,94]. In the range from –90º to –45º,

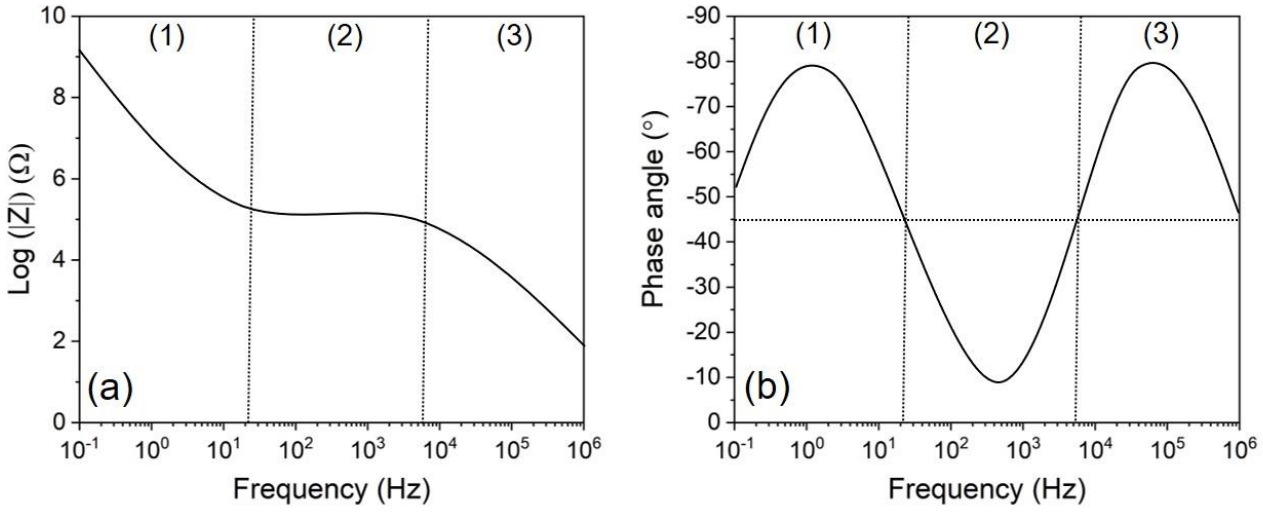

Figure 3-5. Bode plots of (a) log(|Z|) versus frequency and (b) phase angle (º) versus frequency plots.

PE or ion gels show capacitive behaviors corresponding to the phenomena of dipole relaxation and EDL formations [65,94]. The phase angle of –90° is an ideal capacitive response. A phase angle from 0° to –45° indicates resistive behaviors corresponding to the R_{bulk} [65,94]. As above, the Bode plot is useful to analyze frequency-dependent behaviors such as dipole relaxation, ion migration, and formation of EDLs. For this reason, the Bode plot is more useful for the analysis of PEs and ion gels.

Ionic Conductivity

Ionic conductivity is a noteworthy property to evaluate electrolytes. The ionic conductivity can be calculated based on the results of the EIS. Equation 3.15 calculates the ionic conductivity.

$$\sigma = \frac{d}{AZ'} \tag{3.15}$$

d and A are the thickness and surface area of the sample. Z' is the real part of the impedance. The calculated ionic conductivity varies with the frequency because the Z' is dependent on the frequency. Therefore, the variation of ionic conductivity can be interpreted by associating it with the frequency-dependent behavior observed in the Bode plot.

Figure 3-6 is a typical plot of *a.c.* ionic conductivity of PEs against the frequency. This plot displays *a.c.* and *d.c.* ionic conductivities ($\sigma_{a.c.}$ and $\sigma_{d.c.}$) varied by the frequency. The plateau region in the plot corresponds to $\sigma_{d.c.}$. Both $\sigma_{a.c.}$ and $\sigma_{d.c.}$ can be modeled by Jonscher's power law (Equation 3.17) [95–97].

$$\sigma^* = \sigma' + j\sigma'' \tag{3.16}$$

$$\sigma_{a.c.}(w) = \sigma_{d.c.} + Aw^n \tag{3.17}$$

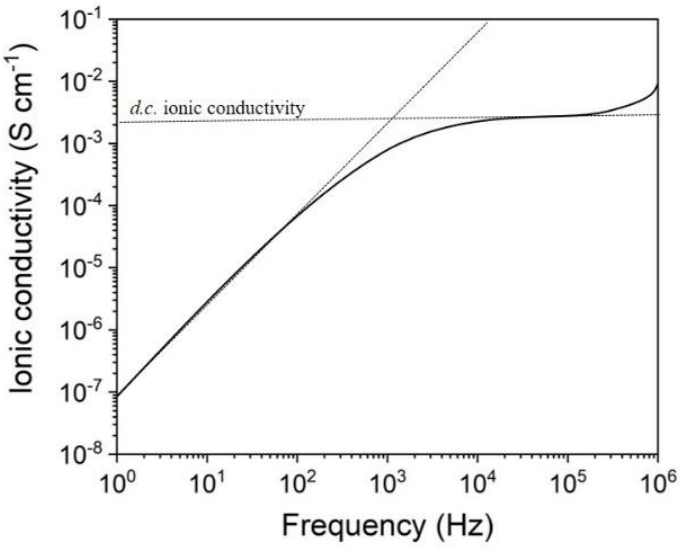

Figure 3-6. a.c. ionic conductivity (σ) versus frequency plot

σ^* represents a complex ionic conductivity. σ' and σ'' are the real and imaginary parts of ionic conductivity. j is an imaginary number. A and n are empirical fitting parameters. The tendency of ionic conductivity to vary according to the frequency is closely related to frequency-dependent responses such as dipole relaxation, ion migration, and formation of EDLs. The ionic conductivity in the higher frequency range than the region of $\sigma_{d.c}$ is affected by the phenomenon of dipole relaxation and can be classified as a dispersive region [95,96]. Due to dipole relaxation, the ionic conductivity increases as the frequency increases. The plateau region of $\sigma_{d.c.}$ also results from constant resistance of ion migration, corresponding to R_{bulk} in the Bode plot. In the low-frequency range, ionic conductivity decreases due to electrode polarization, where EDLs formed at the interfaces hinder the ion migrations [98].

Calculation of the Effective Capacitance

Effective capacitance (C_{eff}) is a capacitance calculated from the result of the EIS. In the case of PEs and ion gels, the C_{eff} mostly results from the capacitance of EDL (C_{dl}) because the capacitance driven by dielectrics of dipoles on polymers is negligible in comparison with the EDL. In general, the C_{eff} is calculated by Equation 3.18.

$$C_{eff} = \frac{-1}{2\pi f Z''} \tag{3.18}$$

f is frequency, and Z'' is an imaginary part of the impedance. In many studies, C_{eff} is generally calculated using Equation 3.18. However, this equation has a deviation in the high-frequency range, where dipole relaxation occurs. For this reason, in this thesis, Equation 3.23 is used for the calculation [99].

$$C_{eff} = C_0 \left(\frac{d}{WA\varepsilon_0}\right)\left(\frac{-Z''}{Z'^2+Z''^2}\right) \tag{3.19}$$

$$C_0 = \frac{A\varepsilon_0}{d} \tag{3.20}$$

$$C_{eff} = \left(\frac{A\varepsilon_0}{d}\right)\left(\frac{d}{WA\varepsilon_0}\right)\left(\frac{-Z''}{Z'^2+Z''^2}\right) = \frac{1}{W}\left(\frac{-Z''}{Z'^2+Z''^2}\right) = \frac{1}{2\pi f}\left(\frac{-Z''}{Z'^2+Z''^2}\right) \tag{3.21}$$

$$Z'^2 + Z''^2 = |Z|^2 \tag{3.22}$$

$$C_{eff} = \frac{-Z''}{2\pi f |Z|^2} \tag{3.23}$$

Although the C_{eff} calculated by Equation 3.18 and 3.23 have similar values in the low-frequency range, the one calculated by Equation 3.23 reduces the deviation with the results of the Bode plot in the high-frequency range.

Measurement of EIS for Polymer Electrolytes and Ion Gels

In this thesis, the EIS analysis was performed using Swagelok cells, which can be connected to the electrochemical measuring equipment, BioLogic (SP-200). Swagelok cells consist of stainless-steel electrodes, cell bodies, and cylinder parts. Inside the cell body, Kapton tape was inserted between the electrode/sample and the cell body for insulation. The ion gels were sandwiched with stainless electrodes and assembled with Swagelok cell parts. The ion gels were prepared as bulk films. For the preparation, ion gel ink was poured and uniformly spread on a glass substrate. After gelation, the film created by the ion gel was prepared as a disk with a diameter of 12 mm and assembled into the Swagelok cell.

The different materials were tested using different parameters. The bulk films of PVA/PEMA ion gel (see chapter 4) were cut into discs of a diameter of 12 mm (area: 1.13 cm^2), and assembled with two stainless steel electrodes in the Swagelok cells. The voltage amplitude was 10 mV, and the frequency was swept from 100 kHz to 1 Hz at low current range.

Adhesive ion gels (see chapter 5) were prepared as bulk films with a thickness of 0.76 mm and a diameter of 12 mm. The films were assembled with stainless steel electrodes and Swagelok cells. The frequency range was from 300 kHz to 1Hz, and the voltage amplitude was 10 mV.

3.2. Scanning Electron Microscopy (SEM)

Scanning electron microscopy (SEM) is a useful method to characterize the morphology, composition, and topography of the samples. Unlike optical microscopes, SEM utilizes an electron beam to raster the sample and forms the image using reflected secondary electrons from the surface of the sample. A secondary electron microscope consists of an electron gun, electromagnetic lens (condenser and objective lens), secondary electron detector, vacuum pump, etc. The electron gun generates electrons to form a beam. A beam of electrons is focused on the sample through a series of electromagnetic coils. The electron beam is injected onto the sample, and the detector collects the secondary electrons reflected from the conducting surface of samples. Through further signal processing, SEM images are generated.

In this thesis, the samples were prepared by completely drying the solvent in their polymeric structures of polymer electrolytes or ion gels due to the low pressure (below 10^{-5} to 10^{-7} Pa) required in the SEM chamber. In SEM images, the dried samples showed the surficial morphology of shrunk polymer structures because the solvents trapped in swollen polymer structures were removed during the drying process. A thin gold layer was sputtered onto the samples to make their surface electron conductive.

The morphology of ion gel (See chapter 4) was analyzed with a scanning electron microscope (SEM, ZEISS Leo 1530). The acceleration voltage used was 5 kV, and the magnification was 10000

times. The thin gold layer (10 nm) was sputtered on the samples by a Cressington Sputter Coater 108 auto.

3.3. Fundamentals and Measurement of Fourier-Transform Infrared (FTIR) Spectroscopy

Fourier transform infrared (FTIR) spectroscopy is a useful method to analyze molecular structures of polymers or organic compounds. The principle of FTIR analysis is to induce vibrational modes, such as stretching and bending, to asymmetrical diatomic molecules and measure the absorbed energies transferred by an IR laser. Compared to dispersive IR instruments, FTIR analysis is fast and very precise. Moreover, the measurement procedure is non-destructive and done at ambient conditions. In addition, the scanning is adjusted using only the moving mirror, and this simple mechanism minimizes the experimental effort and errors. Due to these advantages, FTIR analysis has been utilized in many research fields and has become an essential part of polymer research.

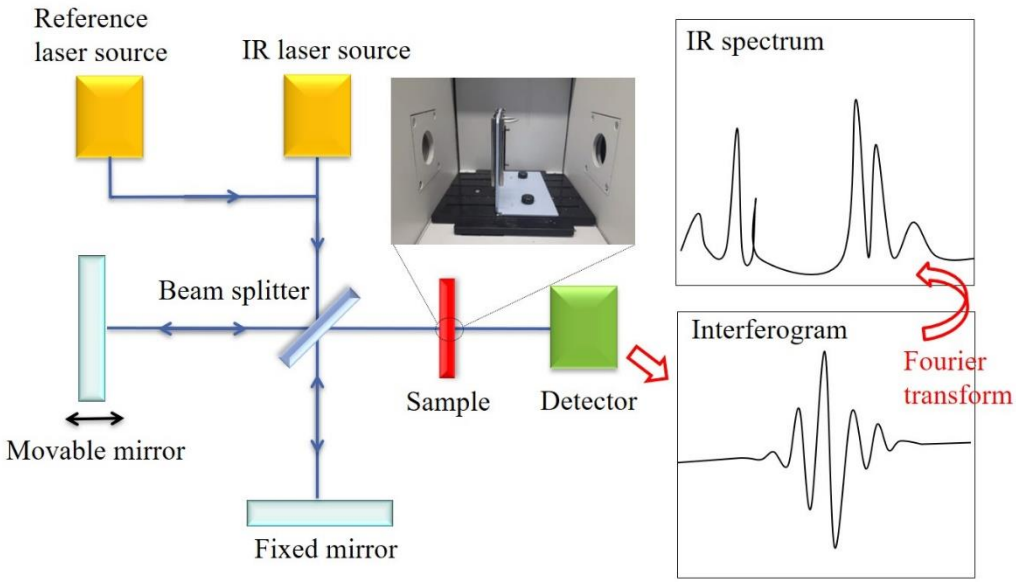

Figure 3-7. Schematic illustration of structure drawing of Fourier transform infrared (FT-IR) spectroscopy

The equipment of FTIR spectroscopy consists of four main parts: (1) IR and reference laser sources, (2) interferometer and beam splitter, (3) fixed and moving mirrors, and (4) detector (Figure 3-7). The measurement process is as follows. The IR and reference lasers are introduced from laser sources into the beam splitter of the interferometer. At the beam splitter, the injected laser is split in two directions, heading to moving and fixed mirrors. Both lasers are reflected by moving and fixed mirrors and meet again at the beam splitter. Doing so, the travel distance of both pathways can be varied and an optical path difference (OPD) created. This OPD results in constructive or destructive interference between the beams. The IR lasers contain broad ranges of frequencies for measurement, and the manipulation of moving mirrors induces the interference of each measured frequencies. The interfered wave spectrum generates the interferogram. After the interference, the

interfered beams go through the sample. At this time, the molecular structures of organic compounds or polymers absorb a certain amount of energy transferred from the IR laser to induce the vibrations of molecules [100]. The absorbed energy varies with molecular structures, structural symmetry, and electron distribution [100]. The detectors of FTIR read the variations of the interferograms between the initial and penetrated IR laser, and their interferograms are converted to the corresponding absorbance or transmittance IR spectra through the use of Fourier transforms. The absorbance peaks in IR spectra are displayed corresponding to the energy absorbed by the molecule structure.

FTIR analysis gives qualitative and quantitative information about the chemical composition of polymers [101]. The structural features of polymers such as the degree of crystallinity, orientation, inter/intramolecular bonding, functional groups, chain constitution, head/tail structures, end groups, and composition of copolymers can be identified with FTIR analysis [100,101]. Depending on the molecular structures and analysis purposes, the IR ranges are used differently. The IR ranges can be divided into three regions as shown below.

- **Near-IR range** (NIR, ν (wavenumber) = 13200-4000 cm^{-1}, λ = 0.76-2.5 μm)
- **Mid-IR range** (MIR, ν (wavenumber) = 4000-200 cm^{-1}, λ = 2.5-50 μm)
- **Far-IR range** (FIR, ν (wavenumber) = 200-10 cm^{-1}, λ = 200 μm-1 mm)

In the near IR (NIR) range, overtone and combinational vibrations are observed due to the imperfect harmonic molecular vibrations [100,102]. In this range, the large number of absorbance peaks are observed and overlapped to enable computational fitting. The structural features such as

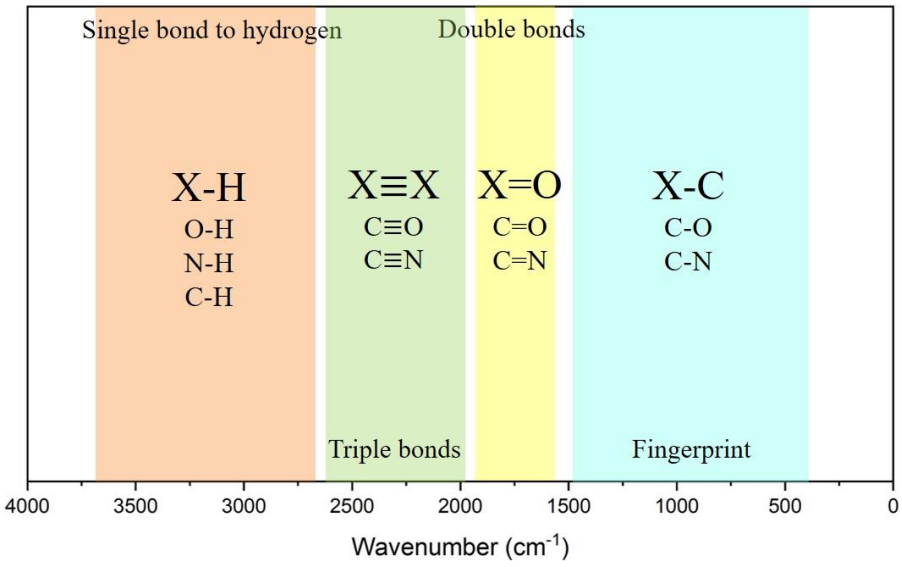

Figure 3-8. Intermediate IR range of EIS. The regions of single, double, triple and fingerprint bonds are notified depending on the wavenumber.

crystallinity, constitution, conformation, inter/intramolecular interaction, end group, molar mass, and particle sizes can be investigated in the NIR range [102].

FT-IR analysis in the NIR range is carried out for quantitative analysis due to the difficulty of qualitative analysis in this area. However, rather than the NIR range, the intermediate IR (MIR) range is more frequently used for polymer research because the vibrational motions of functional groups and related fingerprint peaks are detected in this range. The detectable molecular structures in the MIR range are as follow:

- 3700-2700 cm^{-1}: Single bond to hydrogen (X-H), O-H, N-H, and C-H
- 2700-1900 cm^{-1}: Triple bonds (X≡X), e.g., C≡O, C≡N
- 2000-1500 cm^{-1}: Double bonds (X=X), e.g., C=O, C=N
- 1500-400 cm^{-1}: Single bond (X-X) (Fingerprint region), e.g., C-O, C-N

As described above and in Figure 3-8, the peaks of single bond structures to hydrogen (X-H), e.g., O-H, N-H, and C-H, are identified in the range of 3700-2700 cm^{-1}. Moreover, the peaks of triple bonds and double bonds are detected in the range of 2700-1900 cm^{-1} and 2000-1500 cm^{-1}, respectively. The peaks in the fingerprint region of 1500-400 cm^{-1} are attributed to the single bond structures of molecules. Those contain the intrinsic peaks of molecular structures, allowing us to more easily establish the unknown polymer structures based on the reference data [100]. The far IR (FIR) range below 200 cm^{-1} is rarely used in the analysis of polymer structures.

Measurement of FT-IR Spectroscopy for Polymer Electrolytes and Ion Gels

In this thesis, FT-IR was utilized to characterize the ring-opening esterification between the hydroxyl group and cyclic anhydride for the ion gel synthesis. The samples were prepared differently, depending on the material properties, with the solution casting method or pelletization with potassium bromide (KBr). Most of the samples (from chapters 4 and 5) were prepared as a polymeric film by the solution casting method. However, poly(methyl vinyl ether-*alt*-maleic anhydride) (PMVE-MA) used in chapter 5 was prepared as a pellet by adding KBr and pressing using a hydraulic press because PMVE-MA is moisture-sensitive and it is challenging to make films due to its adhesive property.

The films of poly(vinyl alcohol) (PVA), poly(ethylene-*alt*-maleic anhydride) (PEMA), and PVA/PEMA polymeric gel and ion gels (see chapter 4) were prepared with the solution casting method. Dimethyl sulfoxide (DMSO) solvent was completely removed by heating for a few hours at 50 °C. The scan range of wavenumber is from 2000 cm^{-1} to 500 cm^{-1}, and the samples were scanned 12 times. The background baseline was removed.

Poly(methyl vinyl ether-alt-maleic anhydride) (PMVE-MA) (see chapter 5) was pelletized by blending with potassium bromide (KBr) powder and pressed using a hydraulic press as it is difficult

to make a polymeric film using PMVE-MA. Other polymers, such as PVA, PVE/PEMA-MA polymeric gel and ion gel, were prepared as films by the solution casting process. The DMSO solvent was completely dried at 50 °C for 5 hours. The samples were scanned 12 times in the wavenumber range from 2000 cm^{-1} to 500 cm^{-1}.

Table 3-2. IR absorption bands of organic functional groups used in chapters 4 and 5 [103,104].

Functional group		Band positions [cm^{-1}]	Type of vibration	Functional group		Band positions [cm^{-1}]	Type of vibration
Alcohol	O-H	3700-3584	Stretching	**Maleic Anhydride**	C=O	1857	Symmetric stretching
	O-H	3550-3200	Stretching		C=O	1783	Asymmetric stretching
	O-H	3300-2500	Stretching		C=C	1593	Stretching
	O-H	3200-2700	Stretching		C-O-C	1290	Deformation
	O-H	1420-1330	Bending		O-C=O	1268	Deformation
	C-O	1150-1050	Stretching		C-O-C	1242	Symmetric stretching
Carbonyl	C=O	1820-1670	Stretching			1060	In-plane ring vibration
Carboxylic acid	O-H	3300-2500	Stretching		O=C-O-C=O	872	Asymmetric deformation
	C=O	1760	Stretching			840	Out-of-plane ring vibration
	C-O	1720-1700	Stretching			697	In-plane ring vibration
	O-H	1440-1395	Bending	**Maleic acid**	C=O	1706	Stretching
Ester	C=O	1750-1735	Stretching		C=O and C=C	1636	Stretching
	C-O	1210-1163	Stretching		C=O and C=C	1598	Stretching
Alkane	C-H	3000-2850	Stretching		C=O and C=C	1569	Stretching
	-C-H	1480-1350	Bending		O-H	1460	Deformation
Alkene	=C-H	3100-3010	Stretching		O-H	1434	Deformation
	=C-H	1000-675	Bending		C-OH and C-H	1265	Stretching and deformation
	C=C	1680-1620	Stretching		C-OH	1220	Stretching
Aldehyde	C=O	1740-1720	Stretching		C-H	876	Out-of-plane deformation
	=C-H	2850-2820, 2750-2720	Stretching		C-H	864	Out-of-plane deformation

3.4. Ink Preparation for Electrolyte-Gated Transistors

In this thesis, components of the EGT such as the semiconductor, gate-insulator, and top-gate electrode, were produced by ink-jet printing. Four different inks were prepared for the fabrication of EGTs: (1) indium oxide precursor ink, (2) ink-jet printable PVA/PEMA ion gel ink (Chapter 4), (3) adhesive ion gel ink (Chapter 5), and (4) PEDOT:PSS ink. The ink-jet printable ink for chemically cross-linked ion gel is the highlight of this thesis. This section briefly describes the recipes and preparation methods, and more details are explained in Chapters 4 and 5.

The Ink Preparation of Indium Oxide Precursor

To prepare the semiconducting channel of indium oxide (In_2O_3), the indium oxide precursor inks were prepared as follows; 0.05M indium nitrate hydrate ($In(NO_3)_3 \cdot xH_2O$) was dissolved in 5 ml solvent consisting of 4 ml D.I. water and 1 ml glycerol. Glycerol was added to control the viscosity. The precursor ink was filtered with a polyvinylidene fluoride (PVDF) filter, which has a pore size of 0.45 μm. The printed precursor ink was annealed at 400 ºC for 2 hours to convert the precursor to the In_2O_3 channel.

The Ink Preparation of Ink-Jet Printable, Self-Assembled, and Chemically Cross-Linked Ion Gel

Two types of ion gel inks (dilute ink and viscous ink) were used depending on the purpose (see chapter 4). The dilute ink was developed for ink-jet printing. For the dilute ink of PVA/PEMA ion gel, 0.035 g of poly(vinyl alcohol) (PVA, Mw:100,000, Sigma Aldrich) and 0.015 g of poly(ethylene-*alt*-maleic-anhydride) (PEMA, Mw: 100,000-500,000, Sigma Aldrich) were separately dissolved in 2.5 ml of dimethyl sulfoxide (DMSO) and stirred for 2 hours at 60 ºC. After completely dissolving the PVA and PEMA in DMSO, the polymer solutions were cooled down to room temperature. Then, the two solutions were mixed and stirred for 2 hours at room temperature. The polymer solution in which PVA and PEMA are dissolved was filtered by a 13 mm syringe filter (Acrodisc, 0.45 μm Nylon membrane), and 83 μl of 1-ethyl-3-methylimidazolium trifluoromethanesulfonate ([EMIM][OTf], Sigma Aldrich) was added to the polymer solution.

The viscous ink was developed to produce the bulk film of PVA/PEMA ion gel for EIS measurement. For the synthesis of the bulk film of PVA/PEMA ion gel, 0.07 g of PVA and 0.03 g of PEMA are separately dissolved in 0.5 ml of DMSO and stirred for 2 hours at 60 °C. After mixing the solutions and cooling down to the room temperature, 166 μl of [EMIM][OTf] was added to the polymer solution. Before the gelation, the solution was poured on a glass substrate and the self-assembled gelation was allowed to finish. The ratios of PVA, PEMA, and [EMIM][OTf] are fixed and only the DMSO ratio is changed for bulk film preparation.

The Ink Preparation of Adhesive Ion Gel

For the synthesis of adhesive ion gel, poly(vinyl alcohol) (PVA, Mw: 100,000, Sigma Aldrich) and poly(methyl vinyl ether-*alt*-maleic anhydride) (PMVE-MA, Mw: 1,080,000, Sigma Aldrich) were separately dissolved in DMSO. The solutions were stirred at 60 ºC for 2-3 hours. After dissolution, the solutions were cooled down to room temperature, and 1-ethyl-3-methylimidazolium triflate ([EMIM][OTf], Sigma Aldrich) was added to PMVE-MA solution and stirred for 10 minutes at room temperature. Then, the two solutions were combined and stirred for a few minutes at room temperature. Before the solution was allowed to gelate, the ink was poured on a glass substrate and aged overnight. The weight ratio of ion gel ink is as follows; PVA : PMVE-MA : [EMIM][OTf] : DMSO = 5.6 : 1.4 : 16 : 77 wt%.

The Ink Preparation of Composite Solid Polymer Electrolyte (CSPE)

For the ink-jet printing process, the ink of composite solid polymer electrolyte (CSPE) was prepared. 0.3 g of poly(vinyl alcohol) (PVA) was dissolved in 6 g of dimethyl sulfoxide (DMSO) in solvent form. The solution was stirred at 60-80 ºC for a few hours to dissolve PVA. Then, 0.07 g of lithium perchlorate ($LiClO_4$) and 0.63 g of propylene carbonate were added into the solution and stirred overnight. Before printing, the solution was filtered using a poly(tetrafluoroethylene) (PTFE) filter (pore size: 0.2 μm) and printed using an ink-jet printer.

The Ink Preparation of PEDOT:PSS

Poly(3,4-ethylenedioxythiophene)-poly(styrenesulfonate) (PEDOT:PSS) is an intrinsically conductive polymer. Therefore, PEDOT:PSS was used as a top-gate material (see chapter 4). PEDOT:PSS ink was prepared by combining it with D.I. water. The mass ratio of PEDOT:PSS and D.I. water is 70:30. The ink was filtered with polyvinylidene fluoride (PVDF) filter (pore size: 0.45 μm) to prevent nozzle blockage. After ink-jet printing, the dropped-ink was dried to enable the evaporation of the water and solidify the top-gate electrode.

3.5. Fabrication of Electrolyte-Gated Transistors

The electrolyte-gated transistor (EGT) was fabricated with electron lithography and ink-jet printing techniques. The electrode patterning of gate, source, and drain was carried out by a pulsed infrared (IR) laser (Trumpf, TruMicro 5050) ablation or electron beam (e-beam) lithography (EBL). The electrode-patterned substrates (see chapter 4) were fabricated with EBL (Figure 3-9). For the patterning by EBL, the electron-sensitive resist was deposited using the spin-coating technique on a glass substrate. This electron-sensitive resist is selectively dissolved when an e-beam is injected on the defined areas. These selectively dissolved areas on the resist make electrode patterns on the substrate. After e-beam patterning, indium tin oxide (ITO) was deposited by atomic layer deposition, and a lift-off process removed the residual areas of resist. The electrode-patterned substrates (see

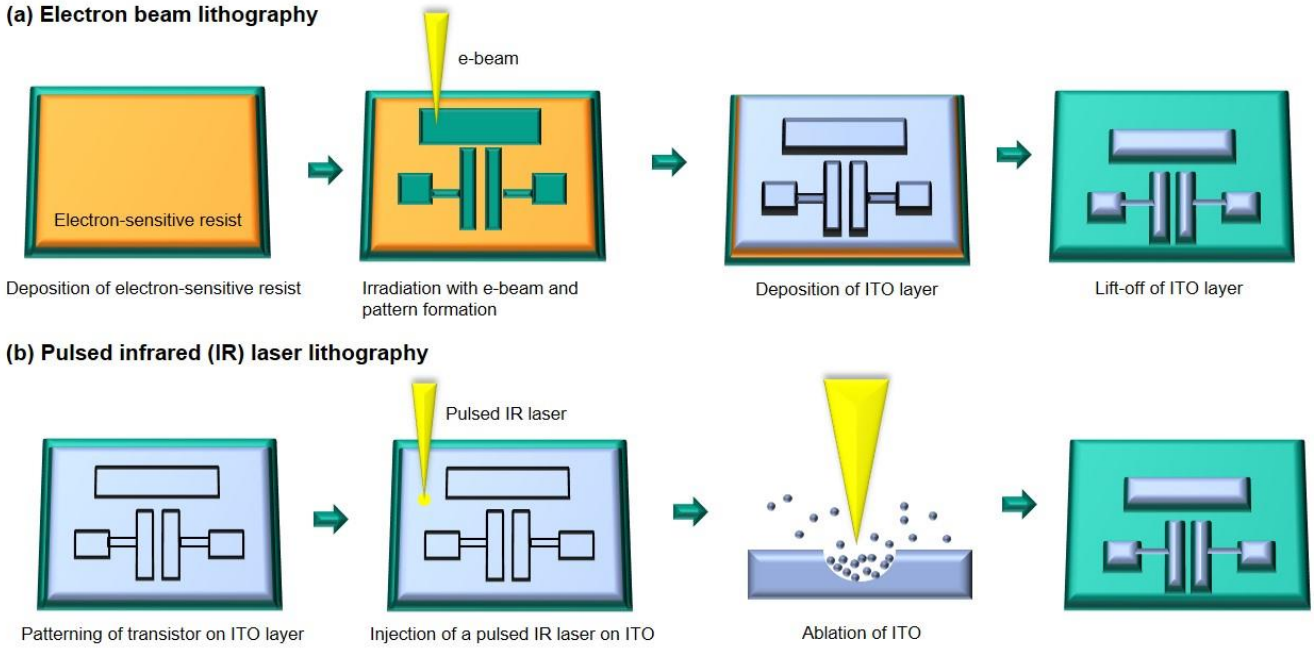

Figure 3-9. Fabrication processes of electrode-patterned substrate by (a) electron-beam lithography and (b) pulsed infrared (IR) laser lithography.

chapter 5) were prepared by a pulsed IR laser. Unlike the EBL, the patterning by a pulsed IR laser is a direct etching process. A pulsed IR laser emitted on the defined areas of ITO-deposited glass substrates ionizes ITO atoms by Coulomb explosion, and the ionized ITO in the exposed area is evaporated. Therefore, the ITO electrodes are patterned on substrates (Figure 3-9).

After the electrode preparation, the indium oxide precursor was printed by the ink-jet printer (Dimatix 2831). The precursor ink of indium oxide was filtered to prevent nozzle blockage before ink-jet printing. The precursor ink was printed between the source and drain electrodes, and the annealing process proceeded to transform to indium oxide (In_2O_3) into a semiconducting channel. The gate insulator was prepared by two methods (Figure 3-10); In chapter 4, the gate insulator was fabricated using the developed ion gel inks through the process of ink-jet printing. Moreover, in chapter 5, the gate insulator was fabricated by attaching the developed ion gel films (adhesive ion gel film) by hand to semiconducting channels and electrodes. After the fabrication of the gate insulator, PEDOT:PSS inks were printed by an ink-jet printer and dried to evaporate the D.I. water used as a solvent. (chapter 4)

E-beam lithography (EBL) was utilized to produce electrodes (see chapter 4). The channel width and length are 600 μm and 20 μm, respectively. An ink-jet printer (Dimatix 2831, Fujifilm) printed the indium oxide precursor ink filtered by the aforementioned polyvinylidene fluoride (PVDF) syringe filter (0.45 μm). After the ink-jet printing of the indium oxide precursor, the sample was annealed at 400 ºC for 2 hours to oxidize the precursor to form the semiconducting channels of indium oxide (In_2O_3). The ion gel or CSPE inks were printed on In_2O_3 channels. The temperatures of

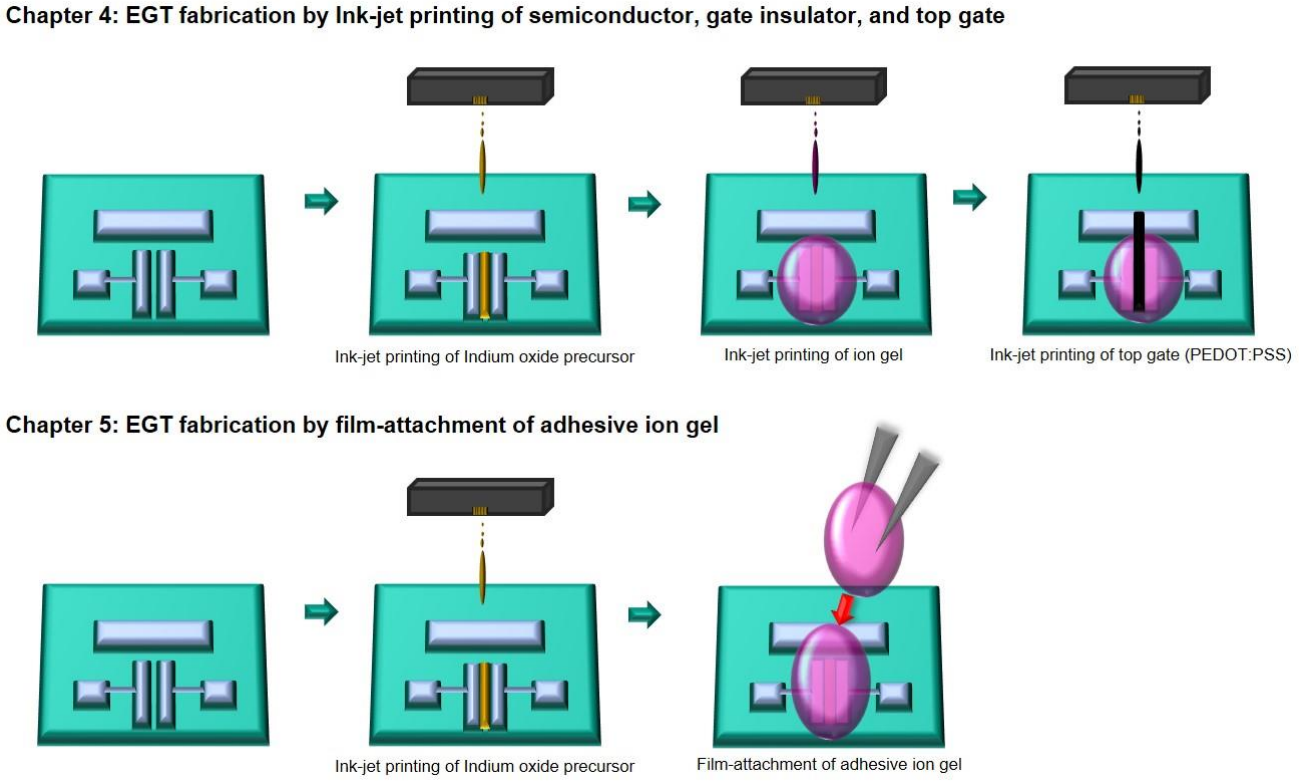

Figure 3-10. Fabrication processes of semiconducting channel, gate insulator, and top gate. In chapter 4, all the components are fabricated by ink-jet printing. In chapter 5, semiconducting channel is only printed by ink-jet printer and gate insulator (adhesive ion gel) is laminated by hand.

the nozzle and substrate were set to 25 °C and 40 °C, respectively. Poly(3,4-ethylenedioxythiophene)-poly(styrenesulfonate) (PEDOT:PSS) was printed as the top gate electrode and dried at 60 °C for 30 minutes.

The electrodes were prepared by a pulsed IR-laser (Trumpf, TruMicro 5000) (see chapter 5). The thickness of ITO deposited on a glass substrate is 150 nm. The channel width and length are 2 mm and 0.5 μm, respectively. Indium oxide precursor ink, in which 0.05 M of $In(NO_3)_3$, was dissolved into deionized water (D.I. water) with glycerol, and was printed by Sonoplot Microplotter on the patterned circuits. The sample was annealed at 400 °C for 2 hours. After the preparation of the electrode and the semiconducting channel, the adhesive ion gel film was simply attached to the substrate with tweezers. The fabricated EGTs were characterized by an Agilent 4156 C analyzer.

Chapter 4

4. Ink-Jet Printable, Self-Assembled and Chemically Cross-Linked Ion Gel as an Electrolyte for Thin Film, Printable Field Transistors

The chapter describes the development of ink-jet printable, self-assembled, and chemically cross-linked (CC) ion gels. These ion gels were synthesized by a straightforward synthesis process and designed to be ink-jet printable, thereby solving the drawbacks of a typical CC ion gel. It has a noticeable ionic conductivity of ~5 mS cm^{-1} and can drive a high effective capacitance of 5.4 μF cm^{-1} at 1 Hz. Moreover, it applies to the electrolyte-gated transistors (EGT) as a gate insulator and exhibits remarkable gating performance, on/off current ratios up to 1.3×10^{6} and a subthreshold swing of 80.62 mV dec^{-1}. This chapter covers the material design of the ion gels, the invention of ink-jet printable ion gel ink, the analysis of the polymer structures as well as their frequency-dependent behaviors, and gating performance in the electrolyte-gated transistors (EGT) in detail.

4.1. Ink-Jet Printable, Self-Assembled and Chemically Cross-Linked Ion Gel

Historically, physically cross-linked (PC) ion gels have been mainly developed as gate insulators for electrolyte-gated transistors (EGTs). Especially, ABA triblock ion gels, described in Chapter 2, have been considered as cutting-edge gate insulators and have been used for EGTs owing to their high ionic conductivity, high capacitance, printability, and thermal reversibility of gel structures. On the other hand, chemically cross-linked (CC) ion gels could not be used for printing processes due to their irreversible gelation and the resulting obstruction of the printing head nozzles. Therefore, CC ion gels could not be used as printed gate insulators for EGTs as well. However, their advantageous properties for application in EGTs, makes them desirable candidates for printed gate insulators. The covalently bonded, chemically cross-linked structures of CC ion gels reveal a much stronger physical

strength compared to physically cross-linked structures formed by polymeric entanglement or micellization. This results in the improved physical and thermal stabilities of the CC ion gels compared to other state-of-the-art polymer electrolytes which have physical cross-linked structures. This improved physical stability makes the final structure less sensitive against bending forces and therefore improves the durability of the printed device. For this reason, many researchers have tried to develop techniques to print CC ion gels and to overcome the drawback of the difficult printing procedure.[74,75] One workaround to achieve printed CC ion gel structures is a subsequent treatment of PC ion gel structures with UV light or annealing processes. These treatments can sometimes induce chemical reactions, leading to the formation of covalent bonds. As an example for this procedure, PC ion gels can first be printed on electric circuits and later UV irradiation or annealing processes are carried out to induce the mentioned chemical reactions in PC ion gels to create covalent-bonds.[74,75] However, this synthesis process is complex and it is difficult to precisely apply temperature or UV light to only these areas, where the reaction should happen, to prevent unwanted side reactions of other circuit components. Thus, the new ion gel presented in this thesis enables CC ion gel to be ink-jet printable with a straightforward synthesis method without any subsequent processes.

The self-assembled, CC ion gel is specially designed for the ink-jet printing process and the straightforward synthesis avoiding complicated post-procedures such as annealing [74], UV-curing[76,105], or polymerization.[65,78,79] This new ion gel is synthesized through a self-assembled gelation using poly(vinyl alcohol) (PVA) and poly(ethylene-*alt*-maleic anhydride) (PEMA), forming the rigid CC structures. This self-assembled gelation is spontaneous and quickly occurs in a viscous solution even at room temperature. For this reason, the self-assembled gelation has to be properly inhibited for ink-jet printing because printing is impossible if the gelation has already taken place.

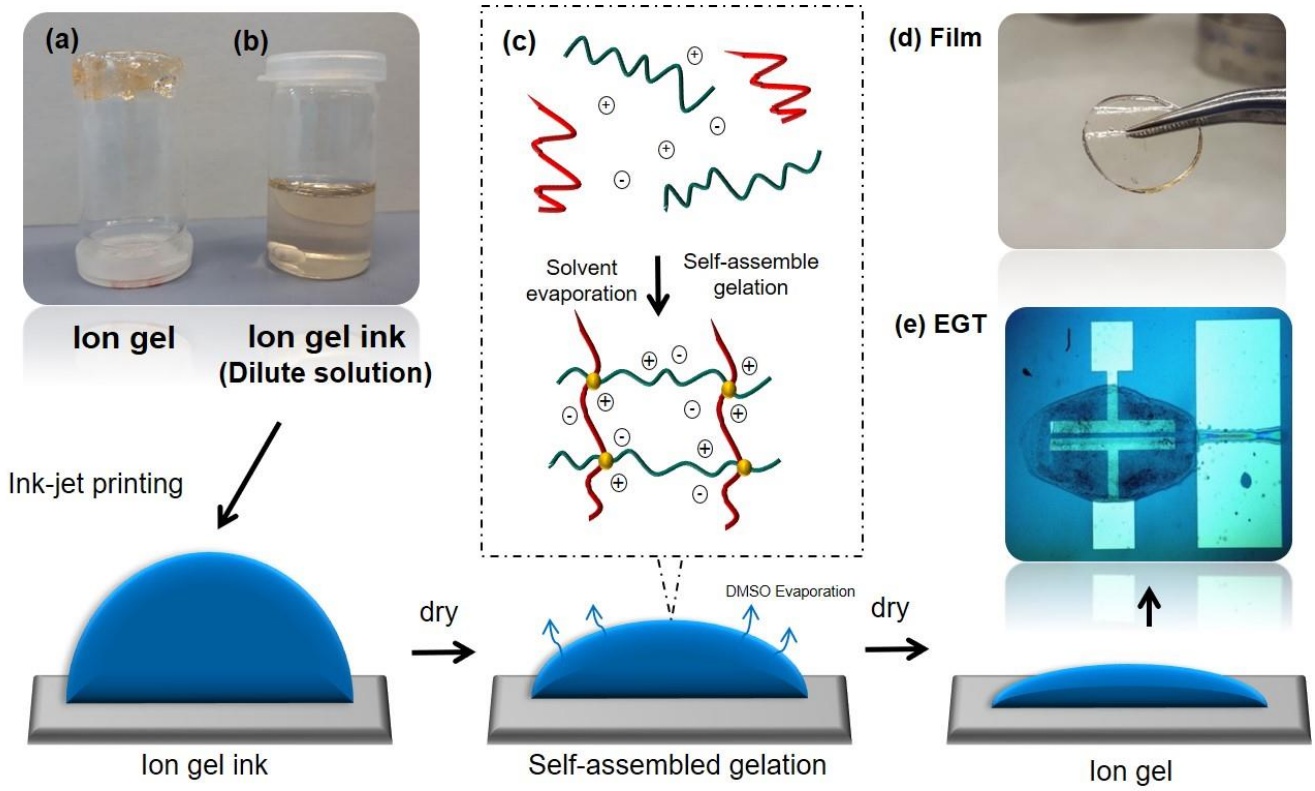

Figure 4-1. Schematic illustration of ink preparation and synthesis of PVA/PEMA ion gel; (a) ion gel, and (b) ink-jet printable ion gel ink (dilute solution), (c) illustration of self-assembled gelation of PVA, PEMA, and [EMIM][OTf] during DMSO evaporation, (d) PVA/PEMA ion gel film, and (e) top-gated, ion gel-gated thin-film transistor.

The method to inhibit the self-assembled gelation is to control the amount of DMSO in the ion gel ink. In solution, the hydroxyl groups of PVA and the cyclic anhydride groups of PEMA can generate sufficient mutual interactions resulting in a ring-opening esterification. This reaction is thermodynamically favorable and spontaneous even at room temperature, if the ratio between PVA and PEMA is optimized. The oxygen atoms of the hydroxyl groups initiate a ring-opening esterification by a nucleophilic attack to the 4-carbon atoms of the cyclic anhydride. This reaction leads to the chemical crosslinking mechanism of the CC polymer and results in a solidified polymer due to excessive polymerization. The CC polymer in this state is not printable anymore.

Therefore, in order to allow printing of the CC polymer, the viscosity of the precursor solution has to be minimized, which means that the polymerization reaction has to be inhibited. To do that, the interactions between the precursors must be weakened to inhibit the ring-opening esterification. Our approach is to add an excessive amount of DMSO into the ion gel ink to weaken their mutual interactions. In a dilute solution, the excessive solvent separates between PVA and PEMA, and makes them lose the mutual interactions required for the gelation [106]. The self-assembled gelation is effectively inhibited through the optimization of the solvent ratio in the ion gel ink. Thus, the ion

gel ink becomes ink-jet printable (Figure 4-1 (b)). After ink-jet printing, the solvent-swollen macromolecular coils release the solvent during the solvent evaporation, and the self-assembled gelation starts to form the CC polymeric structures. This reaction is fast and spontaneous at a specific concentration of PVA and PEMA in solution and does not require any additional processing. By controlling the self-assembled gelation, CC PVA/PEMA ion gel could be successfully applied to ink-jet printing for the fabrication of EGTs, as shown in Figure 4-1.

4.2. The Self-Assembled Gelation by the Ratio of PVA and PEMA

The self-assembled gelation of PVA and PEMA is dependent on their ratios, therefore, it is important to find out the optimized ratios and to control them during the reaction. Ideally, the number of each hydroxyl and cyclic anhydride groups participating in the reaction should be equal, so that all reactants form the chemically cross-linked structure, without leaving unreacted species behind. However, the realistic optimized ratio deviates from 1:1, because there are many other factors, which influence the esterification rate between hydroxyl and cyclic anhydride groups. For example, esterification between hydroxyl and cyclic anhydride groups is affected by the steric hindrance of hydrocarbon chains.[107] If hydrocarbon chains surround the hydroxyl groups, which should initiate the esterification by a nucleophilic attack, the steric hindrance decreases the esterification rate.[107] Furthermore, it is crucial that the esterification of hydroxyl and cyclic anhydride groups is facilitated when hydroxyl groups are abundant.[107] Therefore, rather than just making the number of hydroxyl and cyclic anhydride groups equal by calculation of the number of functional groups, the ratio optimization by the experimental method should be carried out to find out which ratio can induce proper esterification speeds for the printing process. The ratio of PVA and PEMA was optimized experimentally by blending different amounts of PVA and PEMA and by determining the polymerization rate. Figure 4-2(a) illustrates the results of the self-assembled gelation at room temperature, depending on the weight ratios of PVA and PEMA. The polymer solutions in the weight

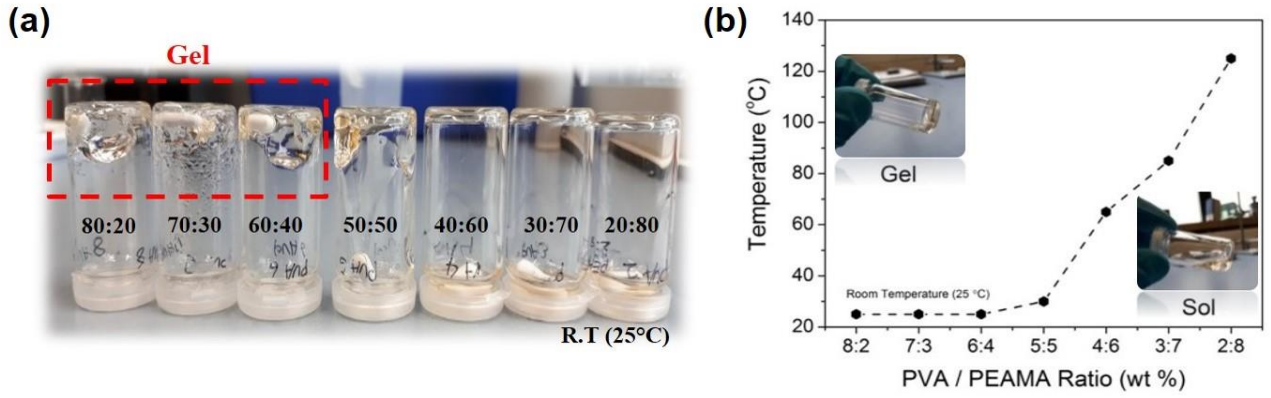

Figure 4-2. Sol-gel transition of PVA-PMEA solution by self-assembled gelation depending on (a) the ratio and (b) temperature. The samples shown in (a) were prepared at room temperature.

ratios of 80:20 to 60:40 wt% (PVA:PEMA) were gelated at room temperature. This can be easily pinpointed when the polymeric gel traps the magnetic stirring bar, whereas the magnetic stirring bar falls off when the polymeric gel structures are insufficiently formed due to a lack of chemical cross-linker, as shown in Figure 4-2. The most promising results were achieved with a weight ratio between 80:20 and 60:40 wt%.[107] Table 4-1 lists the molar proportions (mol %) of hydroxyl and cyclic anhydride groups of samples in Figure 4-2. Figure 4-2 and Table 4-1 indicate that esterification occurs more efficiently when the molar proportions of cyclic anhydride group are less than 20 mol %. When the mol % of cyclic anhydride is higher than 20%, esterification does not properly start, and an increased temperature is necessary. This tendency increases and can be observed in samples with higher cyclic anhydride content. An increased temperature increases the thermal motion of polymer structures, reducing steric hindrance, and therefore leads to higher reaction speeds.

These results unveil that using an equimolar ratio is not the most effective strategy for gelation. Considering these influence parameters and to make gelation possible at room temperature, the ratio of PVA and PEMA was established at 70:30 wt% in this thesis.

Table 4-1. Molar proportion of hydroxyl group of PVA (M_w= 100,000) and cyclic anhydride group of PEMA, corresponding to samples in Figure 4-2. The molecular weight (M_w) of PEMA is calculated to 250,000 as an average M_w because commercial PEMA has a broad molecular weight distribution (M_w: 100,000-500,000, Sigma Aldrich).

Weight percent (wt%) (PVA : PEMA) in Figure 4-2	80:20	70:30	60:40	50:50	40:60	30:70	20:80
Hydroxyl group (mol %)	91	85	79	71	63	52	38
Cyclic Anhydride group (mol %)	9	15	21	29	38	48	62

4.3. Fourier-Transform Infrared (FTIR) Spectroscopy

The CC structures created by the self-assembled gelation could be identified by Fourier transform infrared (FTIR) spectroscopy. With the results of FTIR spectroscopy, it has been determined that PVA/PEMA ion gel has a CC structure by ring-opening esterification. In Figure 4-3(a), two characteristic peaks at 1854 cm^{-1} and 1782 cm^{-1} are observed in the spectra of PEMA. These peaks correspond to the symmetric and asymmetric stretching bands of C=O within the cyclic anhydride.[108–111] With these two peaks, the CC structure created by the ring-opening esterification of the hydroxyl group (OH-) of PVA and cyclic anhydride of PEMA can be tracked. In the synthesis process of the CC ion gel, the swollen macromolecular coils of PVA and PEMA release the trapped solvent and become reactive during the solvent evaporation. Then, carboxylic acid and ester are structured by the ring-opening esterification (Figure 4-3(e)). Due to this reaction, symmetric and asymmetric stretching bands (1854 cm^{-1} and 1782 cm^{-1}) of two C=O carbonyl structures in cyclic anhydride disappeared. The overlapped bands of C=O carbonyl stretching vibrations of carboxylic acid (1717 cm^{-1}) and ester (1720 cm^{-1}) are shown in Figure 4-3(c) and Figure 4-3(d) [111–113].

The broad band (1700-1720 cm^{-1}) in Figure 4-3(a) corresponds to the C=O stretching band of maleic acid hydrolyzed from maleic anhydride during the film-making process [103]. The small band around 1720 cm^{-1} in the spectra of PVA (Figure 4-3(b)) is attributed to the C=O band of poly(vinyl

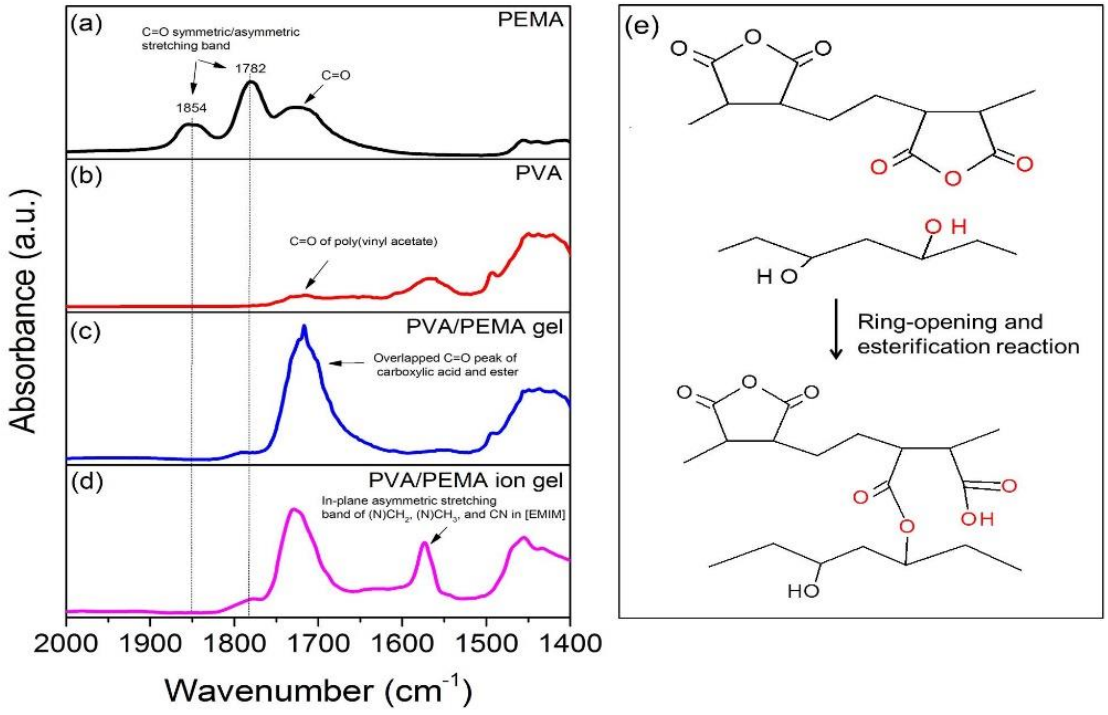

Figure 4-3. FT-IR absorbance spectra; (a) PEMA film, (b) PVA film, (c) PVA/PEMA polymeric gel film, (d) PVA/PEMA ion gel film. DMSO is fully evaporated. (e) Polymer structure of PVA, PEMA, and PVA/PEMA polymeric gel.

acetate) (PVa), which is the unhydrolyzed residue during the PVA synthesis in the factory.[114] The same C=O band of PVa is also observed in the PVA pellet prepared by hydraulic pressure using commercial PVA powder and potassium bromide (KBr) (Figure 4-4). In Figure 4-3(d), the band at 1573 cm^{-1} corresponds to the in-plane stretching band of $(N)CH_2$, $(N)CH_3$, and CN of [EMIM] [115]. With these results, it is determined that the ring-opening esterification of PVA and PEMA creates the CC structure forming the polymeric gel.

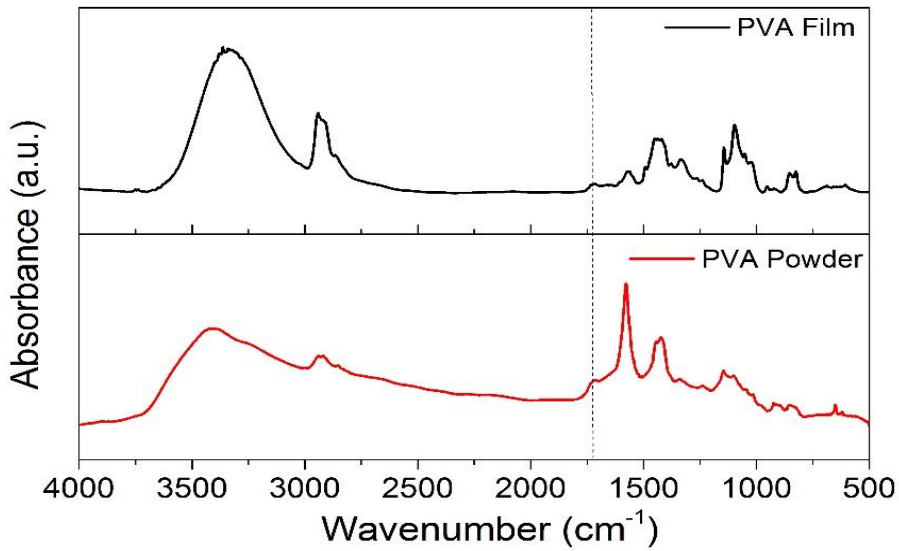

Figure 4-4. FT-IR absorbance spectrum of PVA film (black) and PVA pellet (red). PVA powder was pelletized with commercial PVA and KBr by hydraulic pressure.

4.4. Scanning Electron Microscopy (SEM)

A scanning electron microscope (SEM) is a powerful tool to investigate the surface morphology of the polymer film. The surface morphologies of PVA, PEMA, and PVA/PEMA polymeric gel films were investigated at the micron scale by SEM (Figure 4-5). For the measurement, the solvent absorbed in the polymeric matrix was entirely evaporated for vacuum condition.

The morphology of polymer films is affected by the types of solvent and the drying temperature and speed.[116,117] Specifically, the volatility of solvents influences the surface roughness of polymer films.[117] Highly volatile solvents, like tetrahydrofuran (THF), quickly evaporate and lead rough surface morphologies when polymer films are prepared by drying the solvent. On the other hand, solvents such as toluene and trichloroethylene lead to smooth surface morphologies due to their low volatility.[117] Likewise, since the increase of temperature can accelerate the evaporation of solvents, therefore, it is preferred to dry the solvents at low temperatures to make surface morphology smooth. Moreover, drying temperature and types of

solvent also affect the crystallinity of polymers due to the formation of lamellas. For these reasons, in this study, the films of PVA, PEMA, and PVA/PEMA gel were prepared using a low volatile solvent of DMSO at low drying temperature (50 ºC) to minimize the influence of solvent and temperature on their surface morphologies.

In SEM images, the PVA, PEMA, and PVA/PEMA polymeric gel films have different surface morphologies due to their structural natures and cross-linked structures. PVA and PEMA are not chemically cross-linked polymers, so they can partially crystallize by the formation of lamella structures by intermolecular interactions or can form smooth surface by dense stacking, depending on the film preparation condition. On the other hand, PVA/PEMA gels have a 3-dimensional polymeric network in which ionic liquids can permeate. Furthermore, their polymeric network prevents forming crystalline lamella structures, and it difficult to form smooth surfaces like PVA or PEMA due to their CC structures. The PVA film has small pores and thin thread-shaped structures on the edge of films (Figure 4-5(a)), and the PEMA film has large agglomerates and a relatively smooth surface (Figure 4-5(c)). The PVA/PEMA polymeric gel film has a very rough surface morphology and bundles of agglomerates on the edge of the film, stacking and creating large holes (Figure 4-5(e)). These large holes caused by the bundles of agglomerates create the solvent-permeable spaces inside the polymeric gel structure. Due to these solvent-permeable spaces, PVA/PEMA polymeric gel can absorb a large amount of the ionic liquid and swell. The SEM images show the drastic changes in the surface morphologies. It can be determined that the ring-opening esterification between PVA and PEMA creates the rough surface morphologies and the large solvent-permeable spaces inside the polymeric gel.

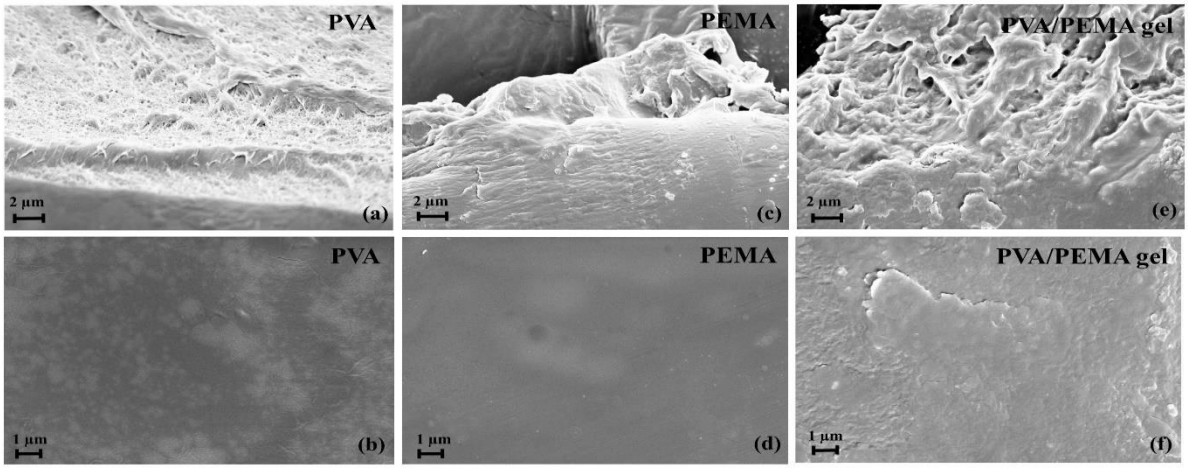

Figure 4-5. Scanning electron microscope (SEM) images of (a,b) PVA, (c,d) PEMA, and (e,f) PVA/PEMA gel films. (a),(c), and (e) are the film edge, and (b), (d), and (f) are the film surface. All the solvent is perfectly evaporated. A thin gold layer was sputtered on the surface of the film (10 nm).

4.5. Electrochemical Impedance Spectroscopy (EIS)

The frequency-dependent behavior of PVA/PEMA ion gel is analyzed by electrochemical impedance spectroscopy (EIS), probing the phenomena of dipole relaxation, ion migration, and formation of the EDL. The frequency range was swept in the range from 100 kHz to 1 Hz with a voltage amplitude of 10 mV. For the EIS measurement, the PVA/PEMA ion gel was prepared as a circular bulk film (diameter: 12 mm and thickness 1.1 mm) and assembled with stainless-steel electrodes in the Swagelok cell (Figure 4-6(a)).

In the Bode plot, the bulk resistance (R_{bulk}) and the formation of EDLs are identified (Figure 4-6(b)). In the high frequency range (>30 kHz), a plateau of the log (|Z|) plot displays the R_{bulk}. In the frequency range of R_{bulk}, the conducting ions are not able to migrate to the inner and outer Helmholtz planes (IHP and OHP) at the interface of ion gel/electrode due to insufficient time for ion migration [92]. Therefore, the resistance from ion migration is measured without the influence of electrode polarization by the EDLs. In the low frequency range (<3.7 kHz), where the phase angle is lower than −45°, the electrode polarization by the EDL formation increases log (|Z|) as the frequency decreases. The phase angle of −45° is the datum line, at which the resistive behavior of PVA/PEMA ion gel is transformed into capacitive behavior by the influence of the formation of the EDLs [65,94]. The phase angle is saturated between −70° and −75° below 400 Hz, and the deviation between the saturated phase angle and an ideal capacitive response of −90° results from non-ideal capacitive behaviors of PVA/PEMA ion gel [92].

In addition, the ionic conductivity (σ) of PVA/PEMA ion gel is calculated and plotted in Figure 4-6(c). The ionic conductivity is calculated with Equation 4.1.

$$\sigma = \frac{d}{AZ_{re}} \tag{4.1}$$

d is the thickness of PVA/PEMA ion gel film, A is the surface area, and Z_{re} is the real part of the impedance. The ionic conductivity of the R_{bulk} (>30 kHz) is measured to be ~5 mS cm^{-1}. As the frequency decreases below 3.7 kHz, the conducting ions can migrate to OHP and IHP to form the EDLs at the interface of the ion gel/electrode, and the ionic conductivity decreases due to the influence of the electrode polarization [118–120]. For this reason, the ionic conductivity linearly decreases due to the capacitive behavior of PVA/PEMA ion gel below 3.7 kHz.

In many studies, the effective capacitance (C_{eff}) is calculated with the EIS results using two equations [94,99,121]. In Figure 4-6(d), the calculated C_{eff} derived using two equations is plotted versus the frequency. Equation 4.2 below is generally used for the calculation of C_{eff}.

$$C_{eff} = \frac{-1}{2\pi f A Z_{im}} \tag{4.2}$$

A is the surface area of the electrode, f is the frequency, and Z_{im} is the imaginary part of the impedance. However, Equation 4.2 is only valid for the low frequencies and deviates in the high frequency range [99,122,123]. For this reason, as suggested in [99], the C_{eff} is calculated using Equation 4.3 for a more precise determination.

$$C_{eff} = \frac{-Z_{im}}{2\pi f A|Z|^2} \quad (4.3)$$

In Figure 4-6(d), the C_{eff} calculated by Equations 4.3 drops drastically in the high frequency range (> 3.7 kHz). This result is in accordance with the Bode plot (Figure 4-6(b)), in which the resistive response dominates in the high frequency range, and the conducting ions cannot form the EDL at the interface of the electrodes. Therefore, we consider that the C_{eff} derived using Equation 4.3 corresponds to the impedance results in the high frequency range of the Bode plot in a more precise manner. The $C_{eff,}$ according to Equation 4.3, is calculated to be 5.4 μF cm^{-2} at 1 Hz.

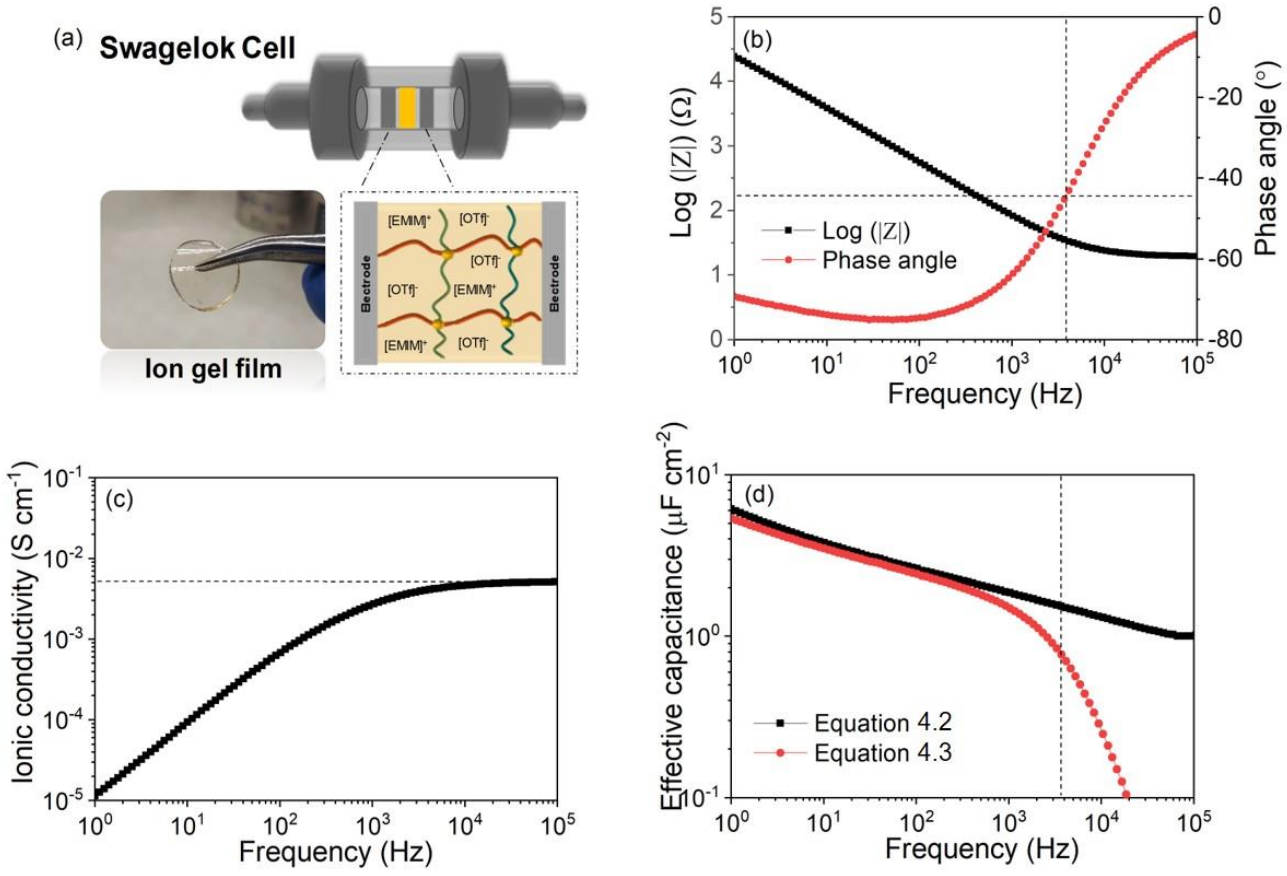

Figure 4-6. (a) Illustration of a Swagelok cell assembled with two electrodes and the ion gel film. (b) Bode plot, (c) ionic conductivity versus frequency plot, and (d) effective capacitance (C_{eff}) versus frequency plot of PVA/PEMA ion gel film. Ionic conductivity and capacitance were calculated based on impedance results. The samples were measured at room temperature (25 ºC). Film thickness and diameter are 1.1 mm and 12 mm, respectively.

Additionally, the PVA/PEMA ion gel was tested directly on the device by the EIS to identify whether the PVA/PEMA ion gel synthesized after ink-jet printing shows capacitive behavior like the bulk ion gel film. The dilute ion gel ink was printed and ion gel was synthesized by self-assembled gelation on in-plane ITO electrodes, which were lithographically patterned by an e-beam (Figure 4-7(d)). Compared to the frequency-dependent behavior of the bulk ion gel film, the entire plots of log (|Z|) and the phase angle in the Bode plot were shifted to the low-frequency range. This deviation comes from the scale, electrode materials, and geometry between Swagelok cell and the in-plain ITO electrode. The Bode plot in Figure 4-7(a) clearly shows the polarization mechanism of dipole relaxation (> 19 kHz), R_{bulk} (19 kHz > f > 105 Hz), and EDL formation (< 105 Hz) according to the applied frequency. The dipole relaxation of PVA/PEMA ion gel was observed in high frequency over 19 kHz. This dipole relaxation region could not be observed with the bulk ion gel film assembled with Swagelok cell because of the frequency limits (Figure 4-6(b)). As the frequency decreases, the R_{bulk} and the formation of EDLs are observed, similar to the bulk ion gel film. The C_{eff} is calculated to 5.77 μF cm^{-2} at 1 Hz. As mentioned above, these results illustrate that PVA/PEMA ion gel on a microscale also dipicts the typical polarization mechanism in relation to the applied frequency.

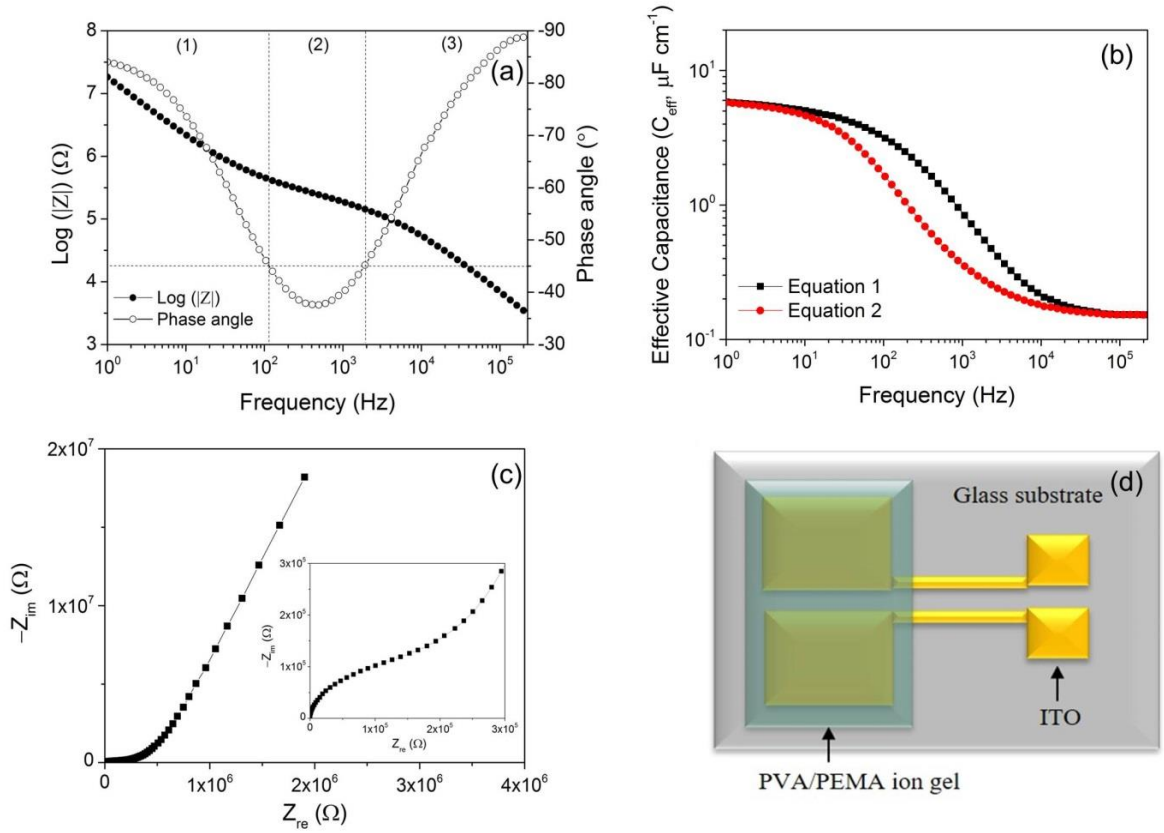

Figure 4-7. Impedance results of PVA/PEMA ion gel in the in-plain substrate; (a) Bode plot of log(|Z|) versus frequency, (b) Ceff versus frequency plot, (c) Nyquist plot, and (d) Schematic image of in-plain ITO electrodes patterned by e-beam laser. PVA/PEMA ion gel is printed on a patterned electrode (500×300 μm) by an ink-jet printer.

4.6. Electrolyte-Gated Transistors (EGTs)

Transistors are the basic unit blocks for every electronic circuit. The EGTs presented here are suitable transistor systems for printed high performance and low voltage applications such as smart sensors and wearable devices.[124] As reported in previous studies, the utilization of polymer electrolytes or ion gels enables low voltage operation of EGTs (below 2 V).[124,125] In this study, the PVA/PEMA CC ion gel can show improved key performance parameters when included in EGTs. Typical gel polymer electrolytes (GPEs) and ABA triblock ion gels, which are used as state-of-the-art electrolytes, form PC structures by polymeric entanglement and micelle formation, respectively. As explained, the physical strength of PC structures is weaker than the strength of covalent-bonded CC structures. Therefore, PVA/PEMA ion gels are expected to be more suitable for application in flexible devices, due to their improved elastic and physical properties compared to CSPE or other ABA triblock ion gels. Additionally, the ionic conductivity of the applied electrolyte plays a key role in transistor operation. High ionic conductivities lead to improved transistor performances and, therefore, can be seen as crucial parameters. While ABA triblock ion gels and GPEs show ionic conductivities of ~2 mS cm^{-1} and 10^{-7} to 10^{-3} S cm^{-1}, respectively, the developed CC ion gels can reveal strongly increased values.[53,65,72,75,126]. This is related to the high intrinsic ionic conductivity of [EMIM][OTf], measured to be ~8 mS cm^{-1}. The ionic conductivity is proportional to the content of IL in the gel polymer structure.[127] By maximizing the contents of [EMIM][OTf] in PVA/PEMA gel structures, their ionic conductivity could reach maximum values. Besides, the high ionic conductivity, PVA/PEMA ion gels can also improve the switching speed of EGTs. Cations and anions of ILs are only weakly interacting over Coulomb forces, leading to the high mobility of the species inside the electrolyte. Therefore, it is expected that PVA/PEMA ion gels can exhibit improved gating performance in EGTs compared to ABA triblock ion gels or GPEs.

The reasons for improved ionic conductivities compared to GPEs are as follows. In previous studies, the state-of-the-art printed EGTs include a composite solid polymer electrolyte (CSPE) consisting of poly(vinyl alcohol) (PVA), propylene carbonate, and lithium perchlorate ($LiClO_4$). The CSPE is GPE-type, which has a ternary composite system of PC backbone polymers, organic plasticizers, and conducting salts. Compared to ion gels, CSPE has a different ion-conducting system. In ion gels, cations and anions of ILs play the role of both, conducting ions and plasticizers, as they can permeate into cross-linked gel structures.

Moreover, CC structures (e.g., PVA/PEMA in the presented ion gel) or PC structures by the micelle of ABA triblock copolymers do show a reduced degree of crystallinity of backbone polymers. They form 3-dimensional polymeric networks, with structures that are not easy to change due to their interconnected chains. Thereby, they cannot easily be stacked to form crystalline lamellas that are created by the intermolecular interactions. In contrast to that, PVA is known to form crystalline lamella structures easily. PVA is a semi-crystalline polymer, and its polymer chains can densely stack

to form lamellas by intermolecular interaction. Therefore, using CC structures or PC structures by a micelle of ABA triblock copolymers is useful to reduce the degree of crystallinity and to form amorphous phases rather than using a semi-crystalline polymer like PVA.

During transistor operation, i.e., when an electric field is applied to open the semiconducting channel, cations and anions can conduct in these cross-linked gel structures without their movement being hampered by steric effects of crystalline polymer structures. However, in the CSPE, lithium ions (Li^+) and perchlorate ions (ClO_4^-) contribute to the ionic conductivity, and propylene carbonate helps to dissociate $LiClO_4$ and as plasticizer reduces the degree of crystallinity of PVA. Since PVA is a semi-crystalline polymer, it is crucial to implement plasticizers in order to enhance the ionic conductivity by reducing the crystallinity. As will be explained later in Section 4.7, although the CSPE has been used as a cutting-edge gate insulator for EGTs, it is expected that the implementation of propylene carbonate as a plasticizer can be further improved, because the CSPE still needs the assistance of water molecules to achieve high ionic conductivities in EGTs. Due to these differences in composition and ion-conduction, GPEs generally have lower ionic conductivities than ion gels. Therefore, in this study, the CSPE was replaced by the presented PVA/PEMA CC ion gel to improve the gating performance of EGTs.

N-type top-gated EGTs were fabricated to test the gating performance of the PVA/PEMA ion gel. Furthermore, it was investigated how the improved ionic conductivity contributes to the effective capacitances formed by EDLs and to the gating performances when used as the gate insulator. For the fabrication of EGTs, the precursor ink of indium oxide was printed on the indium tin oxide (ITO)-deposited glass substrates, which were lithographically patterned by an e-beam (channel width (W) and length (L): 600 μm and 20 μm, respectively). After the precursor ink was annealed at 400 °C for 2 hours, the ion gel ink was printed on the In_2O_3 channels. Within a few minutes, the DMSO in the printed ink droplet quickly evaporated, and the self-assembled gelation formed the ion gel on the In_2O_3 channels. After the gelation, the top-gate of poly(3,4-ethylene dioxythiophene)-poly(styrene sulfonate) (PEDOT:PSS) was printed on the ion gel [128]. Composite solid polymer electrolyte (CSPE) consisting of PVA, propylene carbonate (PC), and lithium perchlorate ($LiClO_4$) was also applied to the EGT as a gate insulator by the same fabrication processes, for comparison with the ion gel.

The EGTs using PVA/PEMA ion gel and CSPE (ion gel-gated FET and CSPE-gated FET) are characterized in Figure 4-8. For a few years, CSPE has been utilized and optimized as a standard gate insulator of the EGT [129–131]. However, PVA/PEMA ion gel exhibits an enhanced gating performance compared to the CSPE. Figure 4-8(a) shows drain current (I_d) and gate leakage current (I_g) versus gate voltage (V_g) plots of the ion gel-gated and CSPE-gated FETs. In the plots, the hysteresis of the PVA/PEMA ion gel is much narrower than that of the CSPE, indicating that the conducting ions in PVA/PEMA ion gel respond more quickly to the controlled V_g and form the EDLs

which open and close the semiconducting channels. The on/off current (I_{on}/I_{off}) ratios of the ion gel-gated and CSPE-gated FETs are calculated to 1.3×10^6 and 6.32×10^5, respectively.

The subthreshold swing (SS) is calculated using Equation 2.33. The SS of the PVA/PEMA ion gel is 80.62 mV dec^{-1}, which is close to the theoretical limit of 60 mV dec^{-1}. This SS value is much closer to theoretical limits than that of the CSPE, which is calculated to be 100.73 mV dec^{-1}. The results above show that the PVA/PEMA ion gel has better gating performance in the EGT than the CSPE. These results underline the improved output of the ion gel, which is connected to the increased ionic conductivity, as already explained. The SS values, as shown in Figure 4-8, depend on the ionic conductivity of gate insulators because the channel opening mechanism is related to ion migration and the formation of EDLs. When a gate voltage (V_g) is applied, an electric field between gate electrode and semiconductor is generated, and ions migrate to the interface of the semiconductor and gate electrode to form EDLs, which open n-type current channels in In_2O_3 semiconductors. For this reason, as the ionic conductivity increases, the formation of EDLs also becomes faster, resulting in high SS values. Moreover, the ion-conducting speed in electric fields, defined as ionic mobility (μ_{ion}), can be calculated with the ionic conductivity. They are correlated as described below in Equation 4.4.

$$\sigma = en\mu_{ion} \tag{4.4}$$

n , e, μ_{ion} are the ionic concentration, the charge of ions, and ionic mobility. The ionic conductivity is proportional to the ionic mobility. Therefore, it can be inferred that the difference in ion conductivities of the gate insulators shows different ion mobility in the applied electric field between the gate electrode and semiconductor. Since the PVA/PEMA ion gel and CSPE have different ionic conductivities, they have different ionic mobility resulting in different SS values. The low SS value of CSPE-gated EGTs is due to the low ionic conductivity of the CSPE. The CSPE in EGTs requires the assist of water molecules to transfer lithium ions in the polymer structure of PVA due to the lack of propylene carbonate used as a plasticizer.[125] This will be explained in more detail at the humidity stability test results in Section 4.7. Even though bulk CSPE indicates high ionic conductivities measured by EIS, the plasticizer propylene carbonate may evaporate during the printing procedure or during the drying process. This can lead to lower ionic conductivity values, as the lower SS values of CSPE-gated EGTs, compared to ion gel gated devices, indicate. An ionic liquid of [EMIM][OTf] is sufficiently trapped in PVA/PEMA gel structures, and due to the negligible volatility, it will not evaporate even after printing and polymer drying. Thereby, PVA/PEMA ion gel exhibits high SS values due to its negligible volatility, as well as its high ionic conductivity.

In Figure 4-8(b), output characteristic curves of the ion gel-gated FETs are plotted. The output characteristic curves display linear and saturation regions, depending on the source-drain voltage (V_d). The V_d makes the potential difference between the source and drain electrodes, and allows

the current to flow through the current channels present in semiconductors. In the linear region, the I_d proportionally increases with the V_d. However, the I_d becomes saturated when the amount of the I_d reaches the limit of the current channel. In the saturation region, the I_d is constant regardless of the V_d. On the other hand, V_g affects the I_d in the saturation region. As the higher V_g applies to PVE/PEMA ion gel, it can drive higher capacitances by EDLs, and can thereby open the larger current channels in the semiconductor. In the output characteristic curves, it is identified that the I_d increases as the V_g increases in the saturation region. These results verify that the PVA/PEMA ion gel effectively acts as a gate insulator of the EGTs.

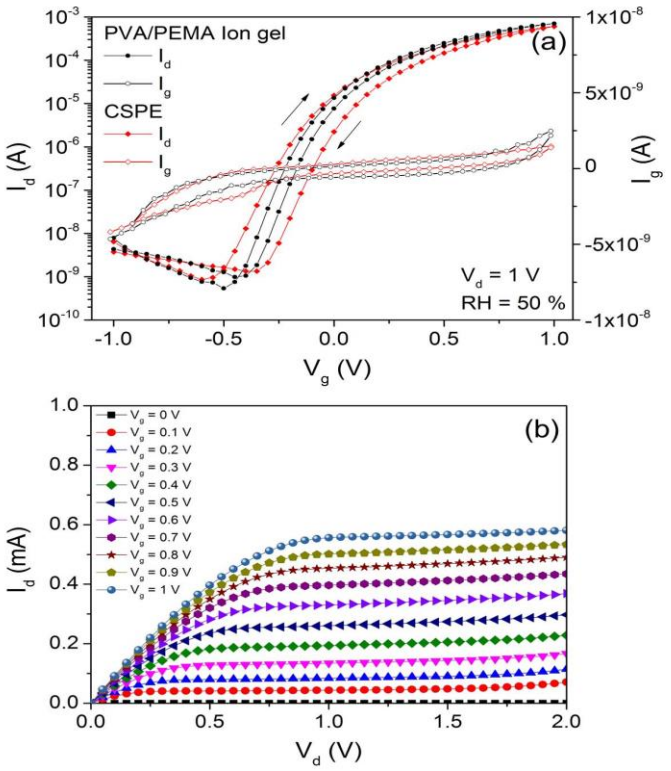

Figure 4-8. Electric characterization of top-gated EGTs; (a) gate-source voltage (V_g) versus drain-source current (I_d) and gate leakage current (I_g) plots of PVA/PEMA ion gel and CSPE at 50 % relative humidity (RH) and 1 V drain-source voltage (V_d), (b) V_d versus I_d plot of PVA/PEMA ion gel at 50 % RH. Channel width and length are 600 μm and 20 μm, respectively.

In addition, in Figure 4-9, the V_g versus I_d plots show the results of a durability test of the PVA/PEMA ion gel in the EGT. To identify the difference in gating performances by aging, the EGT was stored for 10 weeks in room conditions after the first measurement. In the transfer curves, it is noteworthy that the EGT exhibited stable gating performances even after 10 weeks. Upon comparison of the aged EGT with the new one, the differences between their on/off currents are almost negligible, and they show negligible hysteresis in their transfer curves. The results indicate that the PVA/PEMA ion gel is stable and did not decompose even after 10 weeks in room conditions. Furthermore, it results from the negligible volatility of [EMIM][OTf], which could exist in PVA/PEMA gel structures and contribute to the gating performance after the aging. Therefore, this result verifies

that the EGT using the PVA/PEMA ion gel can be used in room conditions without degradation problems.

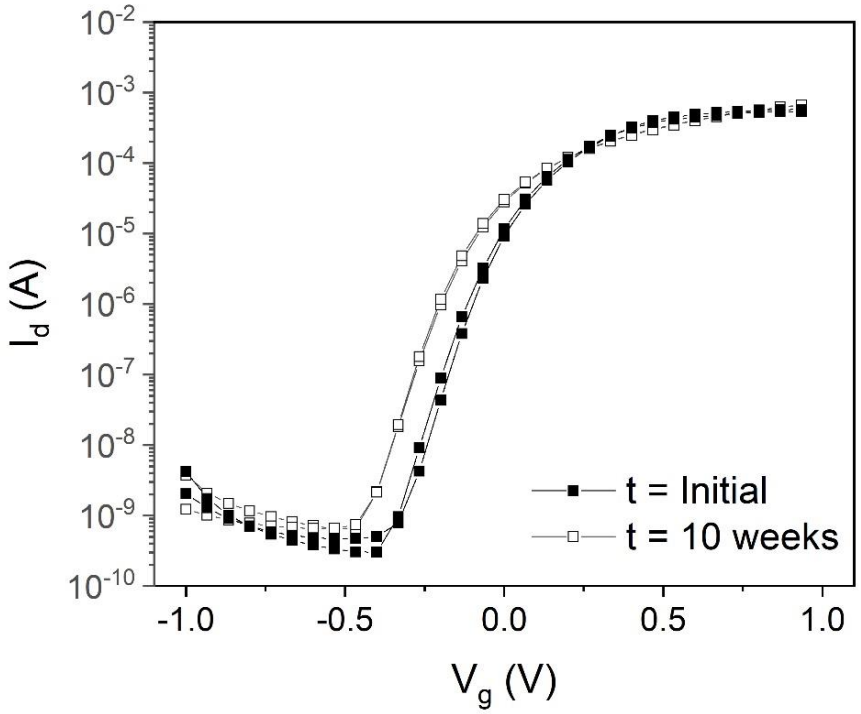

Figure 4-9. Gate-source voltage (V_g) versus drain-source current (I_d) plot for durability test of ion gel-gated EGTs. Drain voltage (V_d) is 1 V. RH is 50 %. The sample is aged for 10 weeks in room condition.

4.7. Stability Under Humidity

The stability of the gate insulator against humidity is important for the practical operation of the EGT in room conditions. However, in a previous study, Marques et al. reported that the CSPE in EGTs drastically loses its gating performance at low relative humidity (RH) (≤20 % RH) [125]. Ionic conductivity of the CSPE is drastically dropped by the insufficient amount of plasticizers, and the ion-transferring channels are disconnected in the PVA matrix at low RH conditions [125]. For this reason, the instability of the CSPE at low RH levels is considered a critical drawback because discrepancies in the weather can limit the operation of CSPE-gated FETs. The PVA/PEMA ion gel, however, solves this problem. In Figure 4-10(b), I_d and $Id^{1/2}$ versus V_g plots of CSPE-gated FETs show a wide hysteresis and a lower on-current value. The CSPE is not able to properly open and close the current channels in In_2O_3 semiconductors by applied V_g at 20 % RH. However, at above a 40 % RH, water molecules can permeate into the CSPE and assist the plasticizer of propylene carbonate in making ion-transferring channels. Therefore, appropriate humidity levels are necessary for the operation of CSPE-gated FETs. On the other hand, ion gel-gated FETs show very stable transfer

curves at all RH levels from 20 % to 90 %. Remarkably, the ion gel-gated FETs exhibit stable transfer curves at 20 % RH (Figure 4-12). These features are the results of the negligible volatility of [EMIM][OTf]. The negligible volatility is an intrinsic property of ILs. Weak Coulomb interaction between cations and anions allows reducing their melting points even below room temperature, but their interaction strength is not too weak to be vaporized. Therefore, due to the negligible vapor pressure and volatility of ILs, the [EMIM][OTf] stays as a liquid in the inks during the solvent-drying process. Therefore, [EMIM][OTf] can be captured in the PVA/PEMA gel structures. In addition, the CC structures of PVA/PEMA ion gels allow capturing a large amount of [EMIM][OTf], resulting in the synthesis of a highly conductive ionic gate insulator. The ionic conductivity of ion gels is proportional to the ratio of ILs. The ionic conductivity of ion gels increases as the content of ILs in the gel structures increases as well.[127] Since PVA/PEMA gel structures have chemical cross-linkers and a polymeric network, they can absorb a large amount of ILs by swelling. Moreover, their polymeric network by chemical cross-linker can prevent forming crystalline lamella structures that hinder ion conduction. In contrast, semi-crystalline, linear backbone polymers, e.g., PVA and PVDF, crystallize by forming lamella structures, depending on their composition and crystalline nature of the respective backbone polymers. Since weakly bound by physically cross-linked polymeric entanglement, their macromolecular chains can be more easily stacked to form lamellas with their mutual intermolecular interaction. By the optimization of the ink recipe, the [EMIM][OTf] is fully contained in the PVA/PEMA gel structures. Thus, it effectively contributes to controlling the current channels of the ion gel-gated FET at low RH levels regardless of the assistance of water molecules. The V_{th} and SS values of the ion gel-gated FETs are secure in the RH levels from 30 % to 60 % (Table 4-2), while those of CSPE-gated FETs increase by RH levels [125]. The V_{th} and SS values of the ion gel-gated FETs slightly changed over high RH levels (≥ 70 %) because of the hygroscopicity of PEDOT:PSS. Nevertheless, ion gel-gated FETs show stable gating performances at all R.H. levels. Also, Figure 4-11 shows gate leakage currents of the ion gel-gated FETs. The gate leakage currents are stable in the RH levels from 20 % to 70 %. However, over 70 % RH, the hygroscopicity of PEDOT:PSS absorbing water molecules influences the increase of the gate leakage currents. Furthermore, this influence becomes noticeable at 90 % RH. However, these values of the gate leakage currents are low and negligible in the performance of the ion gel-gated FETs. As aforementioned, it is clear that the PVA/PEMA ion gel solves the drawbacks of the CSPE and has better gating performance operated in all RH levels.

Table 4-2. Electrical parameters of PVA/PEMA ion gel-gated transistors at different values of the relative humidity (RH)

Relative Humidity [%]	Off current [A]	On current [A]	On/off current ratio [10^5]	Subthreshold swing [mV dec^{-1}]	Threshold voltage [V]
20	5.01×10^{-10}	6.86×10^{-4}	13.7	82.71	−0.241
30	4.56×10^{-10}	6.97×10^{-4}	15.3	80.71	−0.149
40	5.01×10^{-10}	6.15×10^{-4}	12.3	78.59	−0.161
50	5.37×10^{-10}	7.04×10^{-4}	13.1	80.62	−0.138
60	6.55×10^{-10}	5.89×10^{-4}	8.99	80.73	−0.154
70	1.44×10^{-9}	7.67×10^{-4}	5.31	85.94	−0.186
80	2.07×10^{-9}	7.76×10^{-4}	3.75	84.30	−0.217
90	2.30×10^{-9}	8.21×10^{-4}	3.58	86.01	−0.24

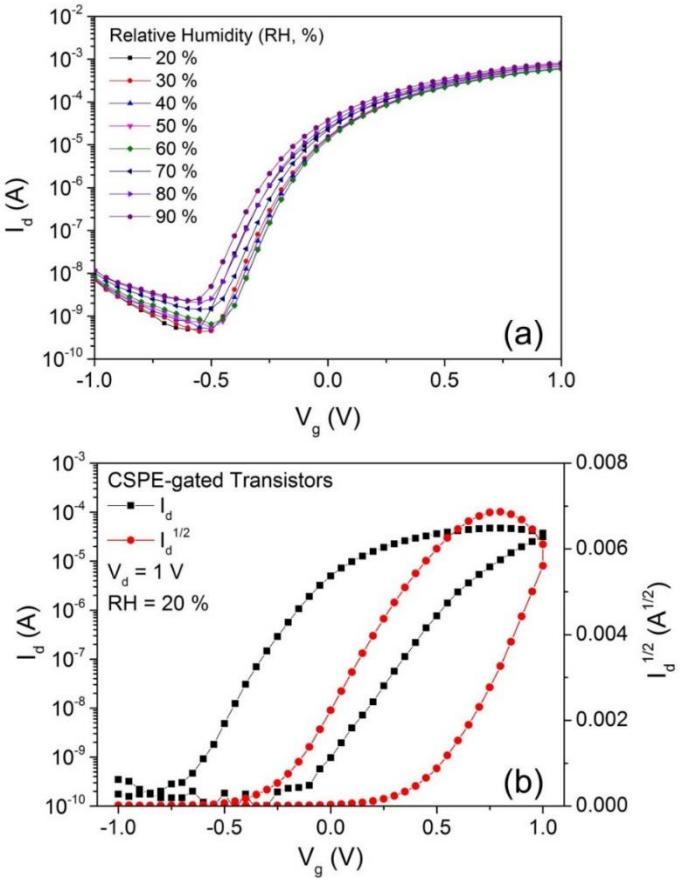

Figure 4-10. (a) Gate-source voltage (V_g) versus drain-source current (I_d) plot of PVA/PEMA ion gel gated FETs at 1 V_d at different relative humidities (RH, %) from 20 % to 90 %. (b) V_g versus I_d and $I_d^{1/2}$ plots of CSPE-gated FETs at 1 V_d and 20 % RH.

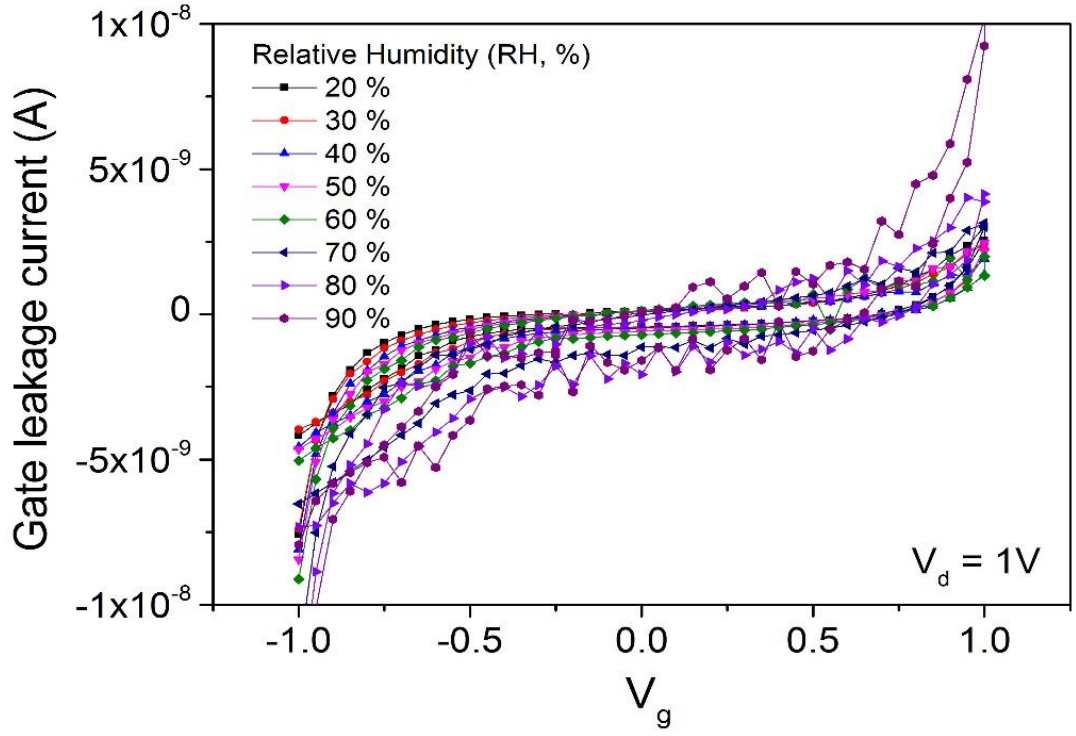

Figure 4-11. V_g versus gate leakage current (I_g) plots of PVA/PEMA ion gel-gated FETs at 1 V_d and different RH from

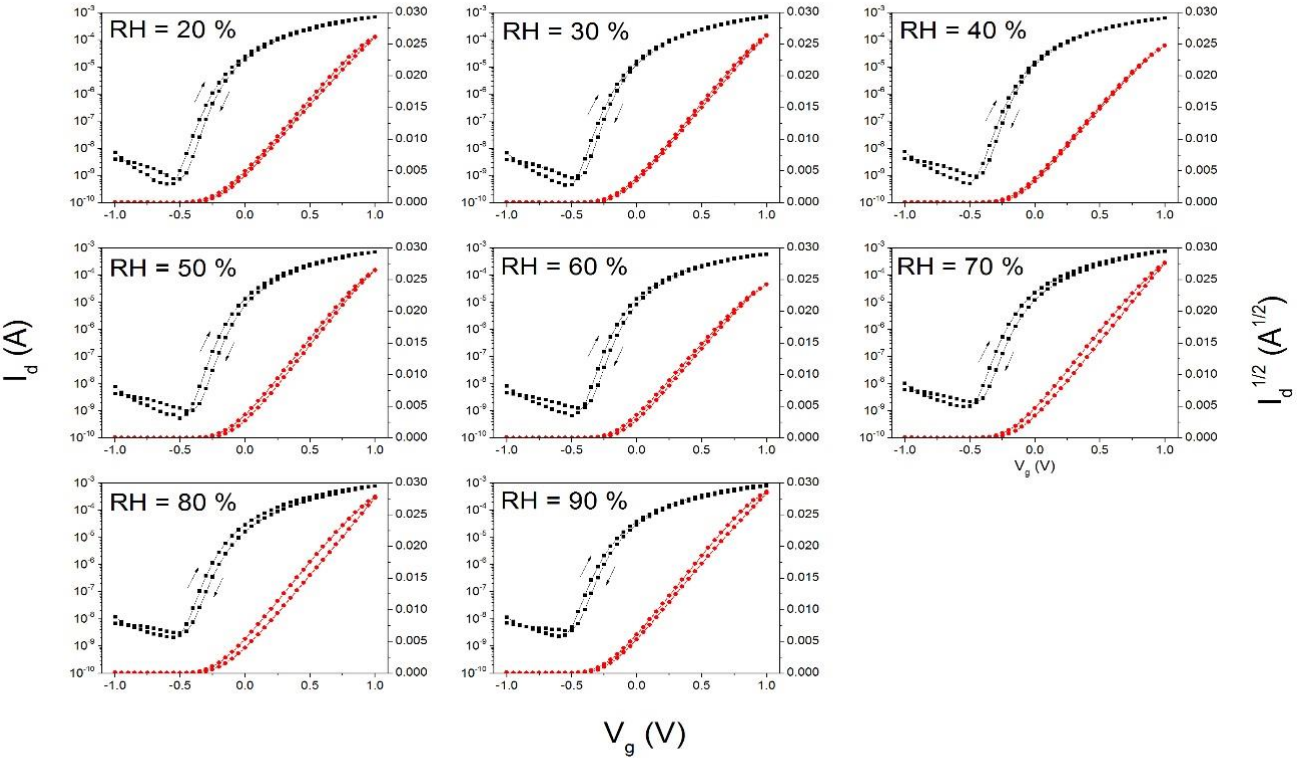

Figure 4-12. V_g versus I_d and $I_d^{1/2}$ plots of PVA/PEMA ion gel-gated FETs at 1 V_d and different RH from 20 % to 90 %.

4.8. Summary

In this chapter, a new method to synthesize a chemically cross-linked (CC) ion gel for EGTs is presented. The developed CC ion gel is a new material different from ion gels reported in other papers. Until now, physically cross-linked (PC) ion gels have mainly been utilized in printed electronics, whereas CC ion gels have not been used due to the difficulty of the printing process. However, the developed PVA/PEMA ion gel solves the problem and successfully applies this technique to ink-jet printing. Additionally, the synthesis process is designed to be straightforward so that anyone can easily follow the synthesis. In particular, the dilute ink of the PVA/PEMA ion gel is invented for ink-jet printing. By controlling the ratio of DMSO, the self-assembled gelation of PVA and PEMA is properly inhibited in dilute ink, and the PVA/PEMA ion gel is successfully applied to EGTs as a gate insulator using an ink-jet printer. The PVA/PEMA ion gel has a remarkable ionic conductivity of ~5 mS cm^{-2} and an effective capacitance of 5.4 μF cm^{-1} at 1 Hz. Moreover, it shows outstanding gating performances such as a high I_{on}/I_{off} ratio, narrow hysteresis, and appropriate SS values in n-type EGTs as a gate insulator.

In the aspect of developing EGTs for commercialization, the PVA/PEMA ion gel gating approach contributes to the development of printed EGTs, so that they can be used in ambient conditions. The PVA/PEMA ion gel solves a critical drawback of the CSPE, where ionic conductivity is lost at low humidity levels (~ 20%). The instability of gating performances at low humidity can limit the practical use of EGTs in dry climates. However, the PVA/PEMA ion gels solve this problem and make printed EGTs stable in a broad humidity window. The ion gel-gated FETs exhibit stable gating performances in all R.H. levels (20 % to 90%), indicating that they can be used in ambient conditions without the negative influence on gating performance by humidity. Moreover, through the durability test, it is observed that the ion gel-gated FETs are stable for approximately 10 weeks in ambient conditions.

This unique method to synthesize the CC ion gel, which has superb properties of high ionic conductivity, humidity stability, and durability in room conditions, enables new insights for developing CC ion gels to the field of printed electronics.

Chapter 5

5. Adhesive Ion Gel as Gate Insulator of Electrolyte-Gated Transistors

This chapter introduces a chemically cross-linked, adhesive ion gel designed for the facile fabrication of gate insulators for electrolyte-gated transistors (EGT). Fabrication techniques of the EGT have existed for a long time, and especially the printing techniques such as ink-jet printing, roll-to-roll printing, or aerosol-jet printing, have been widely used for the fabrication of EGTs. Moreover, as the printing techniques have been developed, the inks for electronic materials have also been optimized regarding viscosity, drying or other rheologic properties. For instance, the inks of ABA triblock ion gels were prepared and printed by the aerosol-jet printer for the fabrication of EGTs [65,132]. Marques et al. also reported the fabrication of the n-type In_2O_3-based EGTs through ink-jet printing of composite solid polymer electrolyte (CSPE) and indium oxide precursor [125]. Besides the printing techniques, other fabrication methods were investigated as well. For example, Lee et al. reported a rubbery ion gel that can be easily cut by hand and laminated on electric circuits of the EGT [133]. The efforts to diversify these fabrication techniques have multiplied in recent years.

Here, a new type of ion gel is reported. This ion gel is developed in an effort to diversify the fabrication method of the gate insulator of the EGT. It has an adhesive property that can easily adhere to various substrates, electrodes, and semiconductors. This adhesive property gives convenience to the fabrication of gate insulators of EGTs. In general, gate insulators are fabricated through continuous processes of ink-printing and solvent-drying. However, the film attachment of ion gels, using the adhesive property, is a one-step process that can fabricate gate insulators faster by excluding the solvent-drying process. Furthermore, adhesive ion gels (AIGs) can adhere to various materials such as plastics, metals, and fabrics; thereby, it is compatible with various electrode or semiconductor materials for electronic devices, e.g., organic field-effect transistor (OFET). Moreover, AIG films are suitable for EGTs, which have multi-layered structures, because film-attachment of AIG

film can prevent organic components from swelling or penetration by solvents during the solvent-drying process. Besides, since AIG films are elastic and free-standing due to CC gel structure, they are suitable for utilization in flexible devices. This AIG film is prepared by an uncomplicated synthesis method to avoid complex processes like polymerization or UV-curing. AIG can be cut by hand and laminated onto electric circuits with adhesive and flexible properties. AIG has remarkable ionic conductivity, and also exhibits remarkable gating performances in the EGT. Moreover, it can be reused several times without the loss of gating performance.

In this chapter, the synthesis method, the adhesive property, analyses of the molecular structures, frequency-dependent behaviors, and the gating performances of the AIG in the EGT are discussed in detail. Furthermore, gating performances of the EGTs fabricated by film-attachment and ink drop-casting are compared.

5.1. The Synthesis of Adhesive Ion Gel (AIG)

AIG is synthesized by a straightforward method using poly(vinyl alcohol) (PVA), poly(methyl vinyl ether-*alt*-maleic anhydride) (PMVE-MA), dimethyl sulfoxide (DMSO) and 1-ethyl-3-methylimidazolium trifluoromethanesulfonate ([EMIM][OTf]). PVA is a backbone polymer, and PMVE-MA is a chemical cross-linker. [EMIM][OTf] and DMSO are the conducting ions and solvent, respectively. The synthesis process and sample preparation are straightforward, as shown in Figure 5-1. For the synthesis, two polymer solutions, in which ingredients of polymers and ionic liquid are dissolved in DMSO, are prepared. Solution (1) consists of PVA and DMSO, and solution (2) consists

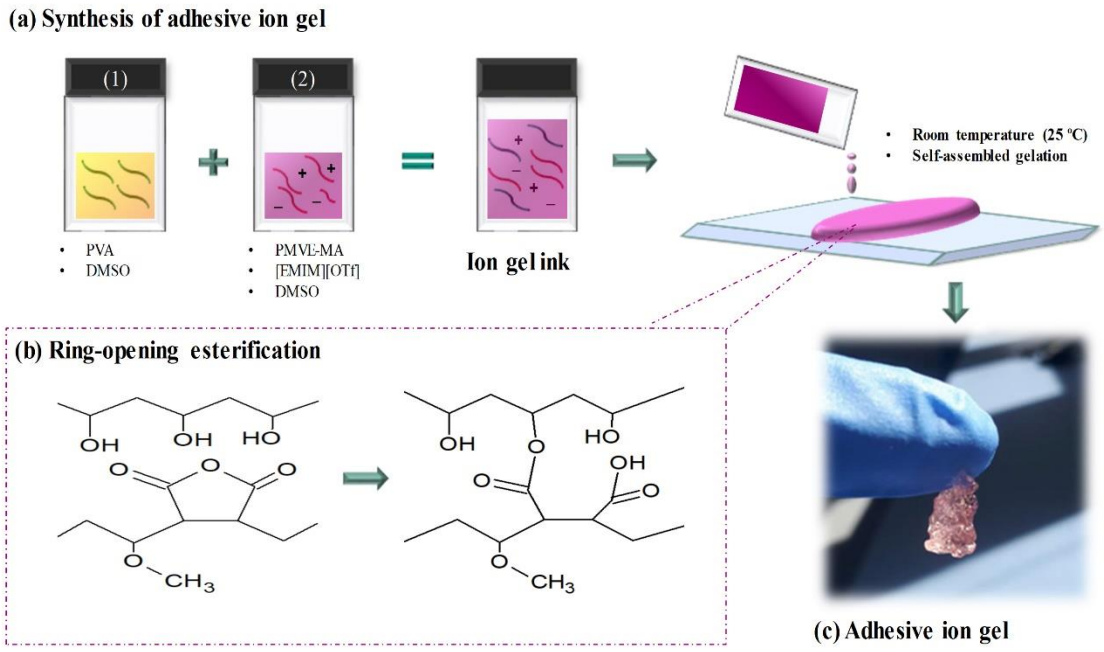

Figure 5-1. Schematic illustration of the adhesive ion gel; (a) the ink preparation for synthesis, (b) the ring-opening esterification, and (c) the adhesive ion gel

of PMVE-MA, [EMIM][OTf], and DMSO. When both solutions are blended, the ring-opening esterification between the hydroxyl group of PVA and cyclic anhydride of PVME-MA occurs, resulting in a chemically cross-linked (CC) gel structure [134]. This reaction is spontaneous and self-assembled. Thereby, the synthesis process does not need subsequent procedures. The blend of solutions should occur in a few minutes to prevent the self-assembled gelation before pouring on the glass substrate. The blended solution on the glass substrate aged overnight. After the aging, the AIG film is prepared.

5.2. The Adhesive Properties of AIG

The adhesive properties of the AIG mainly come from the functional groups of PMVE-MA. PMVE-MA has been studied as a bioadhesive [135–137] and is used in the fields of pharmaceuticals, biomedicals, and drug delivery systems [138,139]. Cyclic anhydride of PMVE-MA is hydrolytically cleaved to the maleic acid, which can make a hydrogen bonding with the mucosa, i.e., membranes covering the surface of internal organs [139,140]. The adhesion of maleic acid through hydrogen bonding can be formed on diverse substrates, not only for biomolecules. For instance, maleic acid cleaved from maleic anhydride can adhere to aluminum oxide (Al_2O_3), and carboxylate or carbonyl groups of maleic acid can form bonds to the aluminum cation by chelate or monodentate bonds [103]. Therefore, the hydrogen bonding formed through the cleavage of maleic anhydride, resulting in a carboxylic acid, contributes to the adhesion of the AIG. Methyl vinyl ether (MVE) also contributes to the adhesion. MVE is known as a pressure-sensitive adhesive [141] and is already used in academia and industry. Thus, the adhesive property of AIG results from MVE and maleic acid

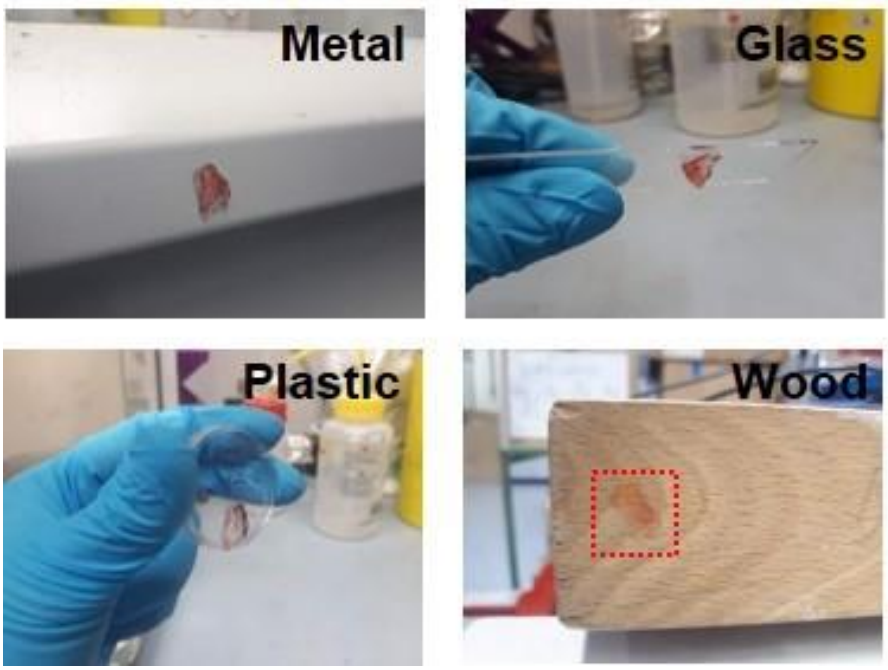

Figure 5-2. Pictures of adhesion test of ion gel on (a) metal, (b) glass, (c) plastic, and (d) wood.

hydrolyzed from maleic anhydride. The AIG can easily adhere to various materials such as metals, plastic, glass, and even wood, as shown in Figure 5-2.

5.3. Fourier-Transform Infrared (FTIR) Spectroscopy

FTIR spectroscopy is a powerful tool to probe the molecular structure of polymers. Figure 5-3 shows the absorbance spectra of film or pellet samples: (a) PVA, (b) PMVE-MA (pellet), (c) PVA/PMVE-MA gel, and (d) PVA/PMVE-MA ion gel (AIG) films. The films of PVA, PVA/PMVE-MA gel, and AIG were prepared as polymeric films. However, the PMVE-MA pellet was prepared by blending KBr powder and pelletized using a hydraulic press due to the complexity regarding its film preparation. Each sample shows characteristic peaks related to their molecular structures. In the absorbance spectra, we can identify the CC structures created by the ring-opening esterification in the AIG. PMVE-MA has two intrinsic peaks at 1856 cm^{-1} and 1783 cm^{-1}, corresponding to symmetrical or asymmetrical stretching bands of C=O in cyclic anhydride.[103] These two peaks disappear in PVA/PMEA-MA gel

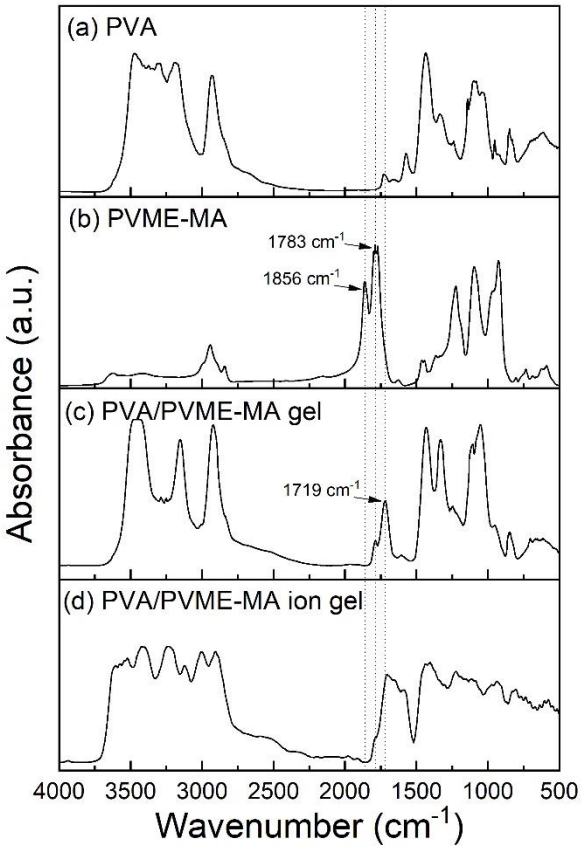

Figure 5-3. Absorbance spectrums of Fourier-transform infrared spectroscopy (FT-IR); (a) PVA film, (b) PVME-MA pellet with KBr, (c) PVA/PVME-MA gel film, and (d) PVA/PVME-MA ion gel (Adhesive ion gel, AIG) film. PVME-MA is pelletized by hydraulic pressure because of the difficulty to make a polymer film. DMSO is fully evaporated for film making of PVA, PVA/PMVE-MA gel, and PVA/PMVE-MA ion gel.

and AIG films, and the overlapped peak noticeably rises at 1719 cm^{-1} (Figure 5-3(c) and (d)). This overlapped peak results from the carbonyl (C=O) groups of carboxylic acid (1718 cm^{-1}) and ester (1720 cm^{-1}), structured by the reaction of cyclic anhydride of PMVE-MA with the hydroxyl group of PVA.[111–113] Broad peaks over 2700 cm^{-1} in PVA films are also attributed to the O-H absorption band of alcohol (Figure 5-3(a)), and PVA/PMVE-MA gel and AIG films show the O-H absorption bands of alcohol and carboxylic acid. The absorbance spectra of PMVE-MA (Figure 5-3(b)) do not show the O-H absorption peaks, indicating that PMVE-MA is not hydrolytically damaged by humidity. With the FTIR spectra, it is determined that the self-assembled gelation by ring-opening esterification creates the CC structures.

5.4. Electrochemical Impedance Spectroscopy (EIS)

The analysis of electrochemical impedance spectroscopy (EIS) was performed to investigate the frequency-dependent behavior, the ionic conductivity, and the capacitance of the AIG. For the measurement, the bulk film of the AIG was prepared and assembled in the Swagelok cell as shown in Figure 5-4(a). The impedance result is processed and plotted in the Bode plot in Figure 5-4(b). The Bode plot shows a plateau region of log (|Z|) in the high-frequency range (> 30 kHz). This region depicts the bulk resistance (R_{bulk}), at which the conducting ions of [EMIM][OTf] are not able to form the electric double layer (EDL) due to the high frequency [92]. However, when the frequency is below 9.3 kHz, where the phase angle (°) is lower than −45°, the conducting ions in the gel matrix can migrate and form the EDL at the interface of electrode and ion gel [65,94]. Below 1 kHz, a phase angle of AIG is saturated to 70° and shows the capacitive behavior (a phase angle of ideal capacitive behavior: −90°), and log (|Z|) linearly increases by the effect to the EDL formation as the frequency decreases.

The ionic conductivity (σ) is an important property which helps determine the speed of the EDL formation and the gating-performance in the EGTs. The ionic conductivity of the AIG can be calculated using the results of the EIS using Equation 5.1.

$$\sigma = \frac{d}{AZ_{re}} \tag{5.1}$$

A and d are the surface area and the thickness of the AIG, respectively, and Z_{re} is the real part of the impedance. The ionic conductivity of AIG is calculated to 4.8 mS cm^{-1} over 30 kHz, in which R_{bulk} from ion migration is measured without the effect of dipole relaxation or EDLs [65,94]. Below 9.3 kHz, the ionic conductivity declines linearly as the frequency decreases because the electrode polarization by the EDL obstructs ion mobility [119,120].

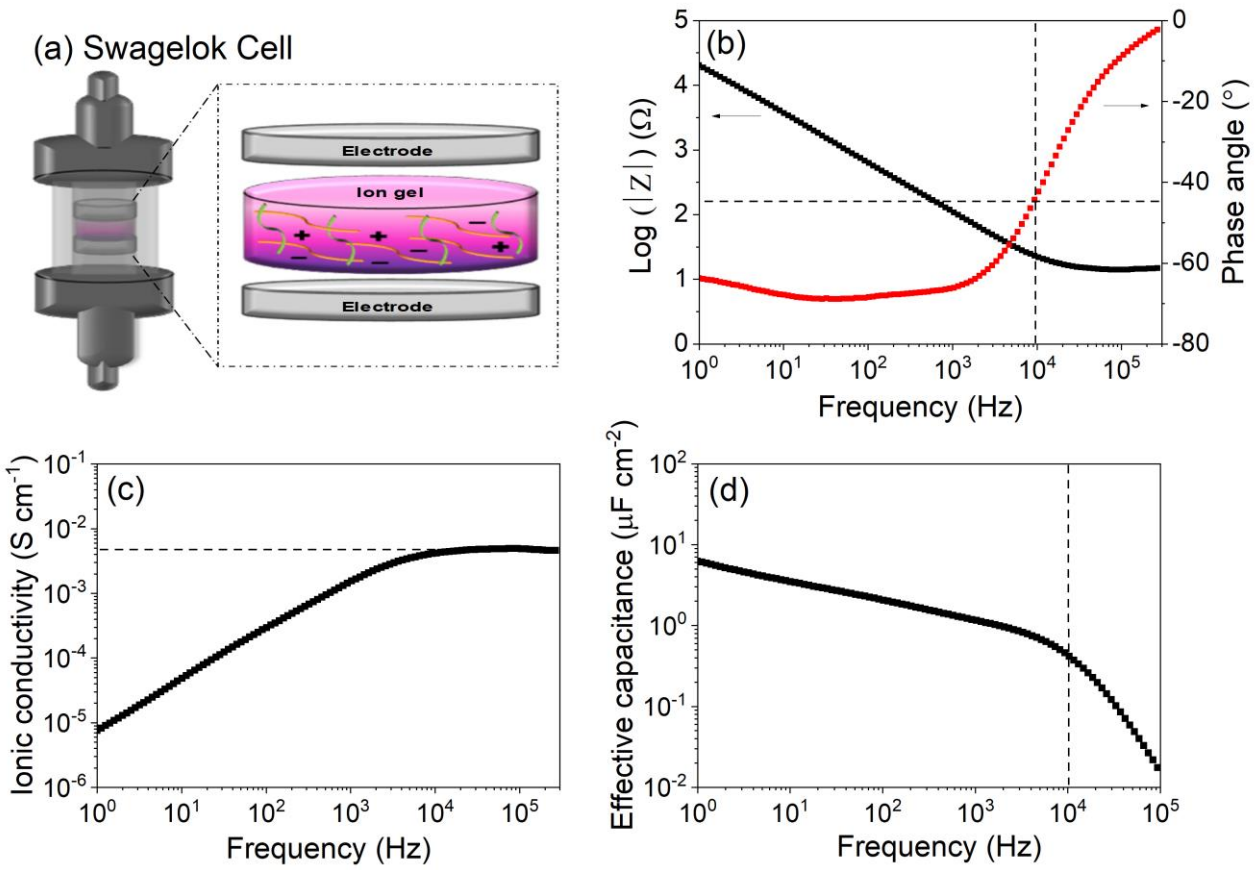

Figure 5-4. The plots of electrochemical impedance spectroscopy of PVA/PMVEA ion gel; (a) illustration of Swagelok cell and adhesive ion gel, (b) Bode plot, (c) ionic conductivity versus frequency plot, and (d) specific capacitance versus frequency plot. Film thickness and diameter are 0.76 mm and 12 mm.

The capacitance is a crucial factor influencing the gating performance because the capacitance of the gate insulator is proportional to the current flowing through the semiconductor channel of the EGT. The capacitance from the EDL of the AIG can be measured as an effective capacitance (C_{eff}) by the EIS. The C_{eff} is calculated by Equation 5.2 based on the results of EIS analysis.

$$C_{eff} = \frac{-Z_{im}}{2\pi f A|Z|^2} \quad (5.2)$$

Z_{im} is the imaginary part of the impedance, f is the frequency, and A is the surface area of AIG. Figure 5-4(d) shows the calculated C_{eff}, differentiated in high- and low-frequency. In the high-frequency region (>9.3 kHz), the C_{eff} significantly decreases due to the insufficient time allowed for the formation of EDLs at the interface of the electrodes. However, in the low-frequency region (<0.3 kHz), the C_{eff} increases as the frequency decreases because conducting ions can migrate to form EDLs. The C_{eff} value is calculated to 6.23 μF cm^{-2} at 1 Hz. These results indicate that the AIG shows typical frequency-dependent behaviors and has noticeably high ionic conductivity and effective capacitance.

5.5. Electrolyte-Gated Transistors (EGTs) Fabricated through the Film-Attachment of AIG

Electrolyte-gated transistors (EGTs) were fabricated to investigate the gating performance of the AIG. The electric circuit and semiconducting channels were prepared using lithography and ink-jet printing techniques. The electrodes of gate, source, and drain were patterned by laser ablation on indium tin oxide (ITO)-coated glass substrates. Then, indium oxide (In_2O_3) precursor was printed using ink-jet printing on the area between source and drain electrodes and annealed to convert to In_2O_3 semiconductor. The AIG film was laminated onto the patterned electrode and semiconductor by hand as shown in Figure 5-5(a). The AIG film can be attached by its adhesive property without any treatment.

The fabricated EGTs using AIG film were analyzed, as shown in Figure 5-5. The drain-source current (I_d) versus gate-source voltage (V_g) plot (Figure 5-5(b)) shows the transfer curves of the EGT. The transfer curves have narrow hysteresis due to the fast formation and deformation of EDLs in the AIG due to high ionic conductivity. The threshold voltage (V_{th}) of the transfer curve is calculated

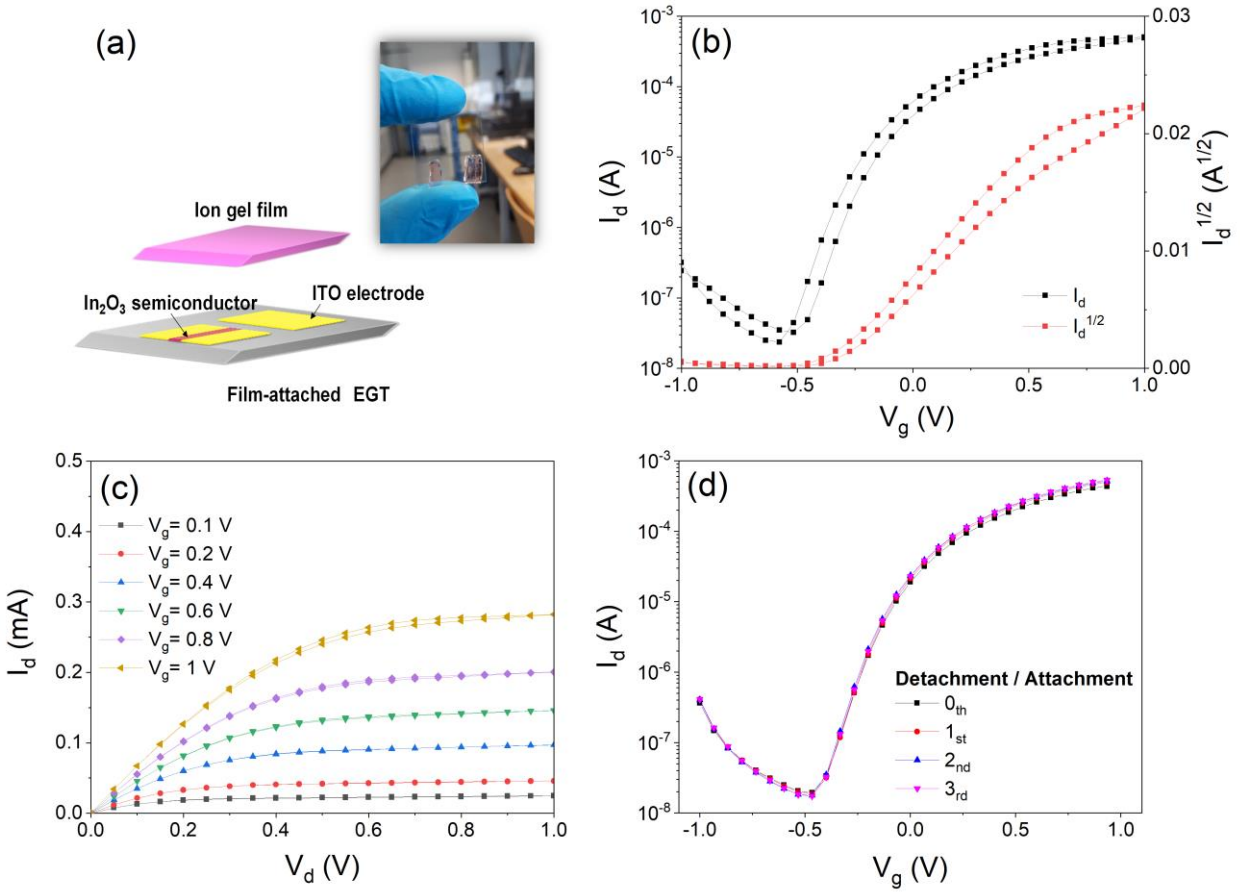

Figure 5-5. Characterization of in-plane, film-attached EGTs; (a) illustration and picture of in-plane, film-attached EGTs, (b) gate-source voltage (V_g) versus drain-source current (I_d) and $I_d^{1/2}$ plots at 1 V of drain-source voltage (V_d), (c) V_d versus I_d plot at different V_g, and (d) V_g versus I_d plots for attachment/detachment test of ion gel film. Channel width and length are 2 mm and 50 μm.

to −0.36 V by the extrapolation of $I_d^{1/2}$. The on/off current ratio (I_{on}/I_{off}) and the subthreshold swing (SS) are calculated to 2.24×10^4 and 117.24 mV dec^{-1}, respectively. Moreover, output characteristic curves of the fabricated EGTs are plotted in Figure 5-5(c). These results display linear and saturation regions, varied by V_d and V_g. At low V_d, I_d linearly increases, and then becomes saturated at high V_d. The saturation of the I_d is related to the capacity of current channels in the semiconductor, controlled by V_g. The capacity of current channels increases when the applied V_g increases. Thereby, currents can flow better through current channels in the saturation region. The output characteristic curves illustrate that the fabricated EGTs can operate appropriately, even though gate insulators are fabricated by the film-attachment of the AIG films.

Furthermore, AIG films have reusability. Figure 5-5(d) shows the transfer curves of EGTs measured by attaching and detaching the AIG films on the electrode and the semiconductor by hand. Although the AIG films were attached and detached by hand several times, the fabricated EGTs showed similar transfer curves, independent of attaching/detaching times. And also, since the adhesion of AIG film is not too strong and not too weak, attaching and detaching the AIG films does not damage In_2O_3 semiconductors and ITO electrodes. This is possible because the contacts between In_2O_3 semiconductors and glass substrates by Van der Waals interactions are stronger than the adhesion between In_2O_3 semiconductors and AIG films. Therefore, it is identified that the AIG film has good reusability and can be detached and reattached to the electrode and the semiconductor several times without degradation of gating performances in EGTs.

In addition, two types of EGTs were prepared to compare the gating performance depending on the fabrication techniques. Figures 5-6(a) and (b) illustrate the fabrication of the gate insulator

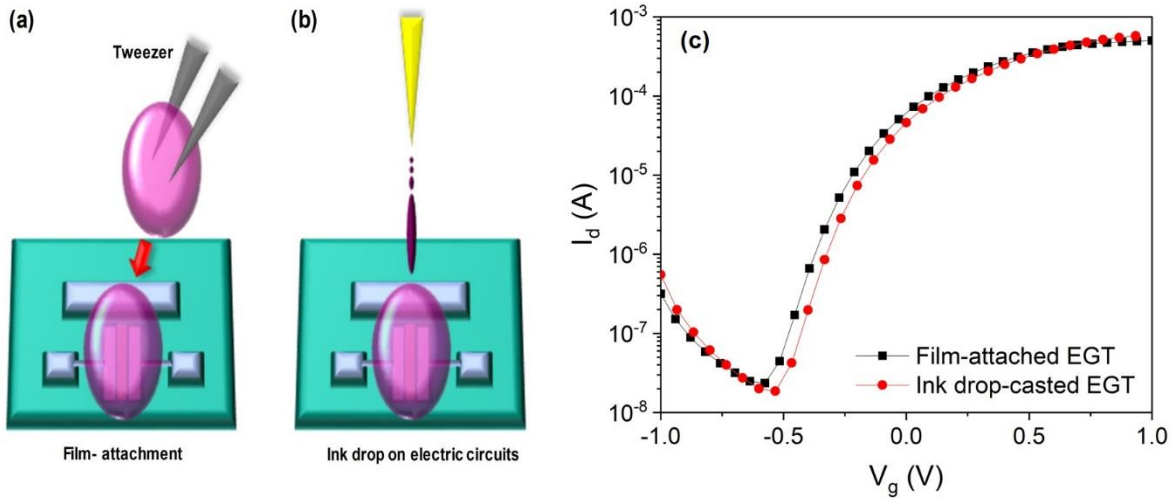

Figure 5-6. Illustration of (a) film-attachment and (b) ink drop-casting procedure for EGT fabrication, and (c) V_g versus I_d plots of ion gel film-attached EGT (black) and ink drop-cased EGT (red). Channel width and length are 2 mm and 50 μm. Humidity level and temperature are room condition.

through either film attachment or drop-casting ink using a pipette, respectively. Figure 5-6(c) show their transfer curves. The ink recipes used in both methods are the same. For the ink drop-casting method, the ink was dropped onto the semiconductor and electrode before the self-assembled gelation occurred. The self-assembled gelation occurred after dropping the ink, and the AIG was spontaneously synthesized onto the semiconductor and the electrodes. The transfer curves of the EGTs fabricated by both methods are similar (Figure 5-6(c)). The on/off ratios of ink drop-casted EGT and film-attached EGT are calculated to 3.03×10^4 and 2.24×10^4, respectively, and ink drop-casted EGT has slightly higher on/off ratio than film-attached EGT. Compared to V_{th} of ink drop-casted EGT, V_{th} of film-attached EGT is a bit negatively shifted from −0.32 V to −0.36 V. And also, SS values of ink drop-casted EGT and film-attached EGT are measured to 119.06 mV dec^{-1} and 117.24 mV dec^{-1}, respectively, which are almost the same. This result indicates that the surface contact by film-attachment is equivalent to that by ink drop-casting, so both exhibit similar gating performance.

Table 5-1. Electrical parameters of EGTs (Figure 5-5(c))

Type of EGTs	**On-current [A]**	**Off-current [A]**	**On/off current ratio [10^4]**	**Subthreshold Swing [mV dec^{-1}]**	**Threshold voltage [V_{th}]**
Film-attached EGTs	5.02×10^{-4}	2.36×10^{-8}	2.24	117.24	−0.36
Ink drop-casted EGTs	5.65×10^{-4}	1.86×10^{-8}	3.03	119.06	−0.32

5.6. Fabrication of EGTs through Ink-Jet Printing

The AIG is designed for the simple fabrication of the EGTs through the film-attachment method, but it can also be used for ink-jet printing. In chapter 4, the dilute ink system was described, where the excessive amount of DMSO inhibits the self-assembled gelation. The ingredients of the AIG can also apply to the dilute ink system and ink-jet printing process to fabricate the gate insulator of the EGT. The ratio of PVA, PMVE-MA, and [EMIM][OTf] are fixed, and only the ratio of DMSO is modified. Figure 5-7 shows the transfer curves of the EGTs fabricated with ink-jet printing with the dilute inks of the AIG. This EGT is not the in-plane structure, but the top-gated structure, as shown in chapter 4. The length and width of the In_2O_3 semiconductor are 600 μm and 20 μm, respectively. After preparing the AIG on the semiconductor, PEDOT:PSS was printed onto the AIG as a top-gate electrode. The ink-jet printed AIG exhibits outstanding gating performance. Although the on/off current ratio calculated to 6.53×10^5 is higher than that of film-attached EGTs in Figure 5-5, it results from the different length and width of semiconductor and geometry of EGTs. These results

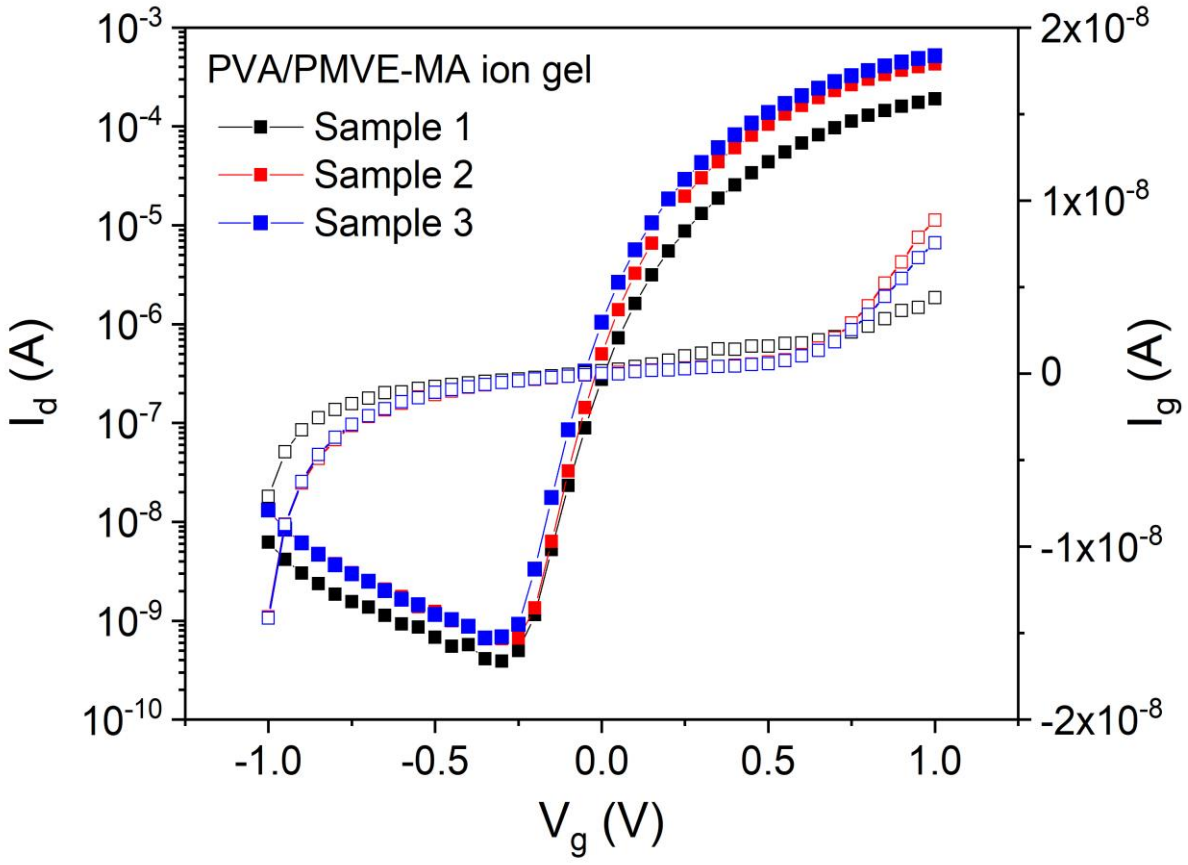

Figure 5-7. V_g versus I_d and I_g plot of top-gated, ion gel-gated transistors fabricated by ink-jet printing. The dilute ink of adhesive ion gel (AIG) was printed by ink-jet printer. V_d is 1 V and RH is 20 %. The channel width and length are 600 μm and 20 μm.

demonstrate that the composition of the AIG, developed for the film-attachment method, can also be utilized with the dilute ink system and ink-jet printing, as shown in chapter 4. In addition, the ink-jet printed AIG shows good reproducibility, as shown in Figure 5-7. There are no differences between V_{th} and SS of three samples. On/off current ratio of Sample 1 (black) calculated to 4.86 $\times 10^5$ is slightly lower than that of Sample 2 (red) and 3 (blue), which have on/off current ratios of 6.53×10^5 and 7.57×10^5, respectively. However, their differences are not large. Therefore, the fabrication methods of gate insulators using AIG can be diversified with film-attachment and ink-jet printing methods.

5.7. Humidity Stability Test of AIG-gated EGTs

Humidity stability is an essential property of gate insulators of EGTs. It is because stable gate performances must be achieved even at low and high humidity levels for practical use at ambient conditions. AIG-gated EGTs were tested to analyze their stabilities at different relative humidity (RH) levels. For the measurement, RH levels were precisely controlled from 30 % to 90 %. Gate insulators of AIG-gated EGTs were fabricated by film-attachment of AIG films on electrodes and semiconductors. The width and length of In_2O_3 semiconducting channels are 2 mm and 50 μm,

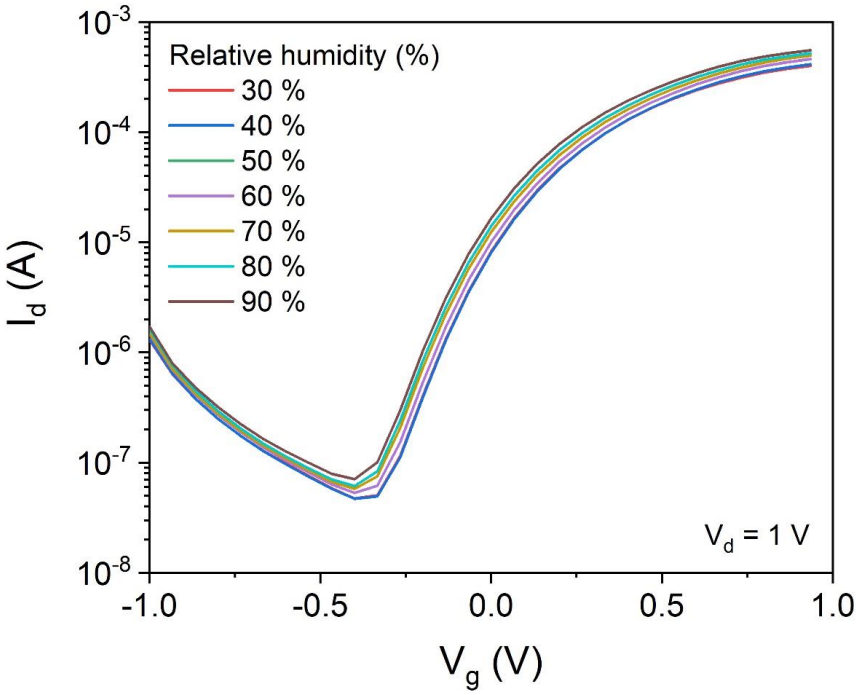

Figure 5-8. Transfer curves of AIG-gated EGTs measured at different relative humidities (R.H.) for humidity stability test. The R.H. conditions were controlled from 30 % to 90 %, and source-drain voltage (V_d) was set to 1 V. Gate voltages (V_g) were swept from -1 V to 1 V during measurement. The width and length of In_2O_3 semiconducting channels are 2 mm and 50 μm, respectively.

respectively. Figure 5-8 shows the transfer curves of AIG-gated EGTs measured at 1 V_d. Notably, AIG films exhibit very stable gating performances at all RH levels. There are no differences in V_{th} and SS, depending on RH levels. Therefore, this result can be understood that the influence of water molecules on ionic conductivity and formation of EDLs by [EMIM][OTf] is negligible. This humidity stability enables AIG films to be utilized at room conditions without encapsulation.

5.8. Summary

In summary, adhesive ion gel (AIG) used for gate insulators of the EGTs was developed. The AIG was designed for manufacturing gate insulators of the EGTs with film attachment. In particular, facile synthesis by the self-assembled gelation is an excellent advantage to use AIG films for the EGTs. The adhesive property of the AIG results from the functional groups of PMVE-MA. MVE is a pressure-sensitive adhesive, and maleic acid cleaved from maleic anhydride can make a hydrogen bond with substrates to induce adhesion. These adhesive properties enable the gate insulator to be laminated onto the semiconductor and electrode of the EGTs by hand. The AIG has an outstanding ionic conductivity of 4.8 mS cm^{-1} at room temperature using Swagelok cell and an effective capacitance of 6.23 μF cm^{-2} at 1 Hz. Moreover, in the EGTs as a gate insulator, the AIG exhibits stable transfer curves and remarkable SS and I_{on}/I_{off} ratios. Moreover, the AIG film has reusability enabling it to be attached and detached to the electrode and the semiconductor several times by hand without the loss of gating performance. These results present the possibility for the development of ionic conductive 'stickers', which can be easily utilized in the EGTs without any deterioration.

When it comes to comparing the gating performances between PVA/PEMA ion gel (Chapter 4) and AIG, there are no significant differences. In Figure 5-9, the transfer curves of the PVA/PEMA ion gel and AIG-gated EGTs fabricated by ink-jet printing are plotted. These transfer curves show almost similar on/off current ratios, Vth, and SS values. Their similar gating performances result from the similar synthesis mechanism and the use of the same ionic liquid of [EMIM][OTf]. However, the film-attachment method, using the adhesive property of the AIG film, has advantages in terms of fabricating multi-layered EGT structures. Printing techniques are fast, effective to fabricate EGTs, but using solvents for printing can trigger adverse effects such as swelling, dissolution, and penetration of polymers and organic materials by solvents.[142,143] However, film-attaching can prevent those adverse effects in the fabrication of multi-layered structures of EGTs. And also, it can shorten manufacturing time by removing the drying process to remove solvents. The AIG is a new kind of polymer electrolyte, that has not previously reported, and showed the possibility of being applied to many applications. This study presents new insight to fabricate EGTs not only by printing techniques but also by film-attachment.

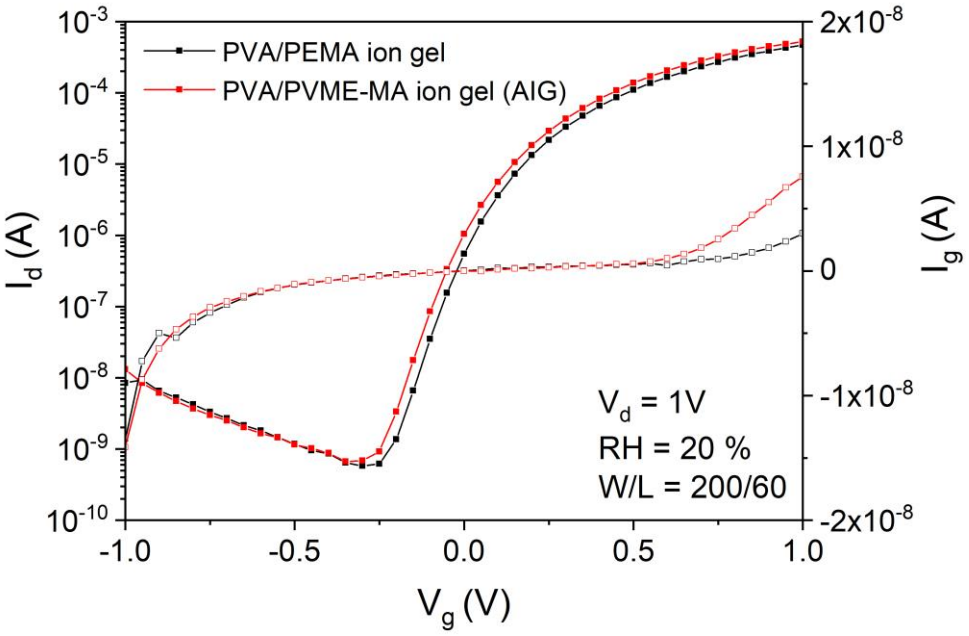

Figure 5-9. Transfer curves of PVA/PEMA ion gel-gated EGTs (Chapter 4) and AIG-gated EGTs measured at 20 % relative humidity (R.H.). Source-drain voltage (V_d) was set to 1 V. Gate voltages (V_g) were swept from -1 V to 1 V during measurement. The width and length of In_2O_3 semiconducting channels are 200 μm and 60 μm, respectively.

Chapter 6

6. Conclusion

This thesis shows the development of a chemically cross-linked ion gel for electronic devices. As detailed in Chapters 4 and 5, new types of ion gels were successfully developed and applied to electrolyte-gated transistor (EGT). The new findings are summarized below.

1. **The easy synthesis method of chemically cross-linked ion gel by self-assembled gelation**
   The synthesis of chemically cross-linked (CC) ion gel is the main highlight of this thesis. The key technique to synthesize CC ion gel is to use ring-opening esterification between cyclic anhydride and hydroxyl groups for self-assembled gelation. This reaction is spontaneous at room temperature in a viscous solution. With the self-assembled gelation, CC ion gel can be easily synthesized without any complicated procedures. Studies of the ring-opening esterification of cyclic anhydride and hydroxyl groups have been published in the fields of organic chemistry or polymers. However, for the first time, the utilization of the ring-opening esterification for the synthesis of CC ion gel has been shown in this thesis. Moreover, the ratio of the composition of CC ion gel was also optimized to induce the self-assembled ion gel at room temperature.

2. **The development of CC ion gel ink for ink-jet printing**
   Ink-jet printable ink for CC ion gel is another highlight of this thesis. In general, there have been no reported ink-jet printable inks for CC ion gel, primarily due to the irreversible gel structure and the nozzle blockage of the printing head. However, in this study, ink-jet printable ink of CC ion gel was invented and was successfully applied to the ink-jet printing process to fabricate EGTs. For the ink-jet printability of CC ion gel, the self-assembled gelation was inhibited by adding an excessive amount of solvent to the ion gel ink. In a dilute solution, macromolecules

are well separated and lose their interaction. Hence, the self-assembled gelation is inhibited. The inhibited gelation starts after ink-jet printing due to the evaporation of the solvent. The inhibition and self-assembled gelation are affected by the ink ratio of ingredients. Therefore, the ink recipe was carefully optimized to control the self-assembled gelation.

3. The stability of gating performance against humidity

Composite solid polymer electrolyte (CSPE) has the drawback that the ionic conductivity drops drastically at low humidity. For this reason, the CSPE does not work in EGTs at low humidity (≤ 20 %). However, the new ion gel overcomes the drawback of CSPE and shows stable gating performance in the EGTs at low humidity levels. Ion gels contain ionic liquid, which has negligible volatility. Therefore, they can exhibit stable gate performances in the relative humidity range from 20 % to 90%.

4. Film-attachment fabrication for gate insulator of EGTs

Adhesive ion gel (AIG), discussed in Chapter 5, allows the fabrication of the gate insulator of EGTs by the film-attachment method. The AIG film was prepared by self-assembled gelation of PVA and PMVE-MA. The adhesion resulting from the functional groups of PMVE-MA enables the lamination of AIG films on electrodes and semiconductors by hand. The film-attached EGTs exhibit remarkable gating performances, which are almost similar to the ink drop-casted EGTs. The developments reported here make it easy to manufacture the gate insulator of EGTs not only by ink-jet printing but also by film attachment.

5. The advantages of the developed CC ion gels compared to state-of-the-art ABA triblock ion gels

In the aspect of developing ion gels, the discovery of PVA/PEMA and PVA/PVME-MA ion gels is a remarkable achievement. Compared to the state-of-the-art ABA triblock ion gels, which are considered the best for gate insulators of EGTs, they show noticeable improvements in thermal stability, synthesis, and ionic conductivity. Table 6-1 lists the properties of representative ABA triblock ion gels and the developed CC ion gels.

The most prominent advantage is the simplicity of synthesis. To synthesize ABA triblock ion gels, ABA triblock copolymers should be synthesized by reversible addition−fragmentation chain-transfer (RAFT) polymerization, and it must be optimized to efficiently form micelle structures by adjusting the length of each block during the synthesis process. However, the synthesis of PVA/PEMA or PVA/PVME-MA ion gels does not require such complex synthetic techniques because the chemically cross-linking reaction is spontaneous at room temperature by ring-opening esterification. The RAFT polymerization is an effective method to synthesize copolymers by precisely controlling molecular weight, low molar mass dispersity, and high end-group fidelity.[144] However, using polymerization itself is complex, and the synthesis method

by spontaneous ring-opening esterification is much easier. The simple synthesis method is beneficial for scaling up mass production; therefore, the developed CC ion gels are more advantageous for the commercialization of gate insulators of EGTs.

The second advantage is the thermal stability of gel structures. Since the ABA triblock ion gel forms a cross-linking point by micelles, the physically cross-linked (PC) structures by micelles can be released if the temperature is over 100 ℃. However, CC gel structures of the developed ion gels are stable even if the temperature is higher than 180 ℃. It is because their cross-linked structures are thermoset with CC structures. Over 189 ℃, the DMSO, which is a residue and trapped in gel structures, can be boiled (boiling point of DMSO ($T_{b.p.}$): 189 ℃). Therefore, there is a significant development in terms of the thermal stability of gel polymer structures in comparison with ABA triblock ion gels.

Lastly, the developed CC ion gels have enhanced ionic conductivities of ~5 mS cm^{-1} compared to ABA triblock ion gels. The ionic conductivities of developed CC ion gels are higher than that of the reported ABA triblock ion gels, e.g., SOS/[BMIM][PF_6] and SMS/[EMIM][TFSI] (Table 6-1).[65,71,72,75] Considering that ionic conductivity of [EMIM][OTf] is ~8 mS cm^{-1} at room temperature, the ionic conductivities of developed CC ion gels reach to the maximum that ion gel system can achieve.

These results can further lead to the use of CC ion gel as gate insulators of EGTs, beyond PC ion gel, which has been extensively utilized. The easy synthesis and superior performance of the developed CC ion gel also have advantages compared to the PC ion gels reported in earlier studies. The discovery of new materials and the optimization of materials for the fabrication process, thereby broadening the range of applicable fabrication techniques, are reported in this thesis. Moreover, these results prove that the developed CC ion gel exhibits superior properties and outstanding gating performance compared to other reported polymer electrolytes or ion gels. These new findings give new insight for using CC ion gel in the field of printed electronics.

Table 6-1. list of materials properties of ABA Triblock ion gels, PVA/PEMA ion gel, and PVA/PVME-MA ion gel.

		ABA Triblock Ion Gel		CSPE	PVA/PEMA Ion Gel (Chapter 4)	PVA/PVME-MA Ion Gel (Chapter 5)
		[71]	[121]	[83]		
Composition	**Backbone polymer**	poly(styrene-b-ethylene oxide-styrene-b-stytene), (SOS)	poly(styrene-b-methyl methacrylate-b-styrene), (SMS)	PVA	PVA / PEMA	PVA / PVME-MA
	Conducting ion / Plasticizer	[BMIM][PF_6]	[EMIM][TFSI]	$LiClO_4$ (salt)/ propylene carbonate (plasticizer)	[EMIM][OTf]	[EMIM][OTf]
Ionic Conductivity (S cm^{-1}) at 25 ℃		2.5	~0.2	~3	5	4.8
Cross-linked Structure		Physically cross-linked structures by micelle		Physically cross-linked structure by polymeric entanglement	Covalent-bonded, chemically cross-linked structures by ester group	
Effective Capcaitance (μF cm^{-2}) at 1 Hz)		n.a.	~9.9	~5	5.4	6.23
Synthesis Method		Reversible addition−fragmentation chain-transfer (RAFT) polymerization and micellization		Blend of compositions	Spontaneous ring-opening esterification	
Synthesis Complexity		Complex		Simple	Simple	
Thermo-stability		Low (<100 ℃)		-	High (>180 ℃)	
		Thermoplastic		thermoplastic	Thermoset	

A. Acknowledgments

The completion of this thesis would not have been possible without the contributions and support of many individuals whom I genuinely appreciate. However, there are a few that made signifcant contributions to this thesis and impacted this experience in a positive way for me. Therefore, I would like to take this section to express my gratitude to those individuals and highlight their efforts as a special thank you.

First of all, I would like to express my gratitude to Prof. Dr. -Ing. Horst Hahn. He accepted me as his Ph.D. student and allowed me to study at the Institute of Nanotechnology (INT). He always provided me with helpful advice, support and guidance which enabled me to solve many scientific problems in research. For this, I am truly grateful.

I would like to express my greatest thanks to Dr. Ben Breitung, who is the leader of the printed electronics group. I am sincerely grateful to him for helping me since I first contacted this group. He taught me many things, and I could mature as a researcher through his guidance. As a patient and understanding group leader, he always supported and trusted me. Without his help, it would have been difficult for me to finish this work.

I would like to thank Prof. Dr. Jasmin Aghassi-Hagmann. She had an open mind and always actively advised me about the research. Her valuable advice was extremely helpful for this research.

I am thankful to Dominic Boll, who was my office mate for 2 years. He supported me in a new cultural environment and helped me navigate through various issues I had when adjusting to my new surroundings. He provided a lot of emotional support and taught me a lot about the importance of diversity and for that, I am extremely grateful.

I am grateful to Gabriel Cadilha Marques, Xiaowei Feng, and Surya Abhishek Singaraju. They primarily contributed to this thesis in a more practical way. Gabriel and Suyra helped me fabricate and measure electrolyte-gated transistors using ion gel, and Xiaowei helped analyze the result of electrochemical impedance spectroscopy.

I would like to thank Parvathy Anitha Sukkurji. We tried to develop ionic liquid-based electrolytes for lithium-ion batteries, and she helped me to assemble and measure battery performances.

I would like to thank Dr. Shyam Swaroop Katnagallu and Daisy Agrawal for helping me proofread this thesis.

I would like to express my gratitude to Deutscher Akademischer Austauschdienst (DAAD), for providing a financial grant to me to study in Germany through doctoral scholarship programs.

I would like to sincerely thank Yeseul Lee, who supported and believed my dream of studying abroad in Germany. She always encouraged me whenever I was in trouble and had a hard time. It was with her care and support that I was able to complete this thesis.

I am thankful to my brother, Jaewon Jeong, who always provided me with motivation whenever research gave me a tough time. Congratulations on your first job, I am very proud of you.

마지막으로, 아버지와 어머니에게 감사드립니다. 한결같은 사랑으로 보살펴 주시고 조언과 응원을 아끼지 않아 주신 부모님의 도움으로 무사히 박사과정을 마칠 수 있게 되었습니다. 독일에서 연구하고 완성한 이 졸업논문을 사랑하는 아버지와 어머니에게 바칩니다.

B. List of Abbreviations and Symbols

IL	Ionic liquid
SEI	Solid electrolyte interface
$AlCl_3$	Aluminum chloride
$[EtNH_3][NO_3]$	Ethylammonium nitrate
$[EMIM]^+$	1-Ethyl-3-methylimidazolium
$[IM]^+$	Imidazolium
$[Pyr_{xy}]^+$	x,y-Alkyl pyrrolidinium
$[Py_{xy}]^+$	x,y-Alkyl-pyridinium
$[Pip_{xy}]^+$	x,y-Alkyl-piperidinium
$[TFSI]^-$	Bis(trifluoro-methanesulfonate)
$[OTf]^-$	Trifluoromethanesulfonate or triflate
$[FSI]^-$	Bis(fluorosulfonyl)imide
$[PF_6]^-$	Hexafluorophosphate
$[BF_4]^-$	Tetrafluoroborate
$[(FSO_2)(C_2F_5SO_2)N]^-$	(Fluorosulfonyl)(pentafluoroethanesulfonyl)imide
$[TFAC]^-$	(2,2,2-trifluoro-N-(trifluoromethylsulfonyl)acetamide
$[CTMA]^-$	Cyanomethyltrimethylammonium
$[N_{1,1,1,4}]^-$	Butyltrimethylammonium
EIS	Electrochemical impedance spectroscopy
SPE	Solid polymer electrolyte
PEO	Poly(ethylene oxide)
GPE	Gel polymer electrolyte
PEMFC	Proton exchange membrane fuel cell
PE	Polymer electrolyte
PC	Propylene carbonate
PC	Physically cross-linked
CC	Chemically cross-linked
PVP-PS-PVP	Poly(vinyl pyridine)-polystyrene-poly(vinyl pyridine)
PS-PEO-PS	Poly(styrene-block-ethylene oxide-block-styrene)
Z_R	Resistor
Z_C	Capacitor
Z' or Z_{re}	Real part of impedance
Z'' or Z_{im}	Imaginary part of impedance
R_p	Polarization resistance in parallel circuit
C_{dl}	Electric-double layer capacitance

R_s	Solution resistance
R_{ct}	Charge transfer resistance
Z_w	Warburg element
κ_f	Forward electron transfer constant
κ_b	Backward electron transfer constant
D_O	Oxidant diffusion coefficient
D_R	Reductant diffusion coefficient
R_{ext}	External resistance
R_{el}	Electrolyte resistance
R_{bulk}	Bulk resistance
R_{diff}	Diffusion layer resistance
R_{dl}	Formation resistance of electric double-layer
$\sigma_{a.c.}$	*a.c.* ionic conductivity
$\sigma_{d.c.}$	*d.c.* ionic conductivity
σ^*	Complex ionic conductivity
σ'	Real part of ionic conductivity
σ''	Imaginary part of ionic conductivity
C_{eff}	Effective capacitance
DOD	Drop-on-demand
R2R	Roll-to-roll
MOSFET	Metal oxide semiconductor field-effect transistor
EGT	Electrolyte-gated transistor
N-FET	N-channel field effect transistor
P-FET	P-channel field effect transistor
V_g	Gate voltage
V_{fb}	Flat band voltage
V_{th}	Threshold voltage
V_{ds}	Drain-source voltage
I_{ds}	Drain-source current
Q_{inv}	Accumulated charges in the inversion layer
C_{dep}	Capacitance at the depletion layer
C_{oxe}	Capacitance at the oxide layer
T_{oxe}	Electrical oxide thickness
W_{dmax}	Maximum thickness of the inversion layer
V_{gs}	Gate-source voltage
V_{cs}	Channel-source voltage
V_{th}	Threshold voltages

IHP	Inner Helmholtz plane
OHP	Outer Helmholtz plane
I_{off}	Off-current
I_{on}	On-current
SS	Subthreshold swing
SEM	Scanning electron microscopy
FT-IR	Fourier-transform infrared
EGT	Electrolyte-gated transistor
KBr	Potassium bromide
MMA	Methyl methacrylate
PVA	Poly(vinyl alcohol)
PEMA	Poly(ethylene-*alt*-maleic anhydride)
PMVE-MA	Poly(methyl vinyl ether-*alt*-maleic anhydride)
PVDF	Polyvinylidene fluoride
[EMIM][OTf]	1-ethyl-3-methylimidazolium trifluoromethanesulfonate
CSPE	Composite solid polymer electrolyte
DMSO	Dimethyl sulfoxide
$LiClO_4$	Lithium perchlorate
PTFE	Poly(tetrafluoroethylene)
PEDOT:PSS	Poly(3,4-ethylenedioxythiophene)-poly(styrenesulfonate)
EBL	Electron beam (e-beam) lithography
ITO	Indium tin oxide
R.H.	Relative humidity
MVE	Methyl vinyl ether
AC	Alternating current

C. List of Figures

D. References

[1] S. Arrhenius, Recherches sur la conductibilité galvanique des électrolytes, PA Norstedt & Söner. (1884).

[2] C. Zhong, Y. Deng, W. Hu, J. Qiao, L. Zhang, J. Zhang, A review of electrolyte materials and compositions for electrochemical supercapacitors, Chem. Soc. Rev. 44 (2015) 7484–7539. https://doi.org/10.1039/C5CS00303B.

[3] B. Raguse, E. Chow, C.S. Barton, L. Wieczorek, Gold Nanoparticle Chemiresistor Sensors: Direct Sensing of Organics in Aqueous Electrolyte Solution, Anal. Chem. 79 (2007) 7333–7339. https://doi.org/10.1021/ac070887i.

[4] M.-J. Spijkman, J.J. Brondijk, T.C.T. Geuns, E.C.P. Smits, T. Cramer, F. Zerbetto, P. Stoliar, F. Biscarini, P.W.M. Blom, D.M. de Leeuw, Dual-Gate Organic Field-Effect Transistors as Potentiometric Sensors in Aqueous Solution, Adv. Funct. Mater. 20 (2010) 898–905. https://doi.org/10.1002/adfm.200901830.

[5] C. Ding, J. Shi, Z. Wang, C. Li, Photoelectrocatalytic Water Splitting: Significance of Cocatalysts, Electrolyte, and Interfaces, ACS Catal. 7 (2017) 675–688. https://doi.org/10.1021/acscatal.6b03107.

[6] O. Khaselev, J.A. Turner, Electrochemical Stability of p-GaInP2 in Aqueous Electrolytes Toward Photoelectrochemical Water Splitting, J. Electrochem. Soc. 145 (1998) 5.

[7] P.V. Wright, Electrical conductivity in ionic complexes of poly(ethylene oxide), Brit. Poly. J. 7 (1975) 319–327. https://doi.org/10.1002/pi.4980070505.

[8] P. Walden, Molecular weights and electrical conductivity of several fused salts, Bulletin of the Russian Academy of Sciences. (1914) 405–422.

[9] S. Gabriel, J. Weiner, Ueber einige Abkömmlinge des Propylamins, Ber. Dtsch. Chem. Ges. 21 (1888) 2669–2679. https://doi.org/10.1002/cber.18880210288.

[10] J.S. Wilkes, A short history of ionic liquids—from molten salts to neoteric solvents, Green Chem. 4 (2002) 73–80. https://doi.org/10.1039/b110838g.

[11] P. Wasserscheid, T. Welton, Ionic liquids in synthesis, Wiley-VCH, 2004.

[12] A.S. Basin, A.B. Kaplun, A.B. Meshalkin, N.F. Uvarov, The LiCl-KCl binary system, Russ. J. Inorg. Chem. 53 (2008) 1509–1511. https://doi.org/10.1134/S003602360809026X.

[13] F.H. Hurley, T.P. WIer, Electrodeposition of Metals from Fused Quaternary Ammonium Salts, J. Electrochem. Soc. 98 (1951) 203. https://doi.org/10.1149/1.2778132.

[14] H.L. Chum, V.R. Koch, L.L. Miller, R.A. Osteryoung, Electrochemical scrutiny of organometallic iron complexes and hexamethylbenzene in a room temperature molten salt, J. Am. Chem. Soc. 97 (1975) 3264–3265. https://doi.org/10.1021/ja00844a081.

[15] W.-Y. Wen, S. Saito, Apparent and Partial Molal Volumes of Five Symmetrical Tetraalkylammonium Bromides in Aqueous Solutions, J. Phys. Chem. 68 (1964) 2639–2644. https://doi.org/10.1021/j100791a042.

[16] B.E. Conway, R.E. Verrall, J.E. Desnoyers, Partial molal volumes of tetraalkylammonium halides and assignment of individual ionic contributions, Trans. Faraday Soc. 62 (1966) 2738. https://doi.org/10.1039/tf9666202738.

[17] R.L. Kay, T. Vituccio, C. Zawoyski, D.F. Evans, Viscosity B Coefficients for the Tetraalkylammonium Halides, J. Phys. Chem. 70 (1966) 2336–2341. https://doi.org/10.1021/j100879a041.

[18] G.W. Parshall, Catalysis in molten salt media, J. Am. Chem. Soc. 94 (1972) 8716–8719. https://doi.org/10.1021/ja00780a013.

[19] J.S. Wilkes, J.A. Levisky, R.A. Wilson, C.L. Hussey, Dialkylimidazolium chloroaluminate melts: a new class of room-temperature ionic liquids for electrochemistry, spectroscopy and synthesis, Inorg. Chem. 21 (1982) 1263–1264. https://doi.org/10.1021/ic00133a078.

[20] J.S. Wilkes, M.J. Zaworotko, Air and water stable 1-ethyl-3-methylimidazolium based ionic liquids, J. Chem. Soc., Chem. Commun. (1992) 965. https://doi.org/10.1039/c39920000965.

[21] J.E. Gordon, G.N.S. Rao, Fused organic salts. 8. Properties of molten straight-chain isomers of tetra-n-pentylammonium salts, J. Am. Chem. Soc. 100 (1978) 7445–7454. https://doi.org/10.1021/ja00492a001.

[22] H.K. Roobottom, H.D.B. Jenkins, J. Passmore, L. Glasser, Thermochemical Radii of Complex Ions, J. Chem. Educ. 76 (1999) 1570. https://doi.org/10.1021/ed076p1570.

[23] O.R. Luca, J.L. Gustafson, S.M. Maddox, A.Q. Fenwick, D.C. Smith, ChemInform Abstract: Catalysis by Electrons and Holes: Formal Potential Scales and Preparative Organic Electrochemistry, ChemInform. 46 (2015) no-no. https://doi.org/10.1002/chin.201534264.

[24] A.E. Visser, R.P. Swatloski, W.M. Reichert, S.T. Griffin, R.D. Rogers, Traditional Extractants in Nontraditional Solvents: Groups 1 and 2 Extraction by Crown Ethers in Room-Temperature Ionic Liquids †, Ind. Eng. Chem. Res. 39 (2000) 3596–3604. https://doi.org/10.1021/ie000426m.

[25] U. Schröder, J.D. Wadhawan, R.G. Compton, F. Marken, P.A.Z. Suarez, C.S. Consorti, R.F. de Souza, J. Dupont, Water-induced accelerated ion diffusion: voltammetric studies in 1-methyl-3-[2,6-(S)-dimethylocten-2-yl]imidazolium tetrafluoroborate, 1-butyl-3-methylimidazolium tetrafluoroborate and hexafluorophosphate ionic liquids, New J. Chem. 24 (2000) 1009–1015. https://doi.org/10.1039/b007172m.

[26] K. Tochigi, H. Yamamoto, Estimation of Ionic Conductivity and Viscosity of Ionic Liquids Using a QSPR Model †, J. Phys. Chem. C. 111 (2007) 15989–15994. https://doi.org/10.1021/jp073839a.

[27] T. Abe, H. Fukuda, Y. Iriyama, Z. Ogumi, Solvated Li-Ion Transfer at Interface Between Graphite and Electrolyte, J. Electrochem. Soc. 151 (2004) A1120. https://doi.org/10.1149/1.1763141.

[28] T.R. Jow, K. Xu, O. Borodin, M. Ue, Electrolytes for Lithium and Lithium-ion Batteries, Springer, n.d.

[29] F. Endres, N. Borisenko, S.Z. El Abedin, R. Hayes, R. Atkin, The interface ionic liquid(s)/electrode(s): In situSTM and AFM measurements, Faraday Discuss. 154 (2012) 221–233. https://doi.org/10.1039/C1FD00050K.

[30] H. Matsumoto, H. Sakaebe, K. Tatsumi, M. Kikuta, E. Ishiko, M. Kono, Fast cycling of Li/LiCoO2 cell with low-viscosity ionic liquids based on bis(fluorosulfonyl)imide [FSI]−, Journal of Power Sources. 160 (2006) 1308–1313. https://doi.org/10.1016/j.jpowsour.2006.02.018.

[31] K. Liu, Y.-X. Zhou, H.-B. Han, S.-S. Zhou, W.-F. Feng, J. Nie, H. Li, X.-J. Huang, M. Armand, Z.-B. Zhou, Ionic liquids based on (fluorosulfonyl)(pentafluoroethanesulfonyl)imide with various oniums, Electrochimica Acta. 55 (2010) 7145–7151. https://doi.org/10.1016/j.electacta.2010.06.085.

[32] H. Matsumoto, H. Sakaebe, K. Tatsumi, Li/LiCoO2 Cell Performance Using Ionic Liquids Composed of N,N-Diethyl-N-methyl-N-(2-methoxyethyl)ammonium - Effect of Anionic Structure, in: ECS Transactions, ECS, Honolulu, HI, 2009: pp. 59–66. https://doi.org/10.1149/1.3123128.

[33] M. Ishikawa, T. Sugimoto, M. Kikuta, E. Ishiko, M. Kono, Pure ionic liquid electrolytes compatible with a graphitized carbon negative electrode in rechargeable lithium-ion batteries, Journal of Power Sources. 162 (2006) 658–662. https://doi.org/10.1016/j.jpowsour.2006.02.077.

[34] M. Egashira, S. Okada, J. Yamaki, D.A. Dri, F. Bonadies, B. Scrosati, The preparation of quaternary ammonium-based ionic liquid containing a cyano group and its properties in a lithium battery electrolyte, Journal of Power Sources. 138 (2004) 240–244. https://doi.org/10.1016/j.jpowsour.2004.06.022.

[35] P. Reale, A. Fernicola, B. Scrosati, Compatibility of the Py24TFSI–LiTFSI ionic liquid solution with Li4Ti5O12 and LiFePO4 lithium ion battery electrodes, Journal of Power Sources. 194 (2009) 182–189. https://doi.org/10.1016/j.jpowsour.2009.05.016.

[36] K. Dokko, N. Tachikawa, K. Yamauchi, M. Tsuchiya, A. Yamazaki, E. Takashima, J.-W. Park, K. Ueno, S. Seki, N. Serizawa, M. Watanabe, Solvate Ionic Liquid Electrolyte for Li–S Batteries, J. Electrochem. Soc. 160 (2013) A1304–A1310. https://doi.org/10.1149/2.111308jes.

[37] J. Zheng, M. Gu, H. Chen, P. Meduri, M.H. Engelhard, J.-G. Zhang, J. Liu, J. Xiao, Ionic liquid-enhanced solid state electrolyte interface (SEI) for lithium–sulfur batteries, J. Mater. Chem. A. 1 (2013) 8464. https://doi.org/10.1039/c3ta11553d.

[38] T. Kuboki, T. Okuyama, T. Ohsaki, N. Takami, Lithium-air batteries using hydrophobic room temperature ionic liquid electrolyte, Journal of Power Sources. 146 (2005) 766–769. https://doi.org/10.1016/j.jpowsour.2005.03.082.

[39] F. Mizuno, S. Nakanishi, Y. Kotani, S. Yokoishi, H. Iba, Rechargeable Li-Air Batteries with Carbonate-Based Liquid Electrolytes, Electrochemistry. 78 (2010) 403–405. https://doi.org/10.5796/electrochemistry.78.403.

[40] J.D. Holbrey, K.R. Seddon, Ionic Liquids, Clean Products and Processes 1. (1999) 223–236.

[41] J.A. Boon, S.W. Lander, J.A. Levisky, J.L. Pflug, L.M. Skrznecki-Cooke, J.S. Wilkes, Catalysis and reactivity of electrophilic reactions in room temperature chloroaluminate molten salts, Proceedings of the Joint International Symposium on Molten Salts. (1987) 979–990.

[42] A. Somers, P. Howlett, D. MacFarlane, M. Forsyth, A Review of Ionic Liquid Lubricants, Lubricants. 1 (2013) 3–21. https://doi.org/10.3390/lubricants1010003.

[43] J. Qu, J.J. Truhan, S. Dai, H. Luo, P.J. Blau, Ionic liquids with ammonium cations as lubricants or additives, Tribol Lett. 22 (2006) 207–214. https://doi.org/10.1007/s11249-006-9081-0.

[44] Q. Lu, H. Wang, C. Ye, W. Liu, Q. Xue, Room temperature ionic liquid 1-ethyl-3-hexylimidazolium-bis(trifluoromethylsulfonyl)-imide as lubricant for steel–steel contact, Tribology International. 37 (2004) 547–552. https://doi.org/10.1016/j.triboint.2003.12.003.

[45] I. Minami, M. Kita, T. Kubo, H. Nanao, S. Mori, The Tribological Properties of Ionic Liquids Composed of Trifluorotris(pentafluoroethyl) Phosphate as a Hydrophobic Anion, Tribol Lett. 30 (2008) 215–223. https://doi.org/10.1007/s11249-008-9329-y.

[46] A.P. de los Ríos, A. Irabien, F. Hollmann, F.J.H. Fernández, Ionic Liquids: Green Solvents for Chemical Processing, Journal of Chemistry. 2013 (2013) 1–2. https://doi.org/10.1155/2013/402172.

[47] A.E. Jiménez, M.D. Bermúdez, P. Iglesias, F.J. Carrión, G. Martínez-Nicolás, 1-N-alkyl -3-methylimidazolium ionic liquids as neat lubricants and lubricant additives in steel–aluminium contacts, Wear. 260 (2006) 766–782. https://doi.org/10.1016/j.wear.2005.04.016.

[48] K.S. Ngai, S. Ramesh, K. Ramesh, J.C. Juan, A review of polymer electrolytes: fundamental, approaches and applications, Ionics. 22 (2016) 1259–1279. https://doi.org/10.1007/s11581-016-1756-4.

[49] J. Gurusiddappa, W. Madhuri, R.P. Suvarna, K.P. Dasan, Conductivity and Dielectric Behavior of Polyethylene Oxide-Lithium Perchlorate Solid Polymer Electrolyte Films, Indian Journal of Advances in Chemical Science. (2016) 6.

[50] J. Siva Kumar, A.R. Subrahmanyam, M. Jaipal Reddy, U.V. Subba Rao, Preparation and study of properties of polymer electrolyte system (PEO+NaClO3), Materials Letters. 60 (2006) 3346–3349. https://doi.org/10.1016/j.matlet.2006.03.015.

[51] N. Shukla, A.K. Thakur, A. Shukla, D.T. Marx, Ion Conduction Mechanism in Solid Polymer Electrolyte: An Applicability of Almond-West Formalism, Int. J. Electrochem. Sci. 9 (2014) 16.

[52] J.Y. Song, Y.Y. Wang, C.C. Wan, Review of gel-type polymer electrolytes for lithium-ion batteries, Journal of Power Sources. 77 (1999) 183–197. https://doi.org/10.1016/S0378-7753(98)00193-1.

[53] S.H. Kim, K. Hong, W. Xie, K.H. Lee, S. Zhang, T.P. Lodge, C.D. Frisbie, Electrolyte-Gated Transistors for Organic and Printed Electronics, Adv. Mater. 25 (2013) 1822–1846. https://doi.org/10.1002/adma.201202790.

[54] M. Watanabe, K. Nagaoka, M. Kanba, I. Shinohara, Ionic Conductivity of Polymeric Solid Electrolytes Based on Poly(propylene oxide) or Poly(tetramethylene oxide), Polym J. 14 (1982) 877–886. https://doi.org/10.1295/polymj.14.877.

[55] S. Das, A. Ghosh, Ionic conductivity and dielectric permittivity of PEO-$LiClO_4$ solid polymer electrolyte plasticized with propylene carbonate, AIP Advances. 5 (2015) 027125. https://doi.org/10.1063/1.4913320.

[56] L. Othman, K.B. Md Isa, Z. Osman, R. Yahya, Ionic Transport Studies of Gel Polymer Electrolytes Containing Sodium Salt, Materials Today: Proceedings. 4 (2017) 5122–5129. https://doi.org/10.1016/j.matpr.2017.05.017.

[57] M. Sangeetha, A. Mallikarjun, M. Jaipal Reddy, J. Siva Kumar, SEM, XRD and electrical conductivity studies of PVDF-HFP-LiBF4 –EC plasticized gel polymer electrolyte, in: Andhra Pradesh, India, 2017: p. 020064. https://doi.org/10.1063/1.4990217.

[58] J.S. Chiou, D.R. Paul, Gas permeation in a dry Nafion membrane, Ind. Eng. Chem. Res. 27 (1988) 2161–2164. https://doi.org/10.1021/ie00083a034.

[59] B. Smitha, S. Sridhar, A.A. Khan, Solid polymer electrolyte membranes for fuel cell applications—a review, Journal of Membrane Science. 259 (2005) 10–26. https://doi.org/10.1016/j.memsci.2005.01.035.

[60] J. Adebahr, A.S. Best, N. Byrne, P. Jacobsson, D.R. MacFarlane, M. Forsyth, Ion transport in polymer electrolytes containing nanoparticulate TiO2: The influence of polymer morphology, Phys. Chem. Chem. Phys. 5 (2003) 720–725. https://doi.org/10.1039/b208454f.

[61] F. Capuano, Composite Polymer Electrolytes, J. Electrochem. Soc. 138 (1991) 1918. https://doi.org/10.1149/1.2085900.

[62] W. Wang, P. Alexandridis, Composite Polymer Electrolytes: Nanoparticles Affect Structure and Properties, Polymers. 8 (2016) 387. https://doi.org/10.3390/polym8110387.

[63] C.M. Branco, S. Sharma, M.M. de Camargo Forte, R. Steinberger-Wilckens, New approaches towards novel composite and multilayer membranes for intermediate temperature-polymer electrolyte fuel cells and direct methanol fuel cells, Journal of Power Sources. 316 (2016) 139–159. https://doi.org/10.1016/j.jpowsour.2016.03.052.

[64] G. Rydzek, Q. Ji, M. Li, P. Schaaf, J.P. Hill, F. Boulmedais, K. Ariga, Electrochemical nanoarchitectonics and layer-by-layer assembly: From basics to future, Nano Today. 10 (2015) 138–167. https://doi.org/10.1016/j.nantod.2015.02.008.

[65] J.-H. Choi, W. Xie, Y. Gu, C.D. Frisbie, T.P. Lodge, Single Ion Conducting, Polymerized Ionic Liquid Triblock Copolymer Films: High Capacitance Electrolyte Gates for n-type Transistors, ACS Applied Materials & Interfaces. 7 (2015) 7294–7302. https://doi.org/10.1021/acsami.5b00495.

[66] X. Yang, F. Zhang, L. Zhang, T. Zhang, Y. Huang, Y. Chen, A High-Performance Graphene Oxide-Doped Ion Gel as Gel Polymer Electrolyte for All-Solid-State Supercapacitor Applications, Adv. Funct. Mater. 23 (2013) 3353–3360. https://doi.org/10.1002/adfm.201203556.

[67] K. Inomata, D. Nakanishi, A. Banno, E. Nakanishi, Y. Abe, R. Kurihara, K. Fujimoto, T. Nose, Association and physical gelation of ABA triblock copolymer in selective solvent, Polymer. 44 (2003) 5303–5310. https://doi.org/10.1016/S0032-3861(03)00534-2.

[68] G. Wanka, H. Hoffmann, W. Ulbricht, Phase Diagrams and Aggregation Behavior of Poly(oxyethylene)-Poly(oxypropylene)-Poly(oxyethylene) Triblock Copolymers in Aqueous Solutions, Macromolecules. 27 (1994) 4145–4159. https://doi.org/10.1021/ma00093a016.

[69] J.M. Yu, S. Blacher, F. Brouers, L'Homme, R. Jérôme, Triblock Copolymer Based Thermoreversible Gels. 4. Effect of the Midblock and Characterization of the Sol−Gel Transition, Macromolecules. 30 (1997) 4619–4625. https://doi.org/10.1021/ma970142m.

[70] N.P. Balsara, M. Tirrell, T.P. Lodge, Micelle formation of BAB triblock copolymers in solvents that preferentially dissolve the A block, Macromolecules. 24 (1991) 1975–1986. https://doi.org/10.1021/ma00008a040.

[71] Y. He, P.G. Boswell, P. Bühlmann, T.P. Lodge, Ion Gels by Self-Assembly of a Triblock Copolymer in an Ionic Liquid †, J. Phys. Chem. B. 111 (2007) 4645–4652. https://doi.org/10.1021/jp064574n.

[72] J. Lee, M.J. Panzer, Y. He, T.P. Lodge, C.D. Frisbie, Ion Gel Gated Polymer Thin-Film Transistors, J. Am. Chem. Soc. 129 (2007) 4532–4533. https://doi.org/10.1021/ja070875e.

[73] J.H. Cho, J. Lee, Y. Xia, B. Kim, Y. He, M.J. Renn, T.P. Lodge, C. Daniel Frisbie, Printable ion-gel gate dielectrics for low-voltage polymer thin-film transistors on plastic, Nature Mater. 7 (2008) 900–906. https://doi.org/10.1038/nmat2291.

[74] Y. Gu, S. Zhang, L. Martinetti, K.H. Lee, L.D. McIntosh, C.D. Frisbie, T.P. Lodge, High Toughness, High Conductivity Ion Gels by Sequential Triblock Copolymer Self-Assembly and Chemical Cross-Linking, Journal of the American Chemical Society. 135 (2013) 9652–9655. https://doi.org/10.1021/ja4051394.

[75] J.-H. Choi, Y. Gu, K. Hong, W. Xie, C.D. Frisbie, T.P. Lodge, High Capacitance, Photo-Patternable Ion Gel Gate Insulators Compatible with Vapor Deposition of Metal Gate Electrodes, ACS Applied Materials & Interfaces. 6 (2014) 19275–19281. https://doi.org/10.1021/am505298q.

[76] G. Martínez-Ponce, C. Solano, Photocrosslinking using linear polyols in xanthene dye-doped polyvinyl alcohol plates, Optics Express. 14 (2006) 3776. https://doi.org/10.1364/OE.14.003776.

[77] Md.A.B.H. Susan, T. Kaneko, A. Noda, M. Watanabe, Ion Gels Prepared by in Situ Radical Polymerization of Vinyl Monomers in an Ionic Liquid and Their Characterization as Polymer Electrolytes, Journal of the American Chemical Society. 127 (2005) 4976–4983. https://doi.org/10.1021/ja045155b.

[78] B. Tang, S.P. White, C.D. Frisbie, T.P. Lodge, Synergistic Increase in Ionic Conductivity and Modulus of Triblock Copolymer Ion Gels, Macromolecules. 48 (2015) 4942–4950. https://doi.org/10.1021/acs.macromol.5b00882.

[79] Y. Gu, T.P. Lodge, Synthesis and Gas Separation Performance of Triblock Copolymer Ion Gels with a Polymerized Ionic Liquid Mid-Block, Macromolecules. 44 (2011) 1732–1736. https://doi.org/10.1021/ma2001838.

[80] W. Wu, Inorganic nanomaterials for printed electronics: a review, Nanoscale. 9 (2017) 7342–7372. https://doi.org/10.1039/C7NR01604B.

[81] R. Parashkov, E. Becker, T. Riedl, H.-H. Johannes, W. Kowalsky, Large Area Electronics Using Printing Methods, Proc. IEEE. 93 (2005) 1321–1329. https://doi.org/10.1109/JPROC.2005.850304.

[82] C.C. Hu, Modern Semiconductor Devices for Integrated Circuits, Pearson, 2010.

[83] F. von Seggern, I. Keskin, E. Koos, R. Kruk, H. Hahn, S. Dasgupta, Temperature-Dependent Performance of Printed Field-Effect Transistors with Solid Polymer Electrolyte Gating, ACS Appl. Mater. Interfaces. 8 (2016) 31757–31763. https://doi.org/10.1021/acsami.6b10939.

[84] H. Helmholtz, Ueber einige Gesetze der Vertheilung elektrischer Ströme in körperlichen Leitern mit Anwendung auf die thierisch-elektrischen Versuche, Ann. Phys. Chem. 165 (1853) 211–233. https://doi.org/10.1002/andp.18531650603.

[85] O. Stern, ZUR THEORIE DER ELEKTROLYTISCHEN DOPPELSCHICHT, Elektrochemie und angewandte physikalische Chemie. 30 (1924) 508–516.

[86] D.C. Grahame, The Electrical Double Layer and the Theory of Electrocapillarity., Chem. Rev. 41 (1947) 441–501. https://doi.org/10.1021/cr60130a002.

[87] E. Barsoukov, J.R. Macdonald, Impedance Spectroscopy: Theory, Experiment, and Applications, Wiley-VCH, 2005.

[88] H. Nyquist, Regeneration Theory, Bell System Technical Journal. 11 (1932) 126–147. https://doi.org/10.1002/j.1538-7305.1932.tb02344.x.

[89] J.E.B. Randles, Kinetics of rapid electrode reactions, Discuss. Faraday Soc. 1 (1947) 11. https://doi.org/10.1039/df9470100011.

[90] R.A. Dorledo de Faria, L.G. Dias Heneine, T. Matencio, Y. Messaddeq, Faradaic and non-faradaic electrochemical impedance spectroscopy as transduction techniques for sensing applications, IJBSBE. 5 (2019). https://doi.org/10.15406/ijbsbe.2019.05.00148.

[91] S.-M. Park, J.-S. Yoo, Peer reviewed: electrochemical impedance spectroscopy for better electrochemical measurements, Analytical Chemistry. 75 (2003) 455–461. https://doi.org/10.1021/ac0313973.

[92] J. Kang, J. Wen, S.H. Jayaram, A. Yu, X. Wang, Development of an equivalent circuit model for electrochemical double layer capacitors (EDLCs) with distinct electrolytes, Electrochimica Acta. 115 (2014) 587–598. https://doi.org/10.1016/j.electacta.2013.11.002.

[93] B.-A. Mei, O. Munteshari, J. Lau, B. Dunn, L. Pilon, Physical Interpretations of Nyquist Plots for EDLC Electrodes and Devices, J. Phys. Chem. C. 122 (2018) 194–206. https://doi.org/10.1021/acs.jpcc.7b10582.

[94] O. Larsson, E. Said, M. Berggren, X. Crispin, Insulator Polarization Mechanisms in Polyelectrolyte-Gated Organic Field-Effect Transistors, Advanced Functional Materials. 19 (2009) 3334–3341. https://doi.org/10.1002/adfm.200900588.

[95] B.M. Greenhoe, M.K. Hassan, J.S. Wiggins, K.A. Mauritz, Universal power law behavior of the AC conductivity versus frequency of agglomerate morphologies in conductive carbon nanotube-reinforced epoxy networks, J. Polym. Sci. Part B: Polym. Phys. 54 (2016) 1918–1923. https://doi.org/10.1002/polb.24121.

[96] R. Baskaran, S. Selvasekarapandian, N. Kuwata, J. Kawamura, T. Hattori, Conductivity and thermal studies of blend polymer electrolytes based on PVAc–PMMA, Solid State Ionics. 177 (2006) 2679–2682. https://doi.org/10.1016/j.ssi.2006.04.013.

[97] J. L. Ndeugueu, M. Aniya, On the Power Law Behavior of the A.C. Conductivity in Li Ion Conducting Perovskites, J. Phys. Soc. Jpn. 79 (2010) 72–75. https://doi.org/10.1143/JPSJS.79SA.72.

[98] S. Choudhary, R.J. Sengwa, Dielectric relaxation spectroscopy and ion conduction in poly(ethylene oxide)-blend salts-montmorillonite nanocomposite electrolytes, APPL PHYS. 49 (2011) 10.

[99] S. Dasgupta, G. Stoesser, N. Schweikert, R. Hahn, S. Dehm, R. Kruk, H. Hahn, Printed and Electrochemically Gated, High-Mobility, Inorganic Oxide Nanoparticle FETs and Their Suitability for High-Frequency Applications, Advanced Functional Materials. 22 (2012) 4909–4919. https://doi.org/10.1002/adfm.201200951.

[100] D. Braun, H. Cherdron, M. Rehahn, G. Ritter, B. Voit, Polymer Synthesis: Theory and Practice, 5th ed., Springer, n.d.

[101] R. Horstman, K. Peters, R. Meltzer, M. Vieth, B. Fanconi, Fourier Transform Infrared Spectroscopy of Polymers—Theory and Application, J. Test. Eval. 12 (1984) 33. https://doi.org/10.1520/JTE11418J.

[102] H.W. Siesler, Near-infrared spectroscopy of polymers, Makromolekulare Chemie. Macromolecular Symposia. 52 (1991) 113–129. https://doi.org/10.1002/masy.19910520111.

[103] B. Schneider, O.-D. Hennemann, W. Possart, The Adhesion of Maleic Anhydride on Native Aluminum Oxide: An Approach by Infrared Spectroscopy and Quantum Mechanical Modeling, The Journal of Adhesion. 78 (2002) 779–797. https://doi.org/10.1080/00218460213837.

[104] R.M. Silverstein, G.C. Bassler, T.C. Morrill, Spectrometric Identification of Organic Compounds, John Wiley and Sons, New York, NY, 1981.

[105] J.-H. Choi, Y. Gu, K. Hong, W. Xie, C.D. Frisbie, T.P. Lodge, High Capacitance, Photo-Patternable Ion Gel Gate Insulators Compatible with Vapor Deposition of Metal Gate Electrodes, ACS Applied Materials & Interfaces. 6 (2014) 19275–19281. https://doi.org/10.1021/am505298q.

[106] D. Braun, H. Cherdron, M. Rehahn, G. Ritter, B. Voit, Polymer Synthesis: Theory and Practice, 5th ed., Springer, n.d.

[107] M. Ratzsch, Alternating Maleic Anhydride Copolymers, Prog. Polym. Sci. (1988) 277–337. https://doi.org/10.1016/0079-6700(88)90001-9.

[108] C.Q. Yang, X. Wang, Formation of five-membered cyclic anhydride intermediates by polycarboxylic acids: Thermal analysis and Fourier transform infrared spectroscopy, Journal of Applied Polymer Science. 70 (1998) 2711–2718. https://doi.org/10.1002/(SICI)1097-4628(19981226)70:13<2711::AID-APP16>3.0.CO;2-Z.

[109] C.Q. Yang, Infrared spectroscopy studies of the cyclic anhydride as the intermediate for the ester crosslinking of cotton cellulose by polycarboxylic acids. I. Identification of the cyclic anhydride intermediate, Journal of Polymer Science Part A: Polymer Chemistry. 31 (1993) 1187–1193. https://doi.org/10.1002/pola.1993.080310514.

[110] C.Q. Yang, D. Chen, J. Guan, Q. He, Cross-Linking Cotton Cellulose by the Combination of Maleic Acid and Sodium Hypophosphite. 1. Fabric Wrinkle Resistance, Ind. Eng. Chem. Res. 49 (2010) 8325–8332. https://doi.org/10.1021/ie1007294.

[111] E. Peng, E.S.G. Choo, C.S.H. Tan, X. Tang, Y. Sheng, J. Xue, Multifunctional PEGylated nanoclusters for biomedical applications, Nanoscale. 5 (2013) 5994–6005. https://doi.org/10.1039/c3nr00774j.

[112] C. Rohatgi, N. Dutta, N. Choudhury, Separator Membrane from Crosslinked Poly(Vinyl Alcohol) and Poly(Methyl Vinyl Ether-alt-Maleic Anhydride), Nanomaterials. 5 (2015) 398–414. https://doi.org/10.3390/nano5020398.

[113] W.-Y. Chiang, C.-M. Hu, Studies of reactions with polymers. I. The reaction of maleic anhydride with PVA and the properties of the resultant, Journal of Applied Polymer Science. 30 (1985) 3895–3910. https://doi.org/10.1002/app.1985.070300928.

[114] D. Dibbern-Brunelli, T.D.Z. Atvars, I. Joekes, V.C. Barbosa, Mapping phases of poly(vinyl alcohol) and poly(vinyl acetate) blends by FTIR microspectroscopy and optical fluorescence microscopy, Journal of Applied Polymer Science. 69 (1998) 645–655. https://doi.org/10.1002/(SICI)1097-4628(19980725)69:4<645::AID-APP3>3.0.CO;2-J.

[115] N.E. Heimer, R.E. Del Sesto, Z. Meng, J.S. Wilkes, W.R. Carper, Vibrational spectra of imidazolium tetrafluoroborate ionic liquids, Journal of Molecular Liquids. 124 (2006) 84–95. https://doi.org/10.1016/j.molliq.2005.08.004.

[116] M. Udayakumar, M. Kollár, F. Kristály, M. Leskó, T. Szabó, K. Marossy, I. Tasnádi, Z. Németh, Temperature and Time Dependence of the Solvent-Induced Crystallization of Poly(l-lactide), Polymers. 12 (2020) 1065. https://doi.org/10.3390/polym12051065.

[117] P. Müller-Buschbaum, J.S. Gutmann, M. Wolkenhauer, J. Kraus, M. Stamm, D. Smilgies, W. Petry, Solvent-Induced Surface Morphology of Thin Polymer Films, Macromolecules. 34 (2001) 1369–1375. https://doi.org/10.1021/ma0009193.

[118] S. Choudhary, R.J. Sengwa, Dielectric relaxation spectroscopy and ion conduction in poly(ethylene oxide)-blend salts-montmorillonite nanocomposite electrolytes, APPL PHYS. 49 (2011) 10.

[119] N. Shukla, A.K. Thakur, A. Shukla, D.T. Marx, Ion Conduction Mechanism in Solid Polymer Electrolyte: An Applicability of Almond-West Formalism, Int. J. Electrochem. Sci. 9 (2014) 16.

[120] Z. Osman, M.I. Mohd Ghazali, L. Othman, K.B. Md Isa, AC ionic conductivity and DC polarization method of lithium ion transport in PMMA–LiBF4 gel polymer electrolytes, Results in Physics. 2 (2012) 1–4. https://doi.org/10.1016/j.rinp.2011.12.001.

[121] K.H. Lee, S. Zhang, T.P. Lodge, C.D. Frisbie, Electrical Impedance of Spin-Coatable Ion Gel Films, The Journal of Physical Chemistry B. 115 (2011) 3315–3321. https://doi.org/10.1021/jp110166u.

[122] K. Darowicki, K. Andrearczyk, P. Slepski, A. Sierczynska, G. Lota, K. Fic, K. Lota, Determination of Pseudocapacitance Changes of Nickel Oxide NiO Electrode with the Use of Dynamic Electrochemical Impedance Spectroscopy, Int. J. Electrochem. Sci. 9 (2014) 13.

[123] M. Singh, K. Manoli, A. Tiwari, T. Ligonzo, C. Di Franco, N. Cioffi, G. Palazzo, G. Scamarcio, L. Torsi, The double layer capacitance of ionic liquids for electrolyte gating of ZnO thin film transistors and effect of gate electrodes, Journal of Materials Chemistry C. 5 (2017) 3509–3518. https://doi.org/10.1039/C7TC00800G.

[124] G. Cadilha Marques, D. Weller, A.T. Erozan, X. Feng, M. Tahoori, J. Aghassi-Hagmann, Progress Report on "From Printed Electrolyte-Gated Metal-Oxide Devices to Circuits," Adv. Mater. 31 (2019) 1806483. https://doi.org/10.1002/adma.201806483.

[125] G. Cadilha Marques, F. von Seggern, S. Dehm, B. Breitung, H. Hahn, S. Dasgupta, M.B. Tahoori, J. Aghassi-Hagmann, Influence of Humidity on the Performance of Composite

Polymer Electrolyte-Gated Field-Effect Transistors and Circuits, IEEE Trans. Electron Devices. 66 (2019) 2202–2207. https://doi.org/10.1109/TED.2019.2903456.

[126] G. Hirankumar, N. Mehta, Effect of incorporation of different plasticizers on structural and ion transport properties of PVA-LiClO4 based electrolytes, Heliyon. 4 (2018) e00992. https://doi.org/10.1016/j.heliyon.2018.e00992.

[127] B. Tang, S.P. White, C.D. Frisbie, T.P. Lodge, Synergistic Increase in Ionic Conductivity and Modulus of Triblock Copolymer Ion Gels, Macromolecules. 48 (2015) 4942–4950. https://doi.org/10.1021/acs.macromol.5b00882.

[128] G.C. Marques, S.K. Garlapati, D. Chatterjee, S. Dehm, S. Dasgupta, J. Aghassi, M.B. Tahoori, Electrolyte-Gated FETs Based on Oxide Semiconductors: Fabrication and Modeling, IEEE Transactions on Electron Devices. 64 (2017) 279–285. https://doi.org/10.1109/TED.2016.2621777.

[129] F. von Seggern, I. Keskin, E. Koos, R. Kruk, H. Hahn, S. Dasgupta, Temperature-Dependent Performance of Printed Field-Effect Transistors with Solid Polymer Electrolyte Gating, ACS Applied Materials & Interfaces. 8 (2016) 31757–31763. https://doi.org/10.1021/acsami.6b10939.

[130] S. Dasgupta, R. Kruk, N. Mechau, H. Hahn, Inkjet Printed, High Mobility Inorganic-Oxide Field Effect Transistors Processed at Room Temperature, ACS Nano. 5 (2011) 9628–9638. https://doi.org/10.1021/nn202992v.

[131] T.T. Baby, S.K. Garlapati, S. Dehm, M. Häming, R. Kruk, H. Hahn, S. Dasgupta, A General Route toward Complete Room Temperature Processing of Printed and High Performance Oxide Electronics, ACS Nano. 9 (2015) 3075–3083. https://doi.org/10.1021/nn507326z.

[132] J.H. Cho, J. Lee, Y. Xia, B. Kim, Y. He, M.J. Renn, T.P. Lodge, C. Daniel Frisbie, Printable ion-gel gate dielectrics for low-voltage polymer thin-film transistors on plastic, Nature Mater. 7 (2008) 900–906. https://doi.org/10.1038/nmat2291.

[133] K.H. Lee, M.S. Kang, S. Zhang, Y. Gu, T.P. Lodge, C.D. Frisbie, "Cut and Stick" Rubbery Ion Gels as High Capacitance Gate Dielectrics, Adv. Mater. 24 (2012) 4457–4462. https://doi.org/10.1002/adma.201200950.

[134] J. Jeong, G.C. Marques, X. Feng, D. Boll, S.A. Singaraju, J. Aghassi-Hagmann, H. Hahn, B. Breitung, Ink-Jet Printable, Self-Assembled, and Chemically Crosslinked Ion-Gel as Electrolyte for Thin Film, Printable Transistors, Adv. Mater. Interfaces. 6 (2019) 1901074. https://doi.org/10.1002/admi.201901074.

[135] P.A. McCarron, A.D. Woolfson, R.F. Donnelly, G.P. Andrews, A. Zawislak, J.H. Price, Influence of plasticizer type and storage conditions on properties of poly(methyl vinyl ether-co-maleic anhydride) bioadhesive films, J. Appl. Polym. Sci. 91 (2004) 1576–1589. https://doi.org/10.1002/app.13228.

[136] K. Yoncheva, E. Lizarraga, J.M. Irache, Pegylated nanoparticles based on poly(methyl vinyl ether-co-maleic anhydride): preparation and evaluation of their bioadhesive properties, European Journal of Pharmaceutical Sciences. 24 (2005) 411–419. https://doi.org/10.1016/j.ejps.2004.12.002.

[137] P. Arbós, M.A. Arangoa, M.A. Campanero, J.M. Irache, Quantification of the bioadhesive properties of protein-coated PVM/MA nanoparticles, International Journal of Pharmaceutics. 242 (2002) 129–136. https://doi.org/10.1016/S0378-5173(02)00182-5.

[138] D.S. Jones, M.S. Lawlor, A.D. Woolfson, Rheological and mucoadhesive characterization of polymeric systems composed of poly(methylvinylether-co-maleic anhydride) and poly(vinylpyrrolidone), designed as platforms for topical drug delivery, Journal of Pharmaceutical Sciences. 92 (2003) 995–1007. https://doi.org/10.1002/jps.10357.

[139] T. Cerchiara, B. Luppi, G. Chidichimo, F. Bigucci, V. Zecchi, Chitosan and poly(methyl vinyl ether-co-maleic anhydride) microparticles as nasal sustained delivery systems, European Journal of Pharmaceutics and Biopharmaceutics. 61 (2005) 195–200. https://doi.org/10.1016/j.ejpb.2005.05.005.

[140] P. Arbós, Influence of the surface characteristics of PVM/MA nanoparticles on their bioadhesive properties, Journal of Controlled Release. 89 (2003) 19–30. https://doi.org/10.1016/S0168-3659(03)00066-X.

[141] C.E. Schildknecht, A.O. Zoss, C. McKinley, Vinyl Alkyl Ethers, Ind. Eng. Chem. 39 (1947) 180–186. https://doi.org/10.1021/ie50446a021.

[142] K.-J. Baeg, Polymer Dielectrics and Orthogonal Solvent Effects for High-Performance Inkjet-Printed Top-Gated P-Channel Polymer Field-Effect Transistors, ETRI J. 33 (2011) 887–896. https://doi.org/10.4218/etrij.11.0111.0321.

[143] L. Zhang, C. Di, Y. Zhao, Y. Guo, X. Sun, Y. Wen, W. Zhou, X. Zhan, G. Yu, Y. Liu, Top-Gate Organic Thin-Film Transistors Constructed by a General Lamination Approach, Adv. Mater. 22 (2010) 3537–3541. https://doi.org/10.1002/adma.201000123.

[144] S. Perrier, *50th Anniversary Perspective*: RAFT Polymerization—A User Guide, Macromolecules. 50 (2017) 7433–7447. https://doi.org/10.1021/acs.macromol.7b00767.

E. Curriculum Vitae (CV)

EDUCATION

Oct 2017 ~ Nov 2020	**Research Institute**: Institute of Nanotechnology (INT), Karlsruhe Institute of Technology (KIT Campus North), Helmholtz Association of German Research Centres **University**: Technische Universität Darmstadt, Department of Material Science Supervisor: Prof. Dr.-Ing. Horst Hahn and Dr. Ben Breitung **Thesis**: The Study of Chemically Cross-linked Ion gels for Electronic Devices
Mar 2015 ~ Feb 2017	Gwangju Institute of Science and Technology (GIST), School of Environmental Science and Engineering (GPA: 4.07 / 4.5) Supervisor: Prof. Dr. Jaeyoung Lee **Thesis**: The Role of Porous and Reactive N-doped Carbon Nanofiber on Electrochemical Oxidation of Hydrazine in Alkaline Media (2017)
Mar 2009 ~ Feb 2015	Soongsil University, Chemical Engineering (GPA: 3.93 / 4.5)
Mar 2006 ~ Feb 2009	Baek Shin High School

EXPERIENCE

Mar 2017 ~ May 2017	Assistant researcher, Electrochemical Reaction & Technology Laboratory, Gwangju Institute of Science and Technology (GIST)
Jan 2014 ~ Feb 2014	Internship program, Electronic Materials Dept. BASF Korea Market research and sales engineering
Jul 2013 ~ Aug 2013	Internship program & 13th Environmental Science Olympiad, GIST, Excellence award, Research Topic: Ammonia Electrolysis in Alkaline Zero-gap Cell
Dec 2012 ~ Feb 2013	Internship program, Public Affairs Dept. U.S. Embassy in Seoul Data collection, Research, and reporting

OTHER EXPERIENCES

Sept 2012~ Feb 2013	Voluntary service, Plan Korea Provided various translation services
Jul 2010 ~ Apr 2012	Military service, Ammunition Support Command, Republic of Korea Army

SCHOLARSHIP & AWARDS

Jun. 2017 ~ Sep. 2020	DAAD Research Grants - Doctoral Program Scholarship (2017/2018)
Aug. 2013	Scholarship for the best student in chemical engineering, Soongsil Univ.
Jul. 2013	Excellence award, Environment and Science Olympiad, GIST.

PUBLICATIONS (* = published during Ph.D. program)

1. **Jaehoon Jeong**, Gabriel Cadilha Marques, Xiaowei Feng, Dominic Boll, Surya Abhishek Singaraju, Jasmin Aghassi-Hagmann, Horst Hahn, Ben Breitung, "Ink-Jet Printable, Self-Assembled, and Chemically Crosslinked Ion-Gel as Electrolyte for Thin Film, Printable Transistors", Advanced Materials Interfaces, 2019, 6, 1901074. [Frontispiece] *
2. **Jaehoon Jeong**, Surya Abhishek Singaraju, Jasmin Aghassi-Hagmann, Horst Hahn, Ben Breitung, "Adhesive Ion-gel for Gate Insulator of Electrolyte-gated Transistors", ChemElectroChem 2020, 7, 2735-2739. [Front Cover] *
3. Junbo Wang, David Stenzel, Raheleh Azmi, Saleem Najib, Kai Wang, **Jaehoon Jeong**, Abhishek Sarkar, Qingsong Wang, Parvathy Anitha Sukkurji, Thomas Bergfeldt, Miriam Botros, Julia Maibach, Horst Hahn, Torsten Brezesinski, Ben Breitung, "Spinel to Rock-Salt Transformation in High Entropy Oxides with Li Incorporation", Electrochem 2020, 1(1), 60-74. *
4. **Jaehoon Jeong**, Myounghoon Choun, Jaeyoung Lee, "Tree-Bark-Shaped N-doped Porous Carbon Anode for Hydrazine Fuel Cells", Angewandte Chemie International Edition (2017), 56, 13513-13516.
5. Thi Huong Vu, Dongyoon Shin, **Jaehoon Jeong**, Jaeyoung Lee, "Porous and Conductive Fibrous Carbon for Enhanced Electrocatalytic Oxygen Reduction Reaction in Alkaline Media", the Journal of Physical Chemistry C (2016), 120, 22342-22348.
6. Xianghua An, Dongyoon Shin, **Jaehoon Jeong**, Jaeyoung Lee, "Metal-Derived Mesoporous Structure of a Carbon Nanofiber Electrocatalyst for Improved Oxygen Evolution Reaction in Alkaline Water Electrolysis," ChemElectroChem (2016), 3, 1720-1724.
7. Jiyong Joo, Myounghoon Choun, **Jaehoon Jeong**, Jaeyoung Lee, "The Influence of Solution pH on Pt Anode Catalyst in Direct Formic Acid Fuel Cells," ACS Catalysis 5 (2015) 6848-6851.

PATENT

1. **Jaehoon Jeong**, Ben Breitung, Horst Hahn, Gabriel Cadilha Marques, "Electrolyte for pri nting electronics, method for preparing it and its use", (Submitted)